RELATIONSHIP BETWEEN MITOCHONDRIAL MEMBRANE POTENTIAL COLLAPSE AND ELECTRICAL FAILURE IN A GLOBALLY ISCHEMIC HEART

by

Paul W. Venable

A dissertation submitted to the faculty of
The University of Utah
in partial fulfillment of the requirements for the degree of

Doctor of Philosophy

Department of Bioengineering

The University of Utah

May 2015

The University of Utah Graduate School

STATEMENT OF DISSERTATION APPROVAL

The dissertation of **Paul W. Venable**

has been approved by the following supervisory committee members:

Alexey Zaitsev	, Chair	**11/6/2014** Date Approved
Robert MacLeod	, Member	**11/6/2014** Date Approved
Alan Dorval	, Member	**11/7/2014** Date Approved
Mark Warren	, Member	**11/6/2014** Date Approved
Kenneth Spitzer	, Member	**11/6/2014** Date Approved

and by **Patrick Tresco**, Chair/Dean of

the Department/College/School of **Bioengineering**

and by David B. Kieda, Dean of The Graduate School.

ABSTRACT

Sudden Cardiac Arrest (SCA) remains one of the leading causes of death in the United States. During SCA, the inability of the heart to pump blood causes progressive metabolic and functional derangements in the heart itself. In the majority of SCA cases, the defining event of death is the failure of defibrillation shocks and cardio-pulmonary resuscitation (CPR) procedures to restore circulation within the first 10 minutes. Resuscitation failure is often due to either asystole (the lack of activation in the heart) or recurrent ventricular fibrillation following defibrillation. The exact physiological mechanisms determining the occurrence of these phenomena within the clinically relevant time frame remain largely unknown. One postulated mechanism linking metabolic stress and electrical abnormalities during SCA is the loss of mitochondrial inner membrane potential ($\Delta\Psi_m$) and the consequent activation of the adenosine triphosphate (ATP)-sensitive potassium channel (K_{ATP}) when cellular ATP is critically depleted.

The goal of this dissertation was to investigate the relationship between $\Delta\Psi_m$ depolarization, electrical failure, and arrhythmias in a model of SCA. The work consisted of three projects. In the first, I characterized the spatiotemporal dynamics of electrical failure in a whole-heart model of VF-induced SCA. I demonstrated that the electrical depression develops in a heterogeneous fashion across the heart and is partially dependent on K_{ATP} activation. In the second project, I developed a method to detect $\Delta\Psi_m$

depolarization during global ischemia using spectral analysis of confocally recorded $\Delta\Psi_m$-sensitive fluorescence. The method is based on the spatial periodicity of mitochondrial packaging in ventricular myocytes and the preferential accumulation of cationic fluorophores in well-polarized mitochondria and addresses the limitations of the traditional mean fluorescence approach during ischemia. Using this method, in the third project, I determined the temporal relationship between ischemic $\Delta\Psi_m$ depolarization and myocardial inexcitability. Additionally, I modulated the energy balance in ischemic hearts using rapid pacing, the inhibitor of myosin II ATPase, blebbistatin, and the inhibitor of anaerobic glycolysis, sodium iodoacetate. This study showed a strong correlation between the onset of asystole and the time of $\Delta\Psi_m$ loss under all tested conditions, and revealed a strong protective effect of Blebbistatin against asystole, $\Delta\Psi_m$ loss, and postreperfusion arrhythmias.

For my wife.

CONTENTS

ACKNOWLEDGEMENTS

The research presented in the following chapters of this dissertation would not have been possible without the dedicated help and knowledgeable advice of many people. The manufacturing of experimental equipment, design and execution of protocols, and the final analysis and presentation of data are the summation of countless hours of collaboration. First and foremost I would like to thank my advisor Dr. Alexey Zaitsev. Alexey has taught me to notice and appreciate the aesthetic of well-executed research, and helped me to grow in countless facets of my professional life. Without his mentorship, I would not have been able to been able to ask and more importantly answer the scientific question presented in this dissertation. I would also like to thank all the members of the Zaitsev lab; Mark Warren, Junco Warren, Vivek Garg, Alicja Booth, and Katie Sciuto. I cannot reflect on my time at CVRTI without thinking of the hours spent running experiments together, jointly analyzing data, and enjoying the company of my fellow lab members. I would especially like to thank Tyson Taylor, who has become an indispensable colleague and friend during our joint paths through graduate school.

The CVRTI staff played vital roles in all aspects of my research. Jayne Davis and Nancy Allen were indispensable in working with the numerous animal models required to complete this dissertation. The design and manufacturing of my experimental equipment would not have been possible without the help of Bruce Steadman, Dennis King, and Wilson Lobaina. Phil Ershler and Marshall Scott kept my computers and acquisition

systems functioning; Jerry Jenkins and Mike Heidinger made sure I always had the supplies I needed despite my often last-minute requests. Tonnya Baxter and Alicia Geesman made sure I only had to worry about my experiments and not about my next paycheck.

I would also like to thank my committee members, Dr. MacLeod, Dr. Dorval, Dr. Spitzer, and Dr. Warren, who have provided me with excellent scientific guidance throughout my PhD. I especially would like to thank Dr. Spitzer for all the extra time he spent working with me on the Zeiss microscope.

Last but far from least, I would like to thank my beautiful wife Shawna. Without her constant dedication and understanding, I would not have been able to complete this work. She is truly my foundation.

CHAPTER 1

INTRODUCTION

Mortality rates due to ventricular fibrillation (VF)-induced sudden cardiac arrest (SCA) remain unacceptably high despite improved resuscitation techniques. One major reason for poor survival is the inability to restore and maintain electrical rhythm compatible with a sufficient cardiac output. Electrical outcomes associated with SCA include severe bradycardia, asystole (complete loss of electrical activity), and recurrence of VF upon resuscitation interventions. Existing evidence suggests that a mechanism leading to all of these events may be the opening of the adenosine triphosphate (ATP)-sensitive potassium channel (K_{ATP}). The K_{ATP} channel is blocked by physiological concentrations of ATP, but it is activated when concentrations of ATP, adenosine diphosphate (ADP), and lactate are altered by metabolic stress. Significant activation of this channel can render cardiac myocytes completely inexcitable by clamping the transmembrane potential at the resting level and preventing depolarization. Regional differences in the level of K_{ATP} activation can eventually lead to localized inexcitability due to source-sink mismatch, thus enhancing wave fragmentation during VF. In isolated cells, K_{ATP} activation following the collapse of the mitochondrial inner membrane potential ($\Delta\Psi_m$) can lead to loss of cell excitability. Therefore, the current concept of electrical failure during ischemia posits that the opening of the K_{ATP} channel and its

associated inexcitability is mediated by a decrease in ATP following $\Delta\Psi_m$ collapse (1). However, the dynamics of $\Delta\Psi_m$ in whole-heart models of SCA remain largely unknown, and its cause-effect relationship with electrical failure has not been tested. Challenging the current concept, I hypothesized that in the context of VF-induced SCA, $\Delta\Psi_m$ collapse is not the primary cause of electrical failure. Rather, the onset of *both* the electrical failure and $\Delta\Psi_m$ collapse are dependent on the ability of anaerobic glycolysis to maintain intracellular ATP at the level sufficient for blocking K_{ATP}, and maintaining $\Delta\Psi_m$ through ATP hydrolysis by the mitochondrial F_0-F_1 ATPase. Thus, an increase in ATP consumption due to the high frequency of excitations associated with VF, or a decrease in ATP production due to the partial blockade of anaerobic glycolysis, would accelerate both the onset of the electrical failure and $\Delta\Psi_m$ collapse, but the latter two events are not necessarily linked. Confirmation of the role of anaerobic glycolysis in modulating $\Delta\Psi_m$ collapse and inexcitability during SCA would help direct future research and improve SCA survival outcomes. Additionally, blockade of the K_{ATP} channel should separate the two events by postponing asystole, but not delaying $\Delta\Psi_m$ depolarization. The research presented in the chapters of this dissertation includes the following projects.

1.1 Projects

In Project 1, I characterized the timing and spatial dynamics of the progressive electrical failure in a whole-heart model of VF-induced cardiac arrest using voltage-sensitive optical mapping. I hypothesized that long-duration VF in a globally ischemic heart is characterized by a progressive increase in conduction block and progressively more complex arrhythmias, culminating in areas of complete inexcitability within a

clinically relevant time frame. I tested this hypodissertation using optical mapping of a voltage-sensitive dye for reliable detection of cardiac excitations and the timing of inexcitability in an isolated canine heart. As a sub-aim, I determined the effect of K_{ATP} channel blockade on the spatiotemporal pattern of electrical failure during VF-induced cardiac arrest.

In Project 2, I developed and validated a methodology to detect $\Delta\Psi_m$ depolarization during whole-heart global ischemia using spectral analysis of confocal images of $\Delta\Psi_m$–sensitive fluorescence. I developed a method for detection of $\Delta\Psi_m$ depolarization based on spatial periodicity of mitochondrial packaging in ventricular myocytes and the preferential accumulation of cationic fluorophores in well-polarized mitochondria. This method addressed the limitations of traditional approaches of monitoring $\Delta\Psi_m$ in whole-hearts under conditions of no-flow ischemia.

In Project 3, I determined the temporal relationship between $\Delta\Psi_m$ depolarization and electrical depression in globally ischemic hearts under different conditions modulating energy balance. I hypothesized that both $\Delta\Psi_m$ depolarization and electrical failure would be modulated in a parallel fashion by affecting either the ATP production (using an inhibitor of anaerobic glycolysis) or ATP consumption (using an inhibitor of myosin ATPase or rapid stimulation) in ischemic cardiac myocytes. Additionally, I hypothesized that K_{ATP} channel blockade would delay asystole, but $\Delta\Psi_m$ depolarization time would not be modulated. I determined the time of $\Delta\Psi_m$ depolarization using the method developed in Project 2, and compared it to the time of electrical failure using local and global electrical recordings from the same heart.

1.2 Organization of the dissertation

This dissertation is organized into eight chapters. Chapter 1 provides an introduction to the research problem and the goals of each project. Chapter 2 presents an overview of basic cardiac electrophysiology and the primary research methods. The research timeline and solutions to problems encountered during the studies are outlined in Chapter 3. Studies under Project 1 are described in Chapters 4 and 5: Chapter 4 presents research on the progression of ventricular fibrillation during ischemia in a whole-heart model of sudden cardiac arrest; Chapter 5 concerns the effects of K_{ATP} channel blockade with glybenclamide on the same model. Studies under Project 2 concerning a new method to monitor mitochondrial membrane potential ($\Delta\Psi_m$) in confocally imaged whole-hearts are described in Chapter 6. Studies under Project 3 concerning the relationship between ischemic $\Delta\Psi_m$ depolarization and electrical failure under conditions modulating energy balance during ischemia are described in Chapter 7. Finally, Chapter 8 discusses the overall scientific contribution of the dissertation and outlines future research topics.

CHAPTER 2

CARDIAC ELECTROPHYSIOLOGY OVERVIEW AND RESEARCH METHODS

The heartbeat is the foundation of life. The synchronized electrical activations of the heart gives rise to contraction of cardiac cells, or cardiomyocytes, thus providing the force to eject blood from the artium followed by the ventricles. When the electrical activity of the heart is working correctly, it can efficiently and reliably supply blood to its own arteries and to the rest of the body. However, when the electrical system is disrupted and no longer initiates the electromechanical activation of the heart in a synchronous manner, the heart quickly loses the ability to provide the necessary blood flow. This loss of blood flow, also known as ischemia, causes a time-sensitive disruption to the complex system that enables activation. If normal activation is not restored in a timely manner, the heart will become asystolic, a state in which activation is no longer sustainable. The disruption of rhythm and loss of contraction resulting in ischemia is clinically known as sudden cardiac arrest (SCA).

SCA remains a leading cause of mortality in Western societies; in the United States alone, an estimated 273,000 out-of-hospital SCA events occur annually (17). For patients presenting the unsynchronized rhythm of ventricular fibrillation (VF) at the time of first response, recent data have found a dismal mean survival rate of 18% (24). This

can be attributed to a variety of factors. Once blood flow to the heart is diminished, the heart enters a rapid decline in its ability to maintain excitability.

Currently, the gold standard treatment of VF-induced SCA is defibrillation. The time delay prior to defibrillation has been shown to have a major influence on survival; a study by Valenzuela et al. found a 1.1 times increase in likelihood of death for *every minute of delayed defibrillation* (34). A defibrillation delay may also impact the rhythm after defibrillation; White et al. found that 61% of SCA victims refibrillated after initial defibrillation (40). In a more detailed study, Lo et al. reported on the rhythm present 20 seconds after a monophasic defibrillation shock to victims of out-of-hospital cardiac arrest. Of 378 subjects presenting VF during SCA, 184 (49%) refibrillated following the first shock, while 123 (33%) had no detectable rhythm (asystole) (18). Thus, recurrent fibrillation following defibrillation and asystole present a major clinical challenge for the recovery of normal synchronous rhythm during life-saving interventions in the setting of SCA.

2.1 Basic cardiac electrophysiology

The available clinical data indicate a need for further investigation of the temporal and spatial progression of inexcitability during clinically relevant durations of global ischemia. The global events of VF and asystole are directly linked to the mechanisms of excitability at the cellular level and conduction at the tissue level. Therefore, translational research to address clinical needs requires a foundation in basic cardiac electrophysiology. The fundamental property of cardiomyocytes is their ability to actively change the electrical potential across the cell membrane. The electrical potential

arises from the separation of ions by the cell membrane and energy-consuming pumps that maintain ion gradients. Electrical currents in the form of ions (potassium, sodium, calcium and chloride) passing through transmembrane channels drive the changes in membrane potential that in summation create the cardiac action potential.

The separation of intracellular and extracellular ions by the sarcolemmal membrane is the basis for membrane potential and excitability. The sarcolemmal membrane is a plasma membrane composed of phospholipids, cholesterol molecules, and glycolipids. Proteins are also embedded in the membrane and facilitate cell structure and signaling. The phospholipids form a bilayer with the hydrophilic heads facing outward and the hydrophobic tails facing inwards, creating a barrier that is impermeable to water molecules and ions. However, both ions and water molecules can cross through protein channels and pumps embedded in the membrane.

The transmembrane-bound channels that facilitate temporal changes in ion permeability are ion-specific and play a key role in the loss of activation. Figure 2.1 shows the basic structure of cardiac ion channels embedded in the sarcolemmal membrane. Ion channels are composed of multiple protein subunits that cross the membrane, with domains in the intracellular, membrane, and extracellular space. The amino acid residues in the mouth of the channels guide ions into the channel pore based on charge and size, leading to remarkable selectivity for the specific ion. Cardiac-specific sodium and calcium channels are both time- and voltage-dependent, which means that the gate blocking the channel opens depending on the voltage across the surrounding membrane. Additionally, sodium and calcium channels will close or inactivate, blocking ions from passing. Inactive channels will not reopen until the membrane has returned to a

set negative voltage for a minimum time, thus creating a refractory period during which the cell cannot depolarize again. In cardiac cells, potassium channels are responsible for repolarization and setting the membrane potential. The potassium channels that repolarize the heart are both voltage- and non-voltage-gated, with a portion being ligand-gated. The ATP-sensitive potassium channel (K_{ATP}) is one ligand-gated channel that links the metabolic state of the cell to the membrane potential and excitability.

Ion pumps and exchangers are proteins embedded in the membrane to move ions across the membrane; however, the rate of transport is much slower than that of ion channels. Pumps can be energy consuming or they can harness the energy of an ion moving down its concentration gradient to move another against its gradient. Active transport pumps move ions against their gradient at the expense of energy in the form of ATP. The most important active transport pump in the heart is the sodium-potassium pump (Na^+/K^+-ATPase), which maintains a resting membrane potential by pumping potassium into the cell and extruding sodium ions. Other important transporters in cardiac cells are the sodium calcium exchanger (NCX) and the sodium hydrogen exchanger (NHE), both of which do not consume ATP. The sodium calcium exchanger moves three sodium ions for every one calcium ion. During rest, the pump removes calcium from the cytosol as sodium moves down its concentration gradient. However, it can run in reverse mode when the intracellular sodium concentration is transiently high following depolarization and pump calcium into the cell. The one-to-one exchange of the sodium-hydrogen pump helps regulate both intracellular pH and sodium concentration.

The selective permeability of ions across the cell membrane gives rise to the membrane potential. Figure 2.2 shows the distribution of ions and resulting electrical

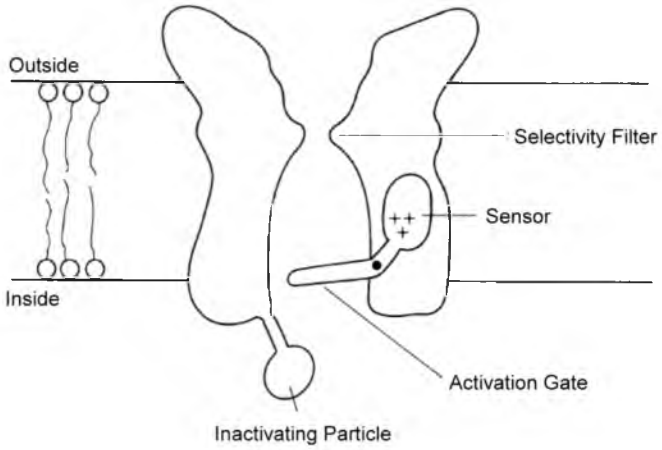

Figure 2.1. Schematic of a voltage-gated ion channel. The channel is embedded within the lipid bilayer. The voltage sensor opens the pore to allow ions to pass through the pore passing the selectivity filter. The inactivating particle closes during inactivation to prevent ions from passing. The opening of the inactivation particle is time sensitive.

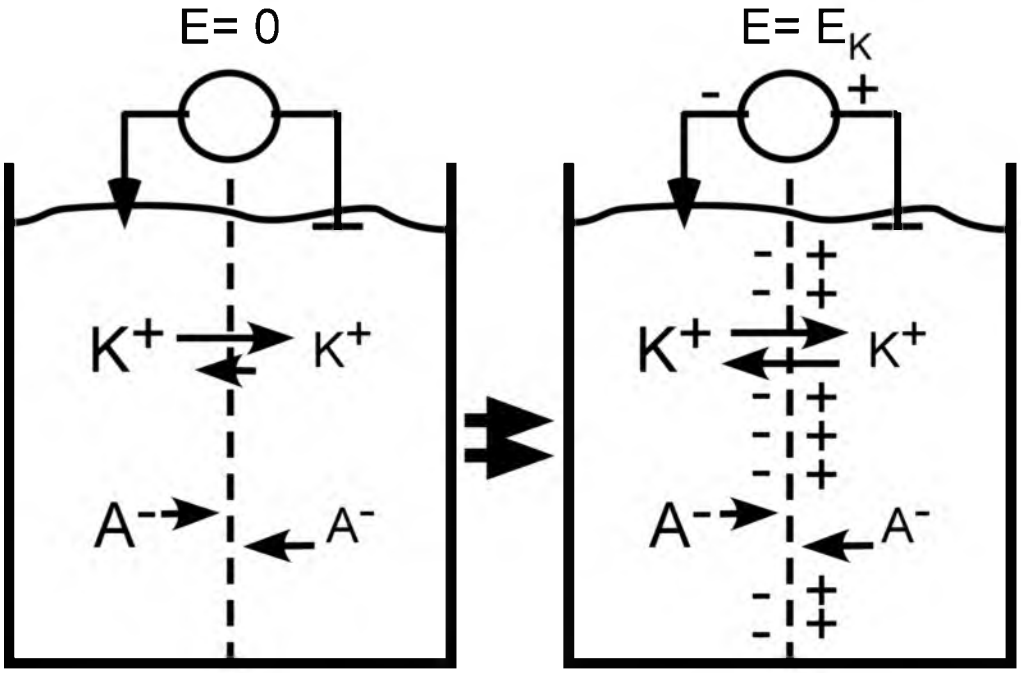

Figure 2.2. Ion diffusion and potential across a selectively permeable membrane. Different concentrations of a potassium salt (KA) are added to two chambers separated by a membrane only permeable to K. Immediately after the salt is added, K ions begin to diffuse across the membrane, creating a potential across the membrane, with the left side more negative. The membrane will eventually reach an equilibrium potential at which the diffusion of ions down the concentration gradient is balanced with the electrical pull of the positive ions back across the membrane.

gradient when potassium ions and an associated anion are added in different concentrations to two compartments separated by a membrane only permeable to potassium. In this system, potassium ions will cross the membrane down their concentration gradient. However, the movement of positively charged potassium ions and the accumulation of impermeable anions will create an electrical gradient across the membrane. An equilibrium voltage will develop across the membrane, balancing the diffusion of potassium ions down their concentration gradient and the electrical potential pulling potassium ions back towards the accumulated negative charge. This voltage is called the reversal potential and can be calculated for a specific ion using the Nernst equation (Eq 2.1). In cardiomyoctyes, potassium (K^+) is located in greater concentration

$$E_s = E_1 - E_2 = \frac{RT}{z_s F} ln \frac{[S]_2}{[S]_1} \qquad \text{Eq 2.1}$$

in the intracellular compartment of the cell (150 mM) than in the extracellular space (4 mM). Therefore, the Nernst potential of potassium is around -95mV. In contrast, the sodium (Na^+) concentration gradient drives ions into the cell, with 140 mM outside the cell and 10 mM in the cell; therefore, the Nernst potential for sodium is around +50mV. In a physiological system with many different ions present and transient membrane permeability, the cumulative membrane potential can be calculated using the Goldman-Hodgkin-Katz equation (Eq 2.2). This equation incorporates the intracellular and

$$E_{rev} = \frac{RT}{F} ln \frac{P_K[K]_o + P_{Na}[Na]_o + P_{Cl}[Cl]_i}{P_K[K]_i + P_{Na}[Na]_i + P_{Cl}[Cl]_o} \qquad \text{Eq 2.2}$$

extracellular concentration and membrane permeability for each ion. For cardiomycotes at rest, membrane potential is primarily set by potassium ions because potassium ion channels remain open at resting potentials. Therefore, the resting membrane of myocytes as calculated by the Goldman-Hodgkin-Katz equation is around -85mV.

The change in voltage across the membrane facilitated by the opening of ion channels is called an action potential (AP), and it is the cornerstone of activation in the heart. As mentioned above, the electrochemical drive for ions is to move down their electrochemical gradient and reach their Nernst potential. When the cell membrane is at resting potential, sodium ions are unable to cross the membrane to reach their Nernst potential, thus creating a driving force. However, if an external electrical current makes the intracellular potential less negative with respect to the extracellular potential (depolarization), sodium-specific ion channels within the membrane will open to allow sodium ions to pass, effectively causing the membrane to temporally be permeable to sodium. As sodium ions pass into the cell down their concentration and electrical gradients, the membrane voltage rapidly depolarizes. Sodium channels continue to open and further depolarize the membrane, but then close, after a short delay, due to the movement of the inactivation gate. This inactivation stops the positive feedback loop of sodium current-induced depolarization. Concurrently, as the membrane potential becomes more positive, the difference between the membrane potential and the Nernst potential for potassium drives potassium ions out of the cell, counteracting the depolarizing effects of sodium by moving the membrane closer to the Nernst potential for potassium. Calcium (Ca^{2+}) enters the cell early in the depolarization phase through L-type calcium channels, adding in depolarization, and causing the release of calcium from

intracellular stores known as the sarcoplasmic reticulum (SR). The calcium release from the SR is the primary source of calcium that modulates electromechanical contraction. In summary, each action potential is a summation of all the active ions currents. Figure 2.3 shows an action potential from a ventricular myocyte with the corresponding currents.

Ventricular myocytes are not able to depolarize on their own and require external stimulus. However, specialized cells located in pace-making regions, called nodal cells, spontaneously depolarize due to a different make up of ion channels. Therefore, for ventricular action potentials to fire, non-nodal myocytes must be electrically coupled to nodal cells. Action potential firing at the cardiomyocyte level is an all or nothing event, therefore providing the basis for electrical abnormalities at the level of the whole-heart, such as arrhythmias, local loss of excitability, and the global loss of excitability (asystole). If the input currents are not sufficient to depolarize the membrane to the activation voltage of sodium channels ($\approx$ -65 mV), an action potential will not fire. Figure 2.4 is a schematic of the all-or-nothing firing of action potentials. The first factor determining depolarization is the currents composing the sodium upstroke; if the membrane is not depolarized to less negative voltages, too few sodium channels will activate, and the membrane will not depolarize. Potassium channels open will then return the membrane to resting potential. The second factor contributing to AP failure is potassium currents opposing the depolarizing sodium currents. A sufficient outward potassium current counteracting depolarization can prevent AP firing by allowing depolarizing input currents to leak out of the cell. Therefore, the potassium channels relevant to metabolic stress, especially the K_{ATP} channel, can effectively prevent AP firing when their conduction is large.

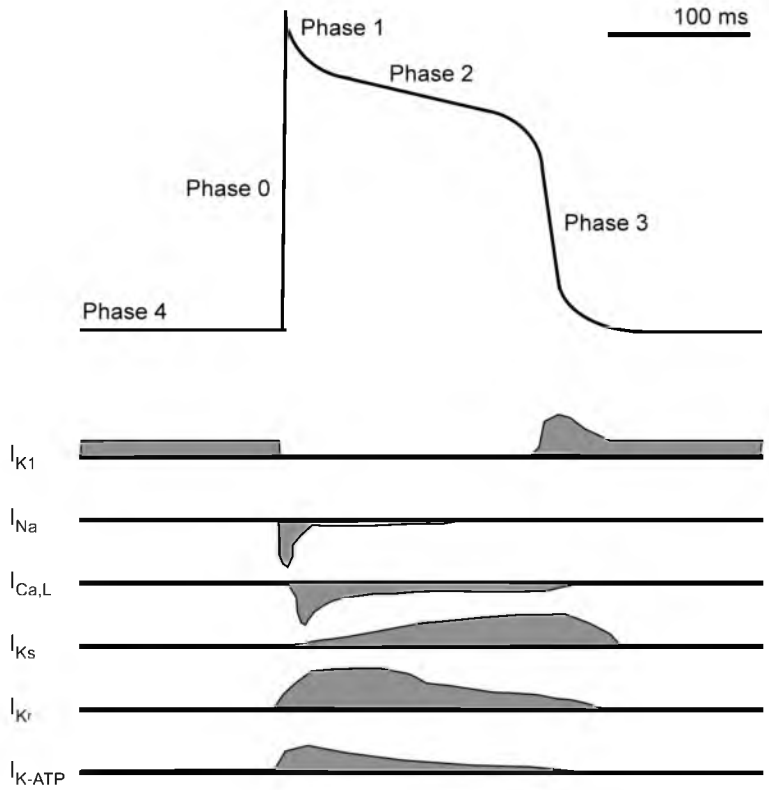

Figure 2.3 Ventricular cardiac action potential with depolarizing and repolarizing currents. I_{K1} sets the resting membrane potential and helps in Phase 3 repolarization. I_{Na} and $I_{Ca,L}$ are responsible for depolarizing the membrane (Phase 0) and maintain the Phase 2 plateau ($I_{Ca,L}$). I_{Ks} and I_{Kr} repolarize the membrane; when open, I_{K-ATP} will also drive the membrane towards the potassium Nernst potential.

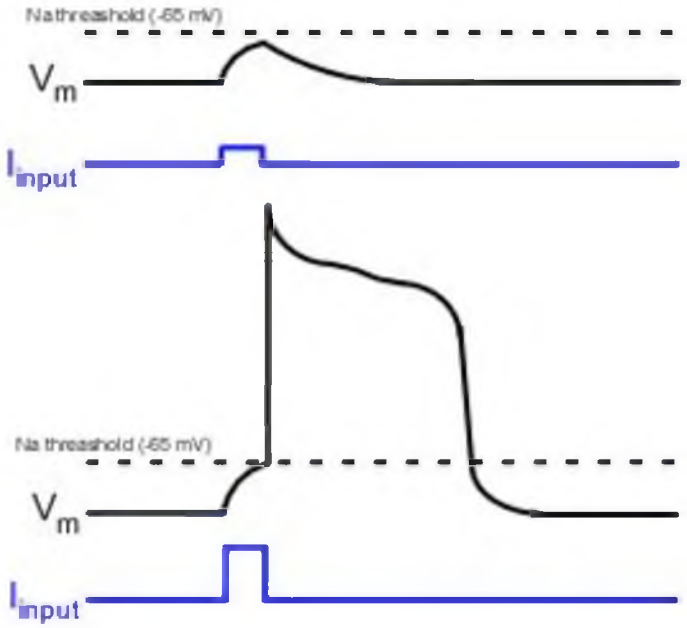

Figure 2.4. Ventricular myocytes require an input current to raise their resting membrane potential and fire an action potential. If the input current does not raise the membrane to a threshold voltage to fire an action potential, the membrane potential will return to resting potential when the input current ceases (top). If the current is large enough to raise the membrane potential above the threshold voltage, the cell will fire an action potential (bottom).

2.2 Tissue level electrophysiology and arrhythmias

The myocardium is composed of a syncytium of cardiomyocytes. The synchronous electrical activation of the heart depends on cells firing action potentials in a relatively coordinate fashion. The electrical coupling of one cardiac myocyte to its neighbor allows activation to spread across the myocardium and activate the entire heart. In the whole-heart, each heart beat initiated in the sinus node of the atria spreads through the atria to the atrioventricular node, and then depolarizes the ventricles through a series of specialized conduction pathways made up of Purkinje fibers. Depolarized cells excite neighboring resting cells through resistive intercellular channels called connexins. There are numerous connexin families within the heart, but all have the same function of passing ions and other small molecules between adjacent cells. As one cell depolarizes, current flows through open connexins into coupled resting cells. If the depolarizing current is sufficient to raise a resting cell's membrane to activate sodium channels, the coupled cell will depolarize and fire an action potential, allowing the electrical wave to continue to propagate. Figure 2.5a shows normal propagation. However, numerous factors can cause an action potential to fail to fire at the tissue level. The balance of depolarizing and repolarizing currents can lead to source-sink mismatch, as seen in Figure 2.5c and d.

At the level of a filament of connected cells, reduction of source currents can occur if too few sodium channels open. During ischemia, elevated extracellular potassium can depolarize the membrane to voltages that reduce the number of available sodium channels. Conversely, increased sink occurs when there are increased leak currents from potassium channels (possibly due to activation of K_{ATP}), clamping the

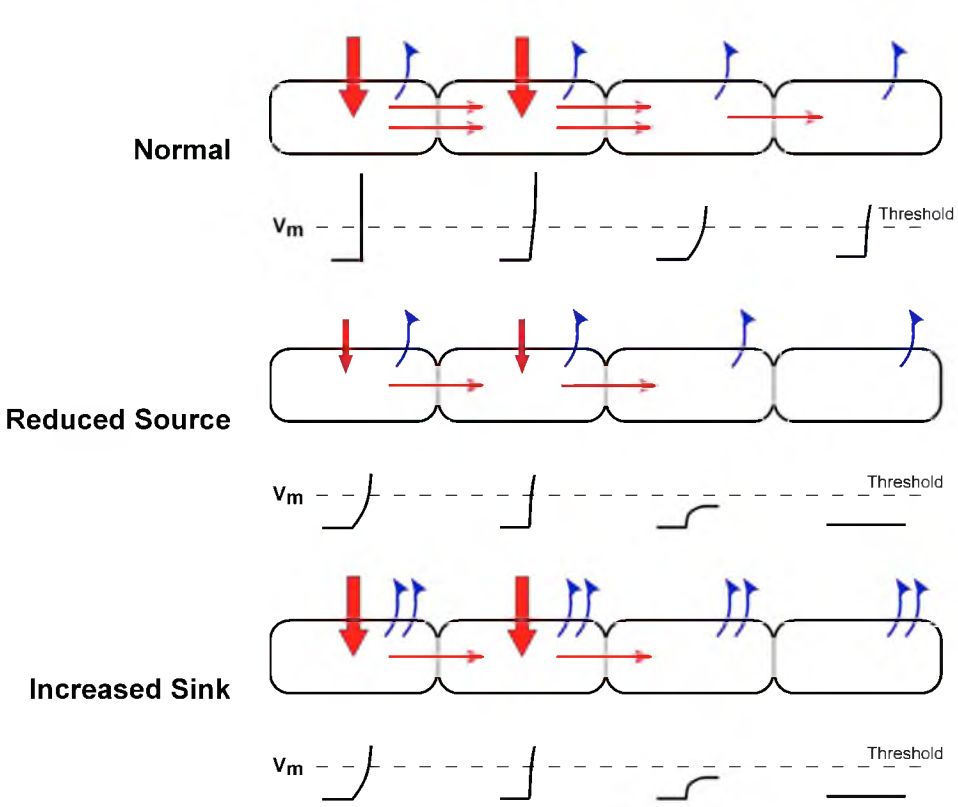

Figure 2.5. Conduction and source-sink mismatch in a one-dimensional model of cells. (A) Normal propagation occurs when input currents (red) are of large enough amplitude to overcome the outward repolarizing currents (blue) allowing propagation to continue. (B) In a reduced source situation, the input currents are too weak to overcome the outward current. (C) Conversely, in an increased sink situation, outward currents are larger than the input currents. In both reduced source and increased sink propagation fails to spread along the cells.

membrane at the resting potential and preventing sodium channel activation. At the tissue level, increased sink can also occur when a small number of cells are coupled to a larger volume of cells. In this case, the depolarizing current will dissipate into the larger mass of cells without sufficiently raising the membrane voltage. Varying degrees of source-sink mismatch can also lead to slowed propagation of the activating wave.

Source-sink mismatch, slowed conduction, and varying degrees of inexcitability provide the substrate for arrhythmias within the heart. Arrhythmias are a family of non-synchronous or irregular activations that include atrial fibrillation, ventricular tachycardia, and ventricular fibrillation. VF plays a principle role in SCA due to its asynchronous activity, which prevents ejection of blood to the coronaries of the heart, causing ischemia. A common mechanism of VF is reentry. Reentry occurs when there is an obstacle, either physical or electrical, that causes an activation wave to excite adjacent regions at different times in a circular manner. As seen in Figure 2.6, an activation wave approaches an obstacle with two pathways. The activation wave is unable to excite one branch from the initial direction of propagation (possibly due to source-sink mismatch), but can excite it from the opposite direction via the other branch. If the wave activates the blocked area from the other direction, the wave may then reactivate the other branch if it is no longer in a refractory period, creating a reentry circuit.

Another phenomenon of excitable tissue called spiral waves can also sustain ventricular fibrillation. Spiral waves occur when an activation wave rotates around a central anchoring point of polarized cells, as seen in Figure 2.7. Potassium currents at the center of the spiral wave can repolarize the membrane of surrounding cells, allowing very short action potentials and fast repolarization near the core. During ischemia, spiral

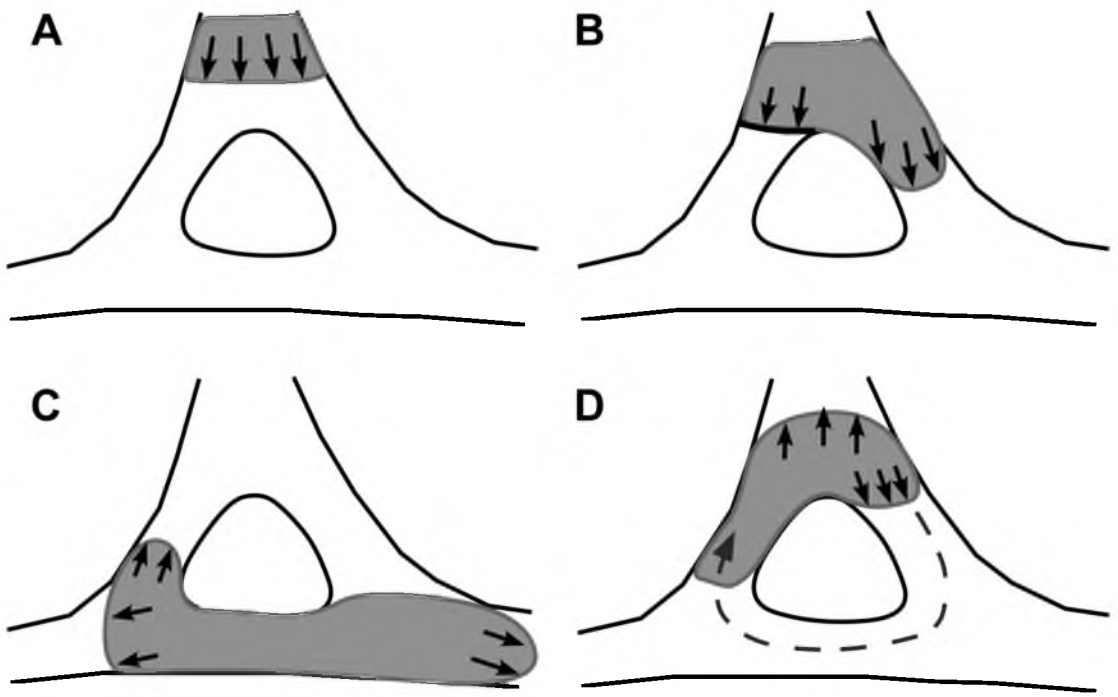

Figure 2.6. Schematic of unidirectional block and the formation of a reentry circuit. An activation wave approaches an obstacle (A); however, as the wave splits around the obstacle, activation block occurs on the left side (B). The wave continues to activate tissue on the nonblock side of the obstacle until it activates the blocked region from the other direction (C). If the tissue past the block is no longer refractory, the wave can reactivate the region, creating a reentry circuit (D).

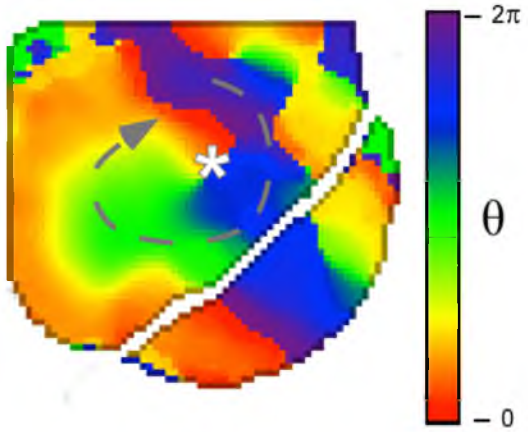

Figure 2.7. Spiral wave on the anterior right ventricular epicardium of a canine heart. The scale bar indicates the phase of the action potential. The spiral wave front propagates around the anchoring singularity point (red asterisk) in a pinwheel fashion (gray dashed line). Outward potassium currents in the center core polarize surrounding tissue, causing short APDs and DIs. Adapted from Venable et al. 2011.

waves can act as a source of wavelets, exciting peripheral myocardium. Heterogeneities in activation, including slow propagation and inexcitability, resulting from metabolic stress can cause spatially complex patterns of fibrillation characterized by a combination of spiral waves, wavelets, and reentry. Spatially complex patterns can then hinder efforts to return the heart to normal rhythm. Current research has implicated the mitochondrial dysfunction and K_{ATP} channel opening as the source of electrical heterogeneities and the link between the metabolic stress of ischemia and electrophysiology of the heart.

2.3 Mitochondria

The principle function of mitochondria is to synthesize ATP. In energy-intensive cardiomyocytes, mitochondria occupy approximately 35% of the cell volume and are tightly-coupled with the cellular contractile structures. Additionally, mitochondria play an important role in intracellular signaling pathways, such as apoptosis (8). Normally functioning mitochondria maintain a large electrochemical potential ($\Delta\Psi_m$; -180 mV inside) across the inner mitochondrial membrane (IMM) due to active pumping of H^+ ions from the mitochondrial matrix to the intermembrane space. H^+ transport is driven by the proteins of the electron transport chain (ETC), whereby oxygen is reduced to water in Complex IV. The F_1F_0-ATP synthase couples the energy of H^+ flowing down its gradient into the IMM to generate ATP (11). Mitochondria are also capable of absorbing excessive cytosolic Na^+ and Ca^{2+}. Therefore, maintenance of $\Delta\Psi_m$ is critical for both the production of ATP and cell homeostasis. Figure 2.8 shows a schematic of mitochondria, including the proteins associated with the electron transport chain, ion exchange, and the transport of fatty acids, pyruvate, and ATP across the membrane.

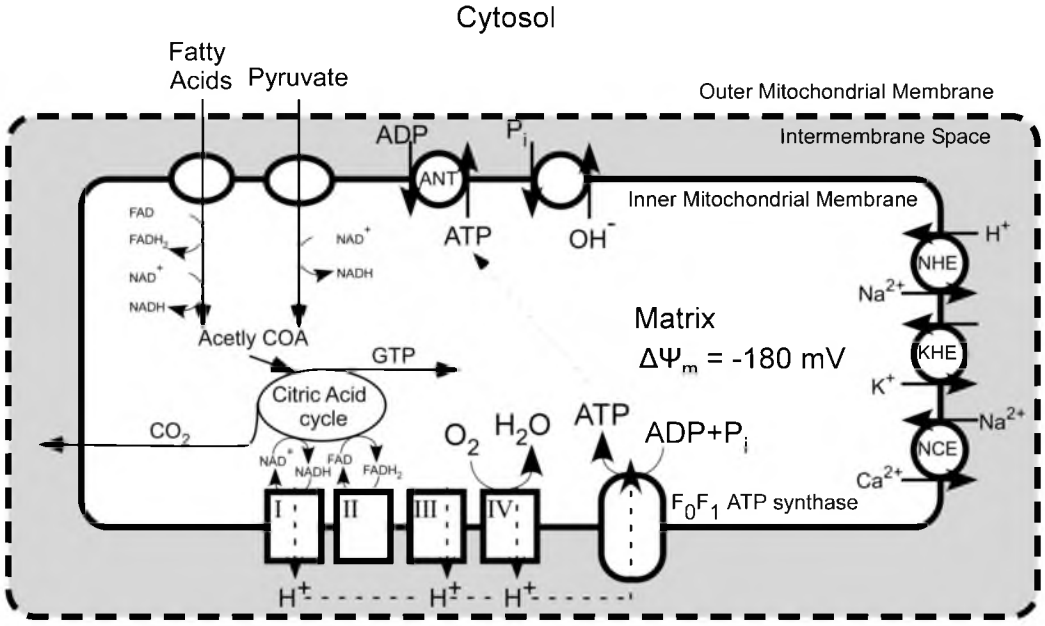

Figure 2.8. Mitochondrial ATP production and associated proteins. Postively charge H+ ions are pumped out of the mitochondria through the proteins of the electron transport change as oxygen is converted to water. During anoxic conditions like ischemia, the membrane potential is preserved by pumping H+ ions against their electrical driving force through the ATP synthase at the expense of ATP.

2.4 Postulated link between mitochondrial inner membrane depolarization and inexcitability

The collapse of $\Delta\Psi_m$ has been implicated in the development of ischemic conduction failure and postreperfusion arrhythmias during SCA (7), (2). If the electro-chemical gradient of the inner matrix that drives ATP production is not maintained, energy production will cease. Fluctuating concentrations of ATP, ADP, lactate, and other energy production by-products link the metabolic state of the cell to the membrane potential through the K_{ATP} channel (26). Physiologically, the channel's role is to shorten action potential duration at times of high energetic load. During severe metabolic stress, activation of the K_{ATP} channel leads to an increased electrical sink, potentially creating conduction failure (7). Figure 2.9 demonstrates the ability of the K_{ATP} channel to shorten APD and eventually prevent action potential firing. The highly heterogeneous nature of mitochondrial depolarization reported in the relevant literature (21) has led to the hypodissertation that mitochondrial membrane collapse can directly cause heterogeneous electrical depression and localized areas of inexcitability during ischemia, promoting arrhythmias and defibrillation failure. Investigations into the relationship between $\Delta\Psi_m$ and sarcolemmal membrane potential, especially the timing of $\Delta\Psi_m$ loss during metabolic stress, have increased in recent years (21), (29), (20). However, the increase in research efforts has yet to produce a unified view of the relationship between changes in $\Delta\Psi_m$ and major physiological outcomes of ischemia/reperfusion. The diversity of reported results is quite striking. Some groups report depolarization within the first 6 minutes (20), others report depolarization late in ischemia (21), yet others report depolarization only upon reperfusion (29). In addition, some authors report only catastrophic $\Delta\Psi_m$ loss in

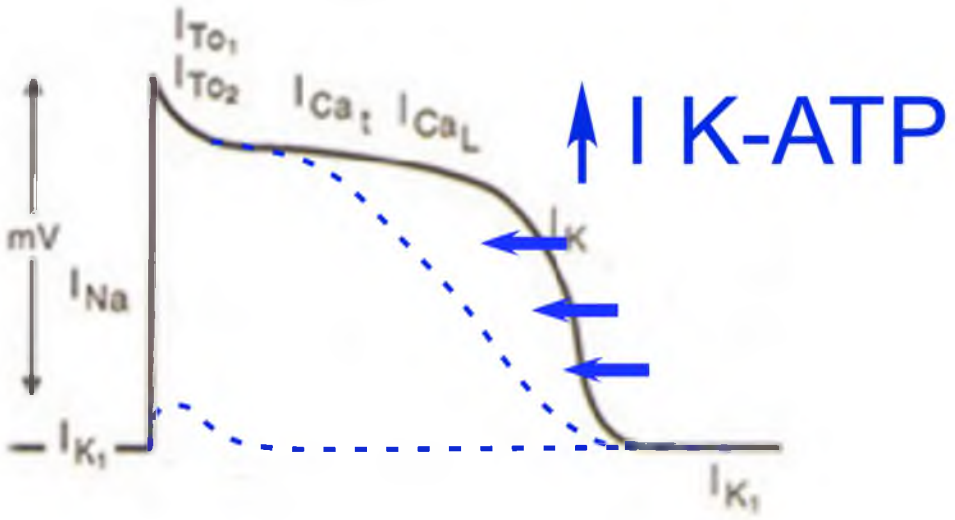

Figure 2.9. Action potential shortening and inexcitability due to increase $I_{K\text{-}ATP}$. Moderate activation of the K-ATP channel can shorten Phase 3 of the action potential. If $I_{K\text{-}ATP}$ is large enough, it can clamp the membrane to resting potential.

individual myocytes amongst apparently intact neighboring cells, whereas others report macroscopic, systemic depolarization occurring in the form of a propagating wave (20). At least in part, these discrepancies could be due to difficulties in interpreting $\Delta\Psi_m$-sensitive fluorescent signal. One important component of cellular metabolism that many of these studies fail to consider during ischemia is the ability of anaerobic glycolysis to provide ATP. ATP derived from glycolysis could provide ATP to both block K_{ATP} channel opening and maintain $\Delta\Psi_m$ through reverse hydrolysis of ATP. Therefore, $\Delta\Psi_m$ loss may not be the direct cause of inexcitability, but instead both inexcitability and $\Delta\Psi_m$ may be the result of decreased anaerobic glycolysis. Furthermore, previous studies have not addressed the effects of VF on $\Delta\Psi_m$ loss. The energetic stress of high rate activation present during VF-induced SCA could possibly alter the timing of $\Delta\Psi_m$.

2.5 Methods to study electrical activity in the whole-heart

Investigating the temporal and spatial distribution of electrical activity of the whole-heart requires a variety of methods. The two primary methods used are electrical mapping with unipolar electrodes and the electrocardiogram (ECG), and optical mapping with fluorescent probes that are sensitive to voltage changes across the membranes of the heart. Both of these methods and their respective limitations will be discussed in the following section.

Electrical mapping of the activation of the heart was one of the first methods used to study cardiac electrophysiology. The ECG is the projection of the activation vector onto the axis of two leads. For in vivo models, the ECG is taken from leads placed on the chest and abdomen. For ex vivo models, the pseudo-ECG is taken from leads adjacent to

the perfused heart. Both surface ECG and pseudo-ECG show the classical PQRS pattern during normal rhythm. Figure 2.10a shows the classical ECG pattern, with the relevant segments noted. The pseudo-ECG reading may differ slightly from that of the surface ECG, as the location of the leads with respect to the heart is arbitrary. During VF, both ECGs show a complex pattern with little to no cyclic activity. The complex pattern, shown in Figure 2.10b, is the transition from sinus rhythm to VF. Note the irregular pattern present on the ECG during VF. When the heart is in asystole, both ECGs show no activity. Although very basic, the ECG can give an accurate measurement of the electrical activity of the whole-heart. Simple analysis of the ECG can give the heart rate and the frequency of global VF. Disadvantages of using ECG recordings are variability resulting from lead placement, and the lack of quantification of activation strength, due to the effects of difference in capacitances of tissue surrounding individual hearts.

Unipolar electrograms recorded from single electrodes provide electrical information on a smaller, more localized scale. The electrodes used in the majority of research are placed on needles that are then inserted into the walls of the ventricles. Electrodes can also be mounted on baskets or socks to record from the endocardium or epicardium, respectively. As an activation wave approaches an electrode, electrical currents flow from the depolarized tissue to the resting tissue, causing the electrode to detect a rise in voltage compared to the reference electrode. As the wave front passes, the voltage quickly changes from positive to negative. The maximum negative derivative is commonly used as the time point for activation of the tissue surrounding the electrode. Figure 2.11 shows the time vs. voltage plot for a unipolar electrode as a wave passes along with the action potential for the surrounding tissue. The advantages of using

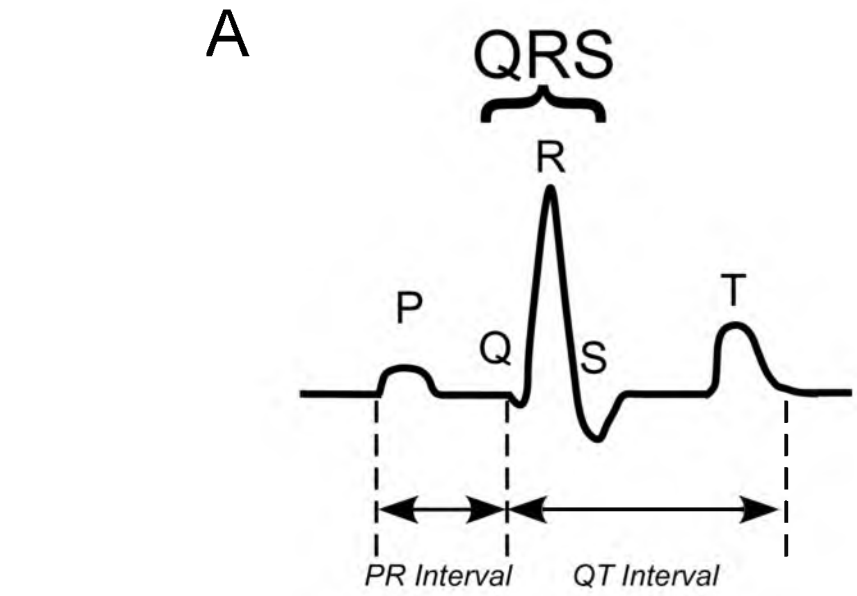

Figure 2.10. Morphology of ECG during normal sinus rhythm (A) and ECG tracing of sinus rhythm transitioning into VF (B). During sinus rhythm, an ECG will show the activation of the atria (the P-wave), the activation of the ventricles (the QRS complex), and the repolarization of the ventricles (the T wave). The PR interval is a measure of the time delay between the atrial activation and the ventricular activation. The QT interval is a measure of the duration of activation and repolarization. The nonsynchronous activation of VF appears on the ECG as an arrhythmic pattern.

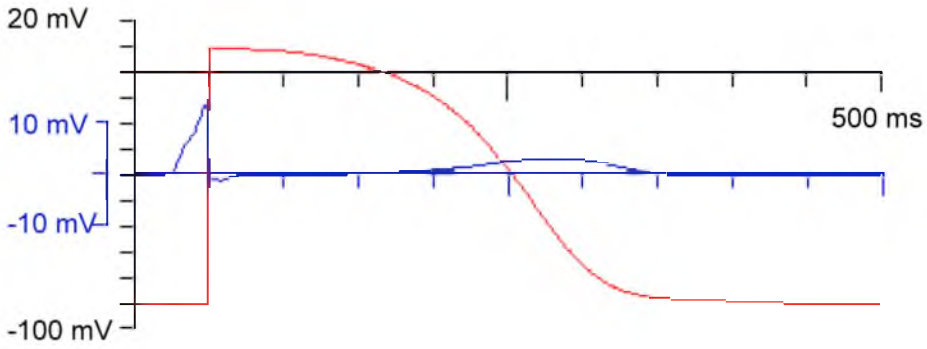

Figure 2.11. Unipolar electrogram (blue) and schematic of local action potential (red). Unipolar electrograms detect activation at a local level based on the resistance of the electrode. An approaching activation wave will cause an increase in the voltage of the electrode. When the surrounding tissue fires an action potential, as seen in the red trace, the electrode will have a rapid decrease in voltage. Repolarization will cause a slight increase in the voltage as current flows from still repolarizing to resting cells.

electrodes in cardiac electrophysiology are the ability to record electrical activity transmurally and their ability to record at a very high-frequency, which is especially important during high-frequency VF. The disadvantage of using electrodes is their relatively low spatial resolution. Electrodes record from a roughly one-millimeter volume of tissue, depending on the resistance of the tip, but are limited with respect to how densely they can be placed. Additionally, electrode recordings are highly susceptible to noise from outside electrical sources.

Optical mapping of membrane voltage is a newer electrophysiology technique that provides additional data not available through traditional electrical techniques. Optical mapping utilizes fluorescent molecules that are perfused through the heart and excited with lasers of specific wavelengths. The fluorescent molecules, or probes, can be used to monitor a variety of physiological events. Voltage-sensitive dyes, such as Di-4-ANEPPS, change their emission wavelength base on the voltage of the cell membrane. By recording the emission signal at a specific wavelength with a band pass filter, recorded Di-4-ANEPPS fluorescent signal drops during an action potential because the emission wavelength shortens when the membrane depolarizes. Other dyes fluoresce in response to changes in ion concentrations. For example, Rhod-2 increases fluorescence when intracellular calcium increases. Figure 2.12 shows an optical mapping setup used to image voltage from a Langendorff perfused heart. Due to the rapid changes in fluorescent signal, and the low signal strength of some dyes, a high-speed charge couple device (CCD) camera is used to record emission signal. The major benefits of optical mapping are a high spatial resolution and the ability to measure the action potential duration, diastolic interval, and the VF rate (VFR) when using voltage sensitive dyes, as

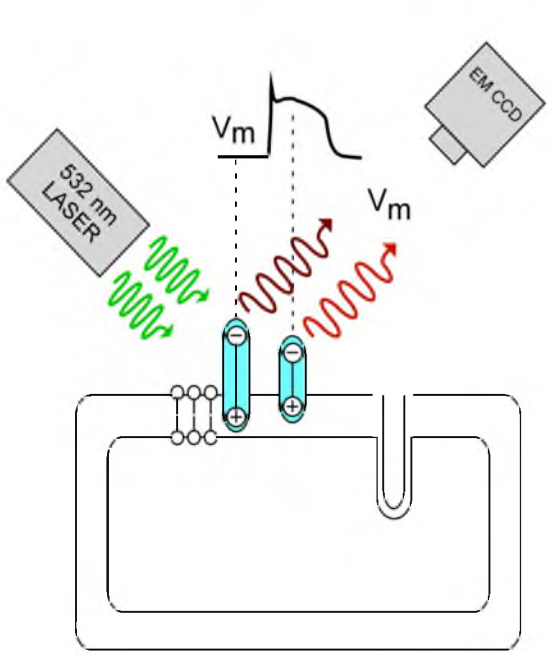

Figure 2.12. Schematic of optical mapping voltage using Di-A-ANEPPS. The dye molecule embeds into the lipid bilayer of the cell membrane and is excited by a green laser. As the membrane potential of the cell depolarizes during activation, the peak emission wavelength of the dye shifts to a shorter wavelength. A CCD camera filtering on the longer end of the emission spectrum will detect a decrease in signal as the cell depolarizes.

seen in Figure 2.13. The drawbacks of optical mapping are that it is limited to the layers of epicardial or endocardial cells. In addition, the signal can be sensitive to variability in dye distribution and laser illumination, and prolonged exposure can cause photo-bleaching and photo-toxicity.

2.6 Methods to monitor mitochondrial potential

Confocal imaging is the gold standard for imaging cellular structure and function. Traditional confocal imaging has primarily been used for single cells, but it is increasingly being used in whole-hearts, including examination of $\Delta\Psi_m$ during ischemia (21, 29). Confocal imaging is technically related to wide-field optical mapping, but is able to resolve the signal at a subcellular resolution. A confocal microscope has a similar layout to traditional inverted microscopes, but has an additional function that limits illumination and emission collection to a very small volume of tissue or cell. The area-specific imaging is achieved by mechanically limiting the illumination and emission detection using a pinhole system that restricts collection to focused photons of emission signal as it scans the imaging area. Figure 2.14 shows a schematic of a confocal microscope, with the pinhole located beneath the imaging stage. Adjusting the size of the pinhole changes the thickness of the focal plane and the volume from which photons are collected. This effectively allows cells or tissues to be imaged in very thin slices, with thicknesses less than a micrometer, by excluding excitation and emission from out-of-focus planes. Scanning using a pinhole also reduces photo-toxicity by limiting the laser exposure of the tissue. Imaging mitochondria requires the slice thickness to be comparable to that of the mitochondria, so that individual mitochondria are resolvable

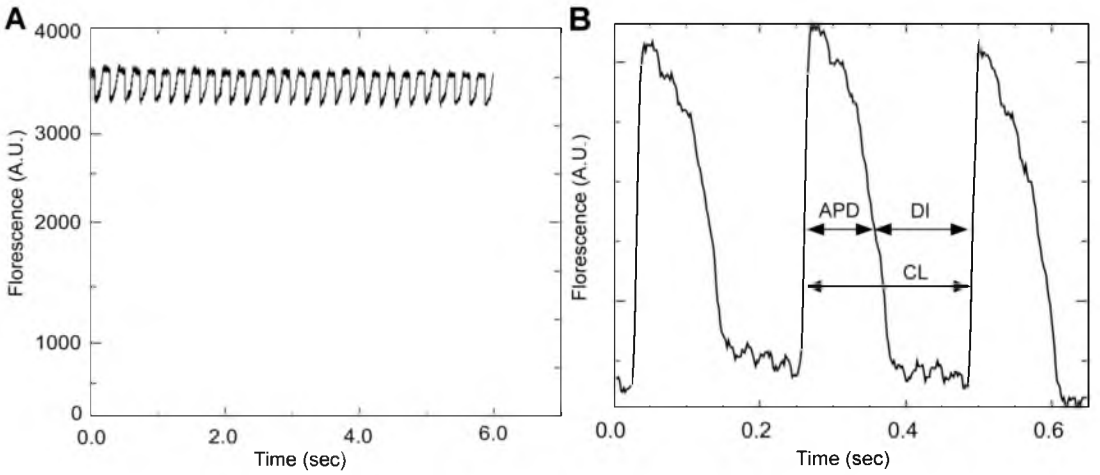

Figure 2.13. Action potentials from optical mapping of voltage-sensitive dye. (A) The unfiltered raw signal. Note the low ΔF/F. The negative shift in wavelength causes the recorded APD to be a decrease in fluorescence signal. (B) Filtered, back-ground subtracted and inverted action potentials. Diastolic interval (DI), action potential duration (APD), and cycle length can all be measured from the V_m-sensitive signal.

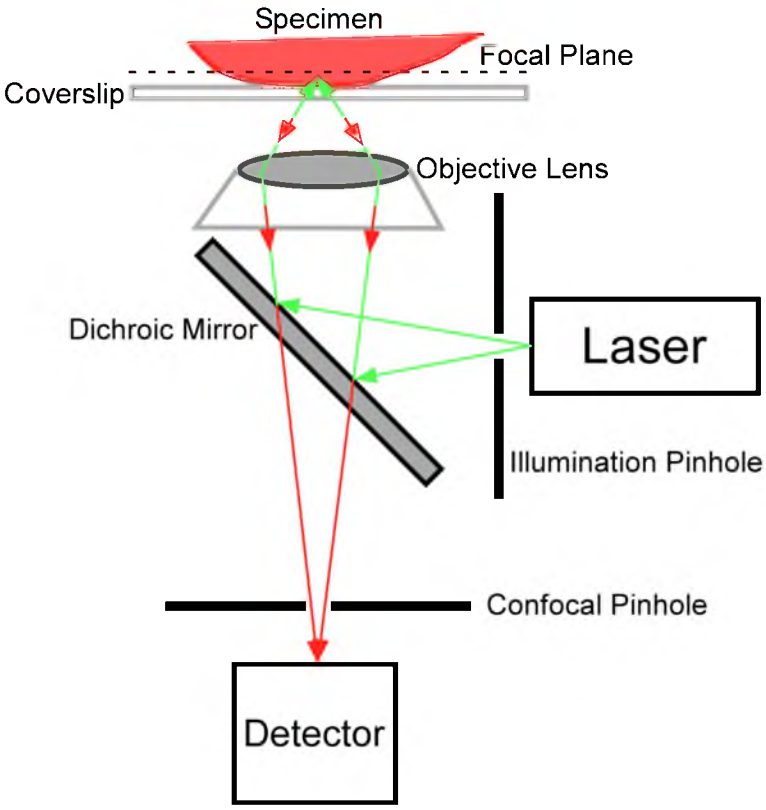

Figure 2.14. Schematic of confocal microscope. The illumination and confocal pinholes limits excitation and emission photons to the desired focal plane. Both pinholes can be adjusted to vary the thickness of the confocal slice.

instead of blurred together.

Many of the same dyes used in whole-heart optical mapping can be used in confocal imaging. The two most commonly used dyes to measure mitochondria membrane potential are tetramethylrhodamine methyl ester (TMRM) and tetramethylrhodamine ethyl ester (TMRE). TMRM distributes across the extracellular space, cytosol, and mitochondrial matrix based on a three-compartment Nernstian distribution. Figure 2.15 shows the location of TMRM dye during polarized mitochondrial membrane potential and depolarized potential. In well-polarized mitochondria, the greatest proportion of the dye is concentrated in the mitochondrial matrix, which is the most negatively charged compartment in myocytes. The loss of $\Delta\Psi_m$ leads to re-distribution of the dye between the three compartments, but under conditions of no-flow ischemia, the total amount of dye in the tissue remains the same and the total level of TMRM fluorescence may not change at all. Therefore, the traditional approach of simply measuring total fluorescence does not give reliable information about the timing of $\Delta\Psi_m$ depolarization.

2.7 Conclusion

From its onset, VF-induced sudden cardiac arrest triggers changes at the cellular metabolic and electrophysiological scale that are reflected at the whole-heart level as increasingly complex fibrillatory patterns. However, using knowledge of the fundamental principles of electrophysiology, and the variety of methods to record tissue and cellular events, research can begin to answer the root causes of inexcitability, and possibly prevent the currently irreversible state of asystole. The following chapters present

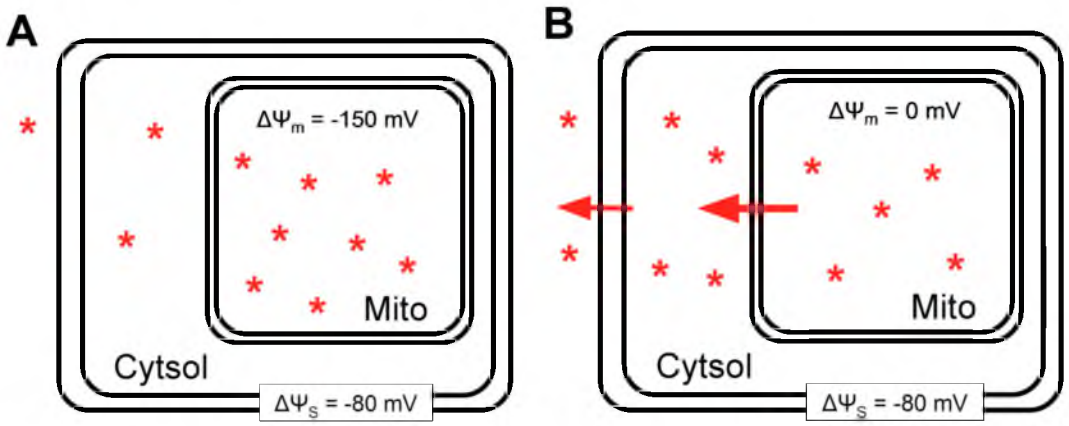

Figure 2.15. Distribution of TMRM in polarized and depolarized mitochondria. (A) When mitochondria are well polarized, TMRM preferentially distributes into the mitochondria. (B) However, if the mitochondrial depolarize, the dye redistributes into the cytosol and extracellular space. If the system is closed, like in no-flow ischemia, the total amount of dye does not change.

research on both the spatial and temporal patterns of VF during modeled sudden cardiac arrest, the tissue-level effects of blocking K_{ATP}, a new method to image mitochondrial membrane potential using confocal imaging, and the time of mitochondrial depolarization and inexcitability under normal and varying energetic conditions.

CHAPTER 3

THE TIMELINE OF THE STUDY, PROBLEMS ENCOUNTERED, AND SOLUTIONS FOUND

The overarching goal of the research presented in this dissertation is to address the causes of inexcitability and aystole in a clinically relevant model of sudden cardiac arrest (SCA). However, during the progression of research, a variety of new hypotheses developed, presenting new technical problems and requiring a new animal model. The purpose of this chapter is to explain the sequence of the study and to address problems encountered during the course of research and their respective solutions.

In order to obtain baseline data for researching the decline in the electrical activity during VF-induced SCA, the first project focused on characterizing the timing and spatial dynamics of the progressive electrical failure in a whole-heart model during the clinically relevant time frame of 10 minutes. The development of different patterns of electrical decline in different species during ischemia has been attributed to the species-specific layout of the Purkinje fibers; human, canine, and rabbit hearts have Purkinje fibers limited to the endocardium, whereas porcine hearts have fibers throughout the ventricular wall. Canine hearts were used for this project, due to the similarities in the Purkinje systems of canine and human hearts. The development of localized areas of inexcitability was a major finding of the initial studies of VF dynamics during ischemia, and became

the basis for researching the roles of K_{ATP} channels and mitochondrial membrane potential depolarization in loss of excitability.

One hypodissertation we tested was that the differences in K_{ATP} channel activation during ischemia were leading to the development of inexcitable areas. Testing this hypodissertation did not require significant changes to the protocol or animal model. However, to rule out the possibility that the K_{ATP} channel blocker glybenclamide was affecting other potassium currents, we incorporated additional studies that modulated these currents pharmaceutically and then compared the VFR response to that of ischemic glybenclamide blockade.

Investigating the role of mitochondrial membrane potential on localized inexcitability required both a change in imaging method and animal model. To resolve events at the cellular level, a new confocal imaging method was required. Confocal imaging allows subcellular imaging by restricting the excitation and emission photons to a narrow plane and the use of a high-magnification lens. Three different confocal imaging approaches were considered: the Nipkow spinning disk system, the Leica FCM 1000, and the LSM Zeiss confocal microscope, which was ultimately used. The Nipkow spinning disk creates a confocal image by collecting the emission light through a small pinhole arranged on a rapidly spinning disk located between the CCD camera detector and the magnification lens. The benefits of the system are that the time required to scan the imaged area is very short, and the system can be mounted in a traditional optical mapping setup. However, the system that we used had filters that prevented us from exciting the heart with a laser optimized for TMRM, therefore limiting the strength of the signal. Figure 3.1 shows a TMRM image of epicardial myocytes from a canine heart acquired

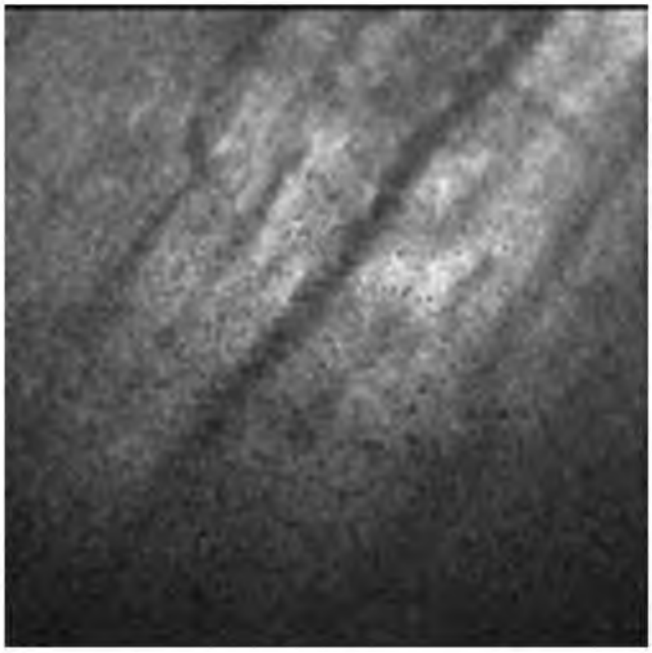

Figure 3.1. TMRM signal from canine epicardial myocytes acquired with a Nipkow spinning disks. Notice the poor signal strength and the low resolution.

with the Nipkow disk in initial testing of the system. While individual cells are visible, the signal is very low. The Nipkow system utilized an Andor camera, which has a maximum resolution of 128 pixels X 128 pixels. With the μm/pixel resolution when imaging with a 20X lens (an optimal magnification to image a group of 20 cells), we would not have been able to detect the spacing of the mitochondria. This would have prevented us from using the spatial Fourier transform method developed in the second project to detect depolarization during no-flow ischemia. Additionally, the disk itself did not spin at a consistent speed and created an artifact in the signal.

The Leica FCM 1000 system confocally images tissue through a fiber optic probe. Confocal slice thickness and magnification are dictated by the properties of the probe itself. The transportability of the system and the flexibility of the probe are major benefits of the FCM. However, in our attempts to image TMRM signal in the whole-heart, we were not able to clearly image mitochondria. This most likely is due to the fact that the available probe had a beveled tip that was not optimized for imaging the epicardium. Another disadvantage with the FCM, as with the Nipkow system, was its low resolution of 128 X 128 pixels.

The Zeiss confocal system was ultimately chosen due to its high resolution (2048 X 2048 maximum), optimized filters, and high laser power. Additionally, previous studies of mitochondrial depolarization in whole-hearts using a similar two-photon Zeiss system produced high-quality images of myocytes and mitochondria (21). However, the Zeiss system required the development of an independent, portable perfusion system, a new electrophysiology recording system, and an imaging chamber that accommodated an isolated heart and the associated Langendorff perfusion plumbing. Each of these

requirements was completed with the help of the CVRTI core.

Building on the results from the first project, we wanted to test whether mitochondrial depolarization was the cause of regional inexcitability in the epicardium of canine hearts. In order to replicate regional inexcitability, our initial confocal studies used isolated, blood perfused canine right and left ventricles. However, this model had a number of technical and physiological disadvantages. We initially attempted to image the epicardium of the heart, but found that the epicardial layer of cells created a barrier of sufficient thickness to prevent imaging of the underlying myocardium. Imaging myocardium on the endocardium was limited due to the concave curve of the ventricles, which prevented the heart from being flat against the imaging glass. Additionally, a layer of Purkinje cells completely covered the myocardium. While imaging the mitochondrial potential of Purkinje fibers would be an interesting research pursuit, it was beyond the scope of our original goal to monitor mitochondrial dynamics in myocytes. A two-photon confocal system might have been able to overcome this issue due to the increased photon penetration depth; however, a two-photon system was not available. Therefore, we decided to switch our animal model to isolated aortic perfused rabbit hearts. Rabbit hearts are similar to canine (and human) hearts in that the Purkinje fibers are isolated to the endocardium; however, the epicardial cell layer of rabbit hearts is thin enough to allow for imaging of the epicardial myocytes. Characterizing VF dynamics during ischemia, research from other groups and our own have also reported the presence of local inexcitability (41), as seen in Figure 3.2.

The interpretation of TMRM signal during ischemia also presents a unique technical problem. Prior studies of mitochondrial membrane dynamics during ischemia

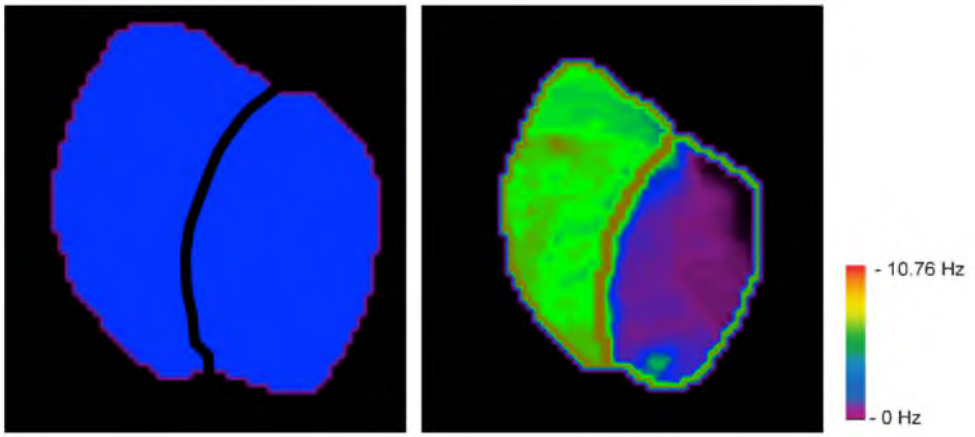

Figure 3.2. Ventricular fibrillation rate in ischemic rabbit hearts. VFR is a measure of activations in a period of time and is shown in Hz at baseline (left) and ischemia (right). At baseline, the activation is homogeneous across the epicardium. However, after 18 minutes of ischemia, the right ventricle is activating at a faster rate than the left ventricle and there are areas with no activation.

analyzed TMRM signal using a decrease in total fluorescence as an indicator of mitochondrial membrane potential depolarization. This method is used with reliable results in isolated cells models of ischemia that rarely model no-flow ischemic conditions. When using this analysis technique in a whole-heart model of ischemia, we could not detect depolarization, even in the presence of a known mitochondrial uncoupler such as FCCP. To address this analysis problem, we developed a new analysis method that uses spatial Fourier transform to detect the redistribution of TMRM molecules from the mitochondria to the cytosol following mitochondrial membrane potential depolarization. The validation of the SFT method is addressed in the sixth chapter.

CHAPTER 4

COMPLEX STRUCTURE OF ELECTROPHYSIOLOGICAL GRADIENTS EMERGING DURING LONG-DURATION VENTRICULAR FIBRILLATION IN THE CANINE HEART

The research in this chapter was published in the *American Journal of Physiology: Heart and Circulatory Physiology*. Paul W. Venable, Tyson G. Taylor, Junko Shibayama, Mark Warren, and Alexey V. Zaitsev.: 'Complex structure of electrophysiological gradients emerging during long-duration ventricular fibrillation in the canine heart.' Am J Physio Heart Circ Physiol, 2010, 299, pp H1405-H1418. Reprinted with permission of the American Physiology Society.

Am J Physiol Heart Circ Physiol 299: H1405–H1418, 2010.
First published August 27, 2010; doi:10.1152/ajpheart.00419.2010.

Complex structure of electrophysiological gradients emerging during long-duration ventricular fibrillation in the canine heart

Paul W. Venable,* Tyson G. Taylor,* Junko Shibayama, Mark Warren, and Alexey V. Zaitsev
Nora Eccles Harrison Cardiovascular Research and Training Institute, University of Utah, Salt Lake City, Utah

Submitted 30 April 2010; accepted in final form 25 August 2010

Venable PW, Taylor TG, Shibayama J, Warren M, Zaitsev AV. Complex structure of electrophysiological gradients emerging during long-duration ventricular fibrillation in the canine heart. *Am J Physiol Heart Circ Physiol* 299: H1405–H1418, 2010. First published August 27, 2010; doi:10.1152/ajpheart.00419.2010.—Long-duration ventricular fibrillation (LDVF) in the globally ischemic heart is a common setting of cardiac arrest. Electrical heterogeneities during LDVF may affect outcomes of defibrillation and resuscitation. Previous studies in large mammalian hearts have investigated the role of Purkinje fibers and electrophysiological gradients between the endocardium (Endo) and epicardium (Epi). Much less is known about gradients between the right ventricle (RV) and left ventricle (LV) and within each chamber during LDVF. We studied the transmural distribution of the VF activation rate (VFR) in the RV and LV and at the junction of RV, LV, and septum (Sep) during LDVF using plunge needle electrodes in opened-chest dogs. We also used optical mapping to analyze the Epi distribution of VFR, action potential duration (APD), and diastolic interval (DI) during LDVF in the RV and LV of isolated hearts. Transmural VFR gradients developed in both the RV and LV, with a faster VFR in Endo. Concurrently, large VFR gradients developed in Epi, with the fastest VFR in the RV-Sep junction, intermediate in the RV, and slowest in the LV. Optical mapping revealed a progressively increasing VFR dispersion within both the LV and RV, with a mosaic presence of fully inexcitable areas after 4–8 min of LDVF. The transmural, interchamber, and intrachamber VFR heterogeneities were of similar magnitude. In both chambers, the inverse of VFR was highly correlated with DI, but not APD, at all time points of LDVF. We conclude that the complex VFR gradients during LDVF in the canine heart cannot be explained solely by the distribution of Purkinje fibers and are related to regional differences in the electrical depression secondary to LDVF.

ischemia; optical mapping; inexcitability

VENTRICULAR FIBRILLATION (VF) is a major cause of sudden cardiac death. The spatiotemporal organization of VF evolves as global ischemia progresses and alters electrophysiological properties of the myocardium. Concurrent with the metabolic and electrophysiological changes, the chance of successful defibrillation and resuscitation diminishes with every minute of VF, approaching zero at ~10 min after the onset of VF (31). Unfortunately, the delayed response time of emergency medical services often approaches the time when successful resuscitation is unlikely. This perhaps explains the fact that the overall survival of victims of out-of-hospital cardiac arrest is a dismal 5% (14). The mechanisms determining successful defibrillation and survival under these conditions remain poorly understood but may be related to the nature of the sources maintaining VF (reentrant or focal) and electrical depression caused by ischemia, culminating in a complete loss of electrical response (asystole). The evolution of the organization of VF lasting 10–20 min in the globally ischemic heart [termed long-duration VF (LDVF)] has been the focus of several recent studies (2, 5, 8, 15, 19, 20, 27, 34, 42). These studies revealed large gradients in the VF activation rate (VFR) between the left ventricular (LV) endocardium (Endo) and LV epicardium (Epi) in the dog and the rabbit but not in the pig. In the rabbit heart, a transmural VFR gradient is present only in the LV but not in the right ventricle (RV) (42). Based on principal differences in the organization of Purkinje fibers in these species (exclusively Endo in the dog and rabbit vs. transmural in the porcine heart), as well as analysis of the directionality of the transmural wave propagation in the dog and pig, the differences in the organization of LDVF between the dog and pig were interpreted in terms of the leading role of focal activity (e.g., abnormal automaticity) arising from Purkinje fibers in maintaining advanced stages of LDVF (2, 8, 34). The idea of focal sources driving VF is a significant shift of the current paradigm of VF based on the notion of reentry in the form of spiral waves and may have important implications for defibrillation and resuscitation during LDVF. Recently, an elegant study (19) using a transmural multilevel optrode in the LV showed that the gradient in VFR is mostly determined by the gradient in the diastolic interval (DI), whereas the action potential (AP) duration (APD) remains conserved across the LV wall as the LDVF evolves. This can be interpreted as evidence that a gradient of excitability and/or postrepolarization refractoriness occurs across the LV wall, which enables Endo to support more rapid activations during LDVF. The presence of such a gradient may be due to the transmural distribution of ionic channel properties unrelated to but coincidental with the distribution of Purkinje fibers. Thus, the question arises as to whether the sites of the fastest activation at advanced stages of LDVF are universally associated with Endo, where Purkinje fibers are localized in the canine heart.

In that regard, it is important to note that in addition to the transmural VFR gradient, optical mapping studies (4, 42) in the rabbit heart have revealed a large Epi VFR gradient between the RV (faster activation) and LV during LDVF. However, little is known about right-to-left gradients during LDVF in large mammalian hearts, in particular in the canine heart, which is considered to be the closest to the human heart in terms of the dynamics of LDVF (2). The purpose of this study was to provide a comprehensive description of both transmural and lateral [RV to septum (Sep) to LV] electrophysiological gradients during LDVF in the canine heart during the first 10 min of LDVF using information from both transmural needle electrodes and high-resolution Epi optical mapping. From optical data, we analyzed the distribution of APD, DI, and sustained sources of activation in the RV and LV during

* P. W. Venable and T. G. Taylor contributed equally to this work.

Address for reprint requests and other correspondence: A. V. Zaitsev, Cardiovascular Research and Training Institute, Univ. of Utah, 95 S. 2000 E., Salt Lake City, UT 84112-5000 (e-mail: zaitsev@cvrti.utah.edu).

LDVF. Our results revealed an unprecedented complexity of electrophysiological gradients emerging during LDVF, with large heterogeneities both between chambers as well as locally within each chamber. Importantly, the magnitudes of interchamber and intrachamber VFR gradients were comparable to the magnitude of the transmural gradient, with Epi sites at the RV-Sep junction being activated as fast as LV Endo. We also found that Epi right-to-left VFR gradients were determined by the gradients in DI amid relatively constant APD, which is similar to the pattern observed transmurally across the LV wall (19). We concluded that VFR gradients during LDVF in the canine heart cannot be fully explained by special properties of Purkinje fibers but may be universally determined by nonuniform electrical depression reflected in the prolongation of postrepolarization refractoriness and eventual loss of excitability. We propose possible factors contributing to the highly nonuniform response of the canine heart to the stress imposed by LDVF and global ischemia.

METHODS

This investigation conformed with the National Institutes of Health *Guide for the Care and Use of Laboratory Animals* (NIH Pub. No. 85-23, Revised 1996). The animal protocols were approved by the Institutional Animal Care and Use Committee of the University of Utah. A total of 19 dogs were used in this study (5 dogs for the multielectrode mapping of LDVF in situ, 10 dogs for the optical mapping of LDVF in isolated hearts, and 4 dogs for the assessment of regional differences in refractoriness during global ischemia in isolated hearts).

Experiments in situ. Five dogs of either sex (30.8 ± 10.5 kg) were anesthetized with acepromazine (0.1 ml/10 kg) and pentobarbital sodium (32.5 mg/kg). Anesthesia was maintained through intravenous injections of pentobarbital sodium. Intubation was accomplished with a cuffed endotracheal tube, and mechanical ventilation was maintained at 10–15 cycles/min (tidal volume: 15–20 ml/kg). The heart was exposed via a midline sternotomy. The chest opening was covered with polyethylene film, and warm, humidified air was blown into the chest to maintain temperature at the surface of the heart between 35 and 37°C during LDVF. Lead I ECG was recorded continuously throughout the experiment. Blood gases, pH, electrolyte concentrations, and glucose were analyzed in arterial blood samples before the onset of VF. Plunge needle electrodes with 10 evenly spaced unipolar leads were manufactured in house following the design developed by Rogers et al. (30). Electrodes in the LV had an interlead distance of 1.6 mm, and those in the RV and Sep had an interlead distance of 1.2 mm. Three needle electrodes were inserted in the anterior RV, one in the Sep, and three in the anterior LV, as shown schematically in Fig. 1*A*. The distance between needles was 10–15 mm. Needles were placed along a transverse plane bisecting the heart approximately at half-distance between the apex and base. The Sep needle was placed just to the right of the left anterior descending coronary artery (LAD). VF was induced by a brief (~1 s) application of current from a 9-V battery to the RV outflow tract. Unipolar electrograms from all contacts of the needle electrodes were recorded continuously during the first 10 min of VF at a sampling rate of 1 kHz using a custom-made multichannel data-acquisition system, as previously described (35).

Electrode data analysis. Unipolar electrograms were analyzed using custom software developed in a Matlab framework. Activations were chosen as the maximum negative derivatives that exceeded a minimum of 3 V/s within a 20-ms search window, which is similar to previously described approaches (8, 9). VFR was calculated as the average number of activations per second over 10-s intervals taken at 10 s after VF induction and at *minutes 1-9* of LDVF. For simplicity, the first time point is referred to as *minute 0* of LDVF.

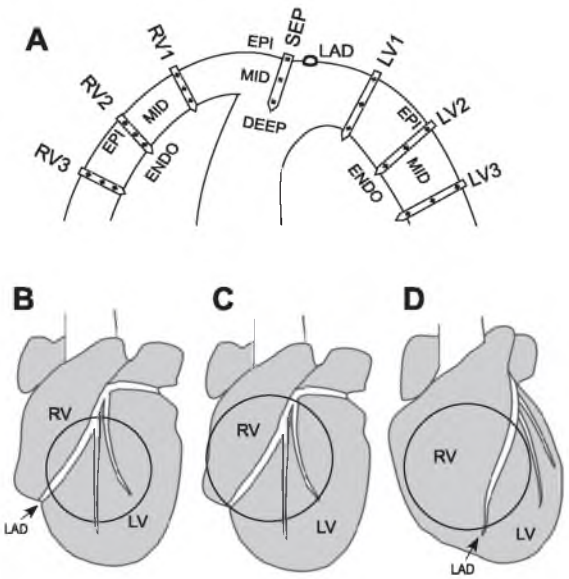

Fig. 1. Schematic representation of the mapping modalities used in this study. *A*: approximate positions of the plunge needle electrodes. RV1, RV2, and RV3 indicate electrodes in the right ventricle (RV). LV1, LV2, and LV3 indicate electrodes in the left ventricle (LV). The electrode in the anterior projection of the interventricular septum (Sep) is also shown. All electrodes were in the transverse plane located at approximately middistance between the base and apex. The epicardial (Epi) and midmyocardial (Mid) leads in the plunge needle electrodes are indicated, as is the endocardial (Endo) lead in the RV and LV electrodes. Deep indicates the lead in the Sep electrode that is the most distant electrode from Epi and is located in the depth of Sep. See text for more detail. *B–D*: three positions of the imaged area (circles) used in the optical mapping experiments. *B*: the imaged area mostly covers the LV with a narrow region of the RV. *C*: the imaged area covers approximately equal portions of the RV and LV. *D*: the imaged area mostly covers the RV with a narrow region of the LV. LAD, left anterior descending coronary artery.

Whereas the length of the RV and LV needles was constant and designed to span the largest thickness observed in the respective chambers of the canine heart, the actual thickness of the ventricular wall is highly nonuniform, especially in the RV. Thus, in some cases, plunge needle electrodes were longer than the wall thickness at the site of insertion. The contacts outside the ventricular wall were excluded from analysis based on the following criteria: *1*) low VFR at 0 min of LDVF (slower by 5 Hz or more compared with the average VFR measured in all locations), *2*) decrease of VFR to below 2 Hz within the first minute of LDVF, and *3*) observation of a progressively decreasing electrogram amplitude toward more distal leads while maintaining the same morphology as more proximal leads in the same needle. In the latter case, the most proximal lead from the group of leads with identical morphology was designated as the Endo location in the needle. This approach could potentially falsely reject some of the true Endo leads in the RV and LV and thus underestimate the magnitude of the Endo-to-Epi difference in VFR, which, however, would not affect the main conclusions of this study (this issue is further discussed in *Limitations*). The position of the Epi lead could be easily ensured by visual inspection. After determination of the most distal lead in contact with the myocardial wall (Endo), the midmyocardial (Mid) lead was chosen as the one closest to being equidistant between Epi and Endo. Note that, unlike in RV or LV needles, the most distal recording site in the Sep needle was always in the depth of

the Sep (see Supplemental Material, Supplemental Fig. 1).[1] Accordingly, in the Sep needle, we identified the Epi, Mid, and Deep sites for the purposes of analysis and comparison with RV and LV locations. At later stages of LDVF, some electrograms appeared to lack any local activation. However, due to a far-field signal always being present in unipolar electrograms, it was sometimes difficult to ascertain a clear-cut case of complete loss of excitability. Therefore, local inexcitabilty was defined in unipolar electrograms when VFR fell below 0.5 Hz, whereas at least some other leads in the same experiment exhibited fibrillatory activity with VFR > 4 Hz.

Experiments in isolated hearts. Hearts were obtained from dogs of either sex (n = 14, 27.5 ± 2.7 kg) after premedication, anesthesia, and surgery performed as described above. After isolation via a midline sternotomy, the heart was perfused in a Langendorff apparatus with a mixture of blood and Tyrode solution as described in detail in our previous publications (16, 43). Briefly, the blood-Tyrode mixture was oxygenated (5% CO_2-95% O_2), heated (37°C), and filtered using standard pediatric heart perfusion units from various vendors. The whole mixture was collected for recirculation with collector tubes inserted into the RV and LV via cuts in the appendages of the respective atria. The heart was then placed in a temperature-controlled bath with heated water-jacketed transparent glass walls. The bath was filled with warmed Tyrode solution, which was continuously pumped, without recirculation, at a rate 80–150 ml/min. The O_2 content in the superfusate was removed by continuous gassing with a 95% N_2-5% CO_2 mixture. Temperatures in the LV cavity, superfusate, and water jacket were maintained at 37 ± 0.5°C during both normal coronary perfusion and ischemia. The gradient of temperature across the LV wall did not exceeded 1°C. Ten hearts were used for the optical mapping of LDVF. In four additional hearts, we performed programmed stimulation during global ischemia to access regional differences in refractoriness (see Supplemental Figs. 6–8).

Optical recordings. Optical mapping of activation during VF was performed using an electron-multiplied charge-coupled device camera (iXon DU-860D, Andor Technology, Belfast, UK) with a 6- or 12-mm objective lens (Computar, Commack, NY) at a resolution of 64 × 64 pixels and frame interval of 2 ms. Excitation light came from a 532-nm green solid-state laser (Coherent, Santa Clara, CA), and the fluorescent signal was filtered with a 640 ± 50-nm filter (Omega Optical, Brattleboro, VT). The voltage-sensitive dye di-4-ANEPPS (Molecular Probes, Carlsbad, CA) was delivered to the heart as a bolus via an injection into the aortic cannula. The field of view covered portions of Epi of the anterior RV, Sep, and LV. Even though the sites immediately adjacent to the LAD most certainly overlay the Epi projection of the Sep, the exact boundaries between the Sep and RV and LV free walls could not be reliably determined for the purposes of optical mapping. Therefore, in optical maps, we followed previously used approaches (4, 32, 42) and defined the area to the right of the LAD as the RV and the area to the left of the LAD as the LV (Fig. 1*B*). The size of the field of view varied between 40 × 40 and 65 × 65 mm. Due to the relatively large size of the dog heart and curvature of the ventricular wall, it was not possible to have large portions of both ventricles simultaneously in the field of view. Therefore, optical mapping experiments were divided into three subgroups. In the first group (n = 4), the field of view predominantly covered the LV with a rim of the RV ~15 mm wide. In the second group (n = 3), the areas to the right and left of the LAD were approximately equal. In the third group (n = 3), the field of view predominantly covered the RV with a rim of the LV ~15 mm wide. The approximation of the respective fields of view is schematically shown in Fig. 1*B*. To minimize motion artifacts, the heart was gently pressed against the glass chamber wall as previously described (16, 43). No electromechanical uncouplers were used.

[1] Supplemental Material for this article is available online at the *American Journal of Physiology-Heart and Circulatory Physiology* website.

The heart was perfused with blood before the onset of LDVF; however, immediately before the induction of ischemia, the perfusion was switched to Tyrode solution with the dual purpose of ensuring constant composition of the extracellular milieu at the onset of LDVF and enhancing the voltage-sensitive signal for the purpose of better resolving low-amplitude signals at advanced stages of LDVF. VF was induced using a 9-V direct current battery 10 s to 5 min before the onset of global ischemia initiated by interruption of aortic perfusion. No perceptible differences in the measured parameters were found between experiments depending on the duration of VF before the onset of ischemia; therefore, in all experiments, the time of LDVF was counted from the moment when perfusion was stopped. LDVF was maintained for 10 min; 4–6-s-long movies were acquired every 30 s. After the last LDVF movie, the perfusion pump was restarted, and additional movies were acquired every minute during 5 min of reperfusion.

Analysis of optical signals. Spatial distributions of VFR, APD, and DI at different time points during LDVF were estimated in optical mapping data using custom routines developed in PV-Wave software (Visual Numerics, Boulder, CO). The dominant frequency of the Fourier spectrum was not used to estimate VFR because it did not reliably represent the perceived number of activations per unit of time at advanced stages of LDVF, when the AP is characterized by very short APD and long DI. Instead, we used an algorithm to detect individual APs in single-pixel recordings, similar to that described in our previous publication (16). In brief, the depolarization and repolarization phases of each optical AP were detected. The time points at which the depolarization and repolarization phases crossed a line drawn at the 40% level of the absolute maximum in the respective signal (ΔF_{max}) were determined. From these time points, APD, DI, and VF cycle length (VFCL) could be calculated for each cycle. The algorithm rejected noise based on thresholds set for APD (<10 ms), VFCL (<30 ms), absolute AP amplitude (<15 levels of brightness), and percent AP amplitude with respect to the time sequence maximum (<5% of ΔF_{max}). VFR maps were created by dividing the number of APs by duration of the analyzed movie. Areas with no APs detected throughout the entire movie were considered to be inexcitable and having a VFR = 0. Such areas were counted for the purposes of determining the average VFR but were excluded from the calculation of average APD and DI. Singularity points were identified in Hilbert-transformed movies of voltage-sensitive fluorescence as points where all AP phases converged, as previously described (13, 39). Rotors were defined as singularity points that lasted for more than one cycle of rotation. The maximal lifespan and maximal number of rotations of rotors were computed for the RV and LV at 0 and 6 min of LDVF.

Statistical analysis. Within the data collected from the plunge needle electrodes, the time course of VFR was statistically compared in a 3 × 3 grid of principal locations (RV Epi, RV Mid, RV Endo, Sep Epi, Sep Mid, Sep Deep, LV Epi, LV Mid, and LV Endo; see Fig. 1A). In each experiment, the RV and LV were represented by average values from all three electrodes in the respective chambers. Two-way ANOVA was performed with a post hoc Bonferroni test to make all 36 pairwise comparisons of the VFR time course between the 9 locations (see Supplemental Table 1). Note that the statistical significance indicated the differences between the means at all time points of LDVF in different locations. No conclusions regarding differences at individual time points were possible due to the prohibitively large number of required pairwise comparisons.

In the data collected from optical recordings, average values of VFR, APD, and DI were calculated for areas to the right (RV) and left (LV) of the LAD. Despite differences in the distribution of the field of view between the RV and LV in different experiments, the average values for the two areas were similar; therefore, data from all optical mapping experiments were combined into respective regions. Two-way ANOVA was performed with a post hoc Bonferroni test to compare the time course of VFR, APD, and DI during LDVF between the RV and LV. Similar to the statistical treatment of the electrode

data, the statistical significance indicated the differences between the mean values of measured parameters at all time points of LDVF. A linear regression analysis was performed to correlate the mean APD versus the mean VFCL and the mean DI versus the mean VFCL throughout all time points analyzed during LDVF. Data are expressed as means ± SE. Differences at $P < 0.05$ were considered statistically significant.

RESULTS

Multielectrode mapping in situ. Representative examples of unipolar electrograms obtained from plunge needle electrodes inserted into the RV, Sep, and LV are shown in Fig. 2. At 0 min of LDVF, VFR was relatively uniform among all locations and all layers. At 10 min of LDVF, a prominent Endo-to-Epi gradient in VFR was typically observed in both LV and RV free walls (Endo faster), whereas in the Sep, the fastest VFR was observed in Epi or Mid locations with slower VFR in the Sep Deep. After 3 min of LDVF, the sites of the fastest VFR in the RV occurred in Endo in four of five (80%) experiments; in one experiment, VFR was uniform across the RV wall. In the LV, the fastest sites were in Endo in three of five (60%) of experiments; in the other two experiments, Endo and Mid had similar VFRs, with both being faster than Epi VFR. In the Sep, the fastest sites were in Epi and/or Mid in 100% of the experiments, with Sep Deep locations being consistently slower than Sep Mid locations. In many cases, we observed what appeared to be a complete lack of activation in some electrograms. Such events occurred starting from ~4 min of LDVF and were often local, so that adjacent needles or different contacts in the same needle still reflected some activation. Using our criterion for inexcitability (see METHODS), local inexcitability was most frequently observed in LV Epi and RV Epi (100% and 60% of experiments, respectively). Much less frequent were cases of inexcitability in LV Endo, RV Endo, RV Mid, LV Mid, and Sep Deep locations (20% of experiments in each case). Finally, inexcitability was never observed in Sep Epi and Sep Mid.

Figure 3 shows the average time course of VFR during the first 9 min of LDVF in the nine ventricular locations shown in Fig. 1*A* (RV Epi, RV Mid, RV Endo, Sep Epi, Sep Mid, Sep Deep, LV Epi, LV Mid, and LV Endo). Data for individual experiments are shown in Supplemental Fig. 2. In both Fig 3 and Supplemental Fig. 2, the wall types are distinguished by different colors (LV, red; Sep, green; and RV, blue) and the distance from the Epi surface is indicated by different symbols (Epi, circle; Mid, square; Endo, triangle; and Sep Deep, ×). Note that in Fig. 3 the VFR curves are presented redundantly in *A–C* and *D–F*. Figure 3, *A–C*, groups the curves by wall type and thus facilitates a visual analysis of transmural gradients. Figure 3, *D–F*, on the other hand, groups the same curves by depth and thus highlights the lateral gradients (between the LV, Sep, and RV) at each depth.

Figure 3*A* shows the time course of VFR during LDVF at three transmural levels in the LV. Consistent with previous results, the difference between Endo, Mid, and Epi progressively increased over time of LDVF, with LV Endo being consistently the fastest location. Note, however, that the largest gradient occurred in the outer half of the LV wall, between Mid and Epi. Accordingly, the time course of VFR was significantly different ($P < 0.05$) between Endo and Epi and between Mid and Epi but not between Endo and Mid.

Figure 3*B* shows the time course of VFR at three transmural levels in the Sep. It is important to note that the Sep Deep location was at approximately the same distance from Epi as RV Endo but at least 4–5 mm away from any Endo surface (see Fig. 1*A*). Within the Sep, Epi and Mid VFR curves stayed very close together throughout the first 9 min of LDVF. After 3 min of LDVF, VFR in Sep Epi and Sep Mid stabilized at ~7 Hz, whereas VFR in Sep Deep continued to fall, leading to a progressive separation of the Sep Deep curve from both Sep Epi and Sep Mid. This separation, however, did not reach statistical significance due to the relatively large variation between individual experiments (see Supplemental Fig. 2).

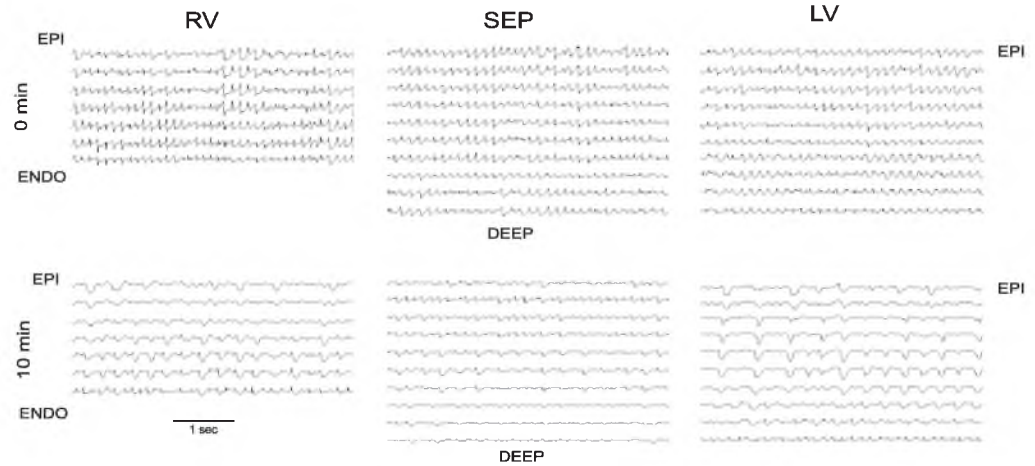

Fig. 2. Unipolar electrograms recorded from different leads of plunge needle electrodes during long-duration ventricular fibrillation (LDVF) in a representative experiment. *Top*: 0 min of LDVF; *bottom*: 10 min of LDVF. Shown are recordings from the RV3 (*left*), Sep (*middle*), and LV3 (*right*) electrodes. See Fig. 1*A* for electrode locations and other definitions.

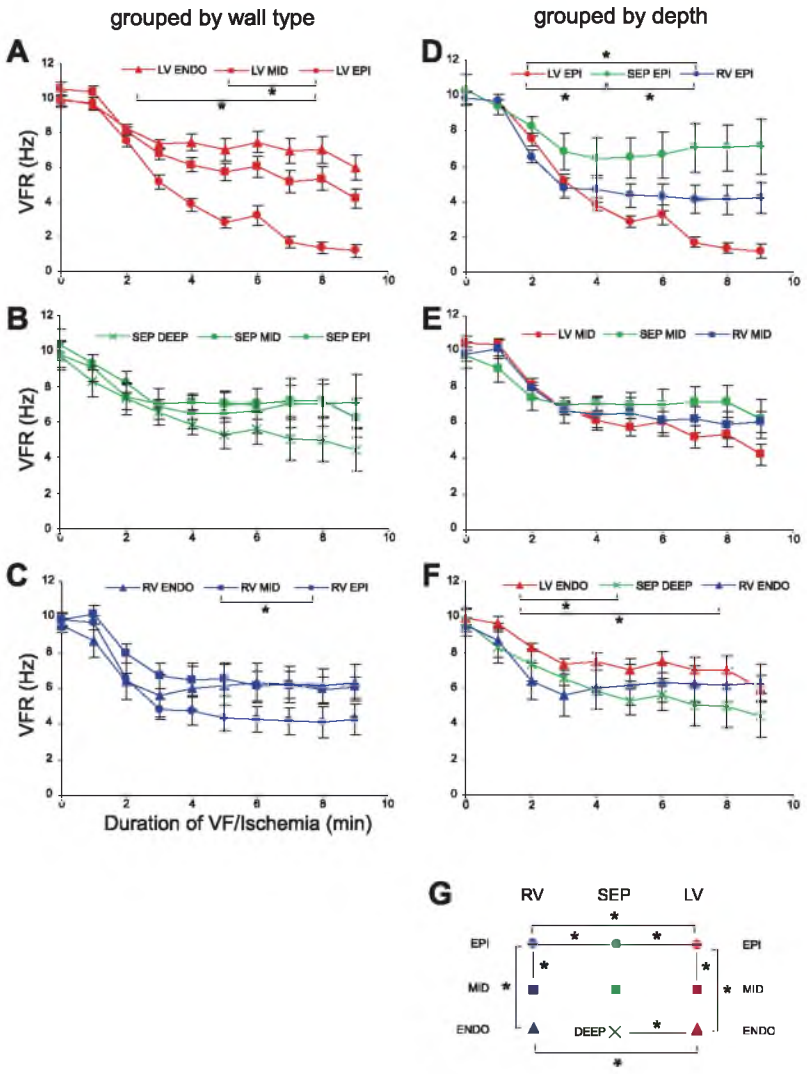

Fig. 3. Time course of VF activation rate (VFR) in a matrix of 3 × 3 of nine principal locations (LV Endo, LV Mid, LV Epi, Sep Deep, Sep Mid, Sep Epi, RV Endo, RV Mid, and RV Epi) during 0–9 min of LDVF. Colors indicate different wall types (LV, red; Sep, green; RV, blue). Symbols indicate different distances from Epi (Endo, triangles; Mid, squares; Epi, circles; Sep Deep, ×). *A–C*: the nine VFR curves grouped by wall type (LV, Sep, and RV, respectively). *D–F*: the same nine VFR curves grouped by distance from Epi (Epi, Mid, and Endo/Deep, respectively). *Statistically significant difference between the VFR curves by two-way ANOVA. *G*: summary of statistically significant differences in VFR time courses between different locations.

Figure 3*C* shows the time course of VFR at three transmural levels in the RV. RV Mid was faster than RV Epi throughout the entire course of LDVF, with the difference being statistically significant ($P < 0.05$). However, there were no significant differences between RV Endo and RV Mid. Thus, the transmural VFR gradient in RV was present mostly between Mid and Epi layers. Note that VFR in all RV layers reached a plateau after 3–4 min of LDVF, similar to Sep Epi and Sep Mid, but dissimilar to all LV layers and Sep Deep.

Figure 3, *D–F*, shows the same data as Fig. 3, *A–C*, but grouped by the distance from Epi. Figure 3*D* shows the VFR time course in the Epi layer of the LV, Sep, and RV. In all Epi locations, there was an initial decrease in VFR up to 3 min of LDVF, which was slightly faster in LV Epi and RV Epi than in Sep Epi. After that, however, VFR in RV Epi and Sep Epi stabilized (albeit at different levels), whereas VFR in LV Epi continued to fall. As a result, VFR was significantly different between all pairs of Epi locations ($P < 0.05$), with Sep Epi being the fastest, RV Epi intermediate, and LV Epi slowest.

Figure 3*E* shows the VFR time course in the Mid layers of the LV, Sep, and RV. There was very little difference in the VFR time course between these locations during the first 3 min of LDVF. After that, the curves slightly diverged, with Sep Mid being the fastest, LV Mid slowest, and RV Mid in between. In a way, this pattern repeats the divergence observed in Epi locations (see Fig. 3*D*) but at a much lower scale. As a result, there were no statistical differences between VFR time courses in all Mid locations.

Finally, Fig. 3*F* shows the VFR time course in Endo layers of the LV and RV and the Deep layer in the Sep. The LV Endo location was consistently faster than both RV Endo and Sep Deep, although LV Endo and RV Endo converged by 9 min of LDVF.

The differences between LV Endo and RV Endo and between LV Endo and Sep Deep were statistically significant ($P < 0.05$). Figure 3*G* diagrammatically shows the VFR gradients in the directions tangential and perpendicular to the anterior ventricular wall. The results of all pairwise comparisons between the nine measured locations are shown in Supplemental Table 1.

The data presented above can be summarized as follows: *1*) VFR is uniform over all locations at the onset of LDVF; *2*) during LDVF, there are significant right-to-left gradients in Epi and Endo but not in Mid; *3*) the largest transmural gradients in both the LV and RV develop between Mid and Epi, whereas the gradient between Endo and Mid is modest in the LV and practically nonexistent in the RV; and *4*) overall, LV Epi exhibits the largest and Sep Epi the smallest decline in VFR during LDVF, so that the largest overall difference in VFR during LDVF was observed between Sep Epi and LV Epi. Figure 4 further highlights the special role of the Sep in the pattern of activation during LDVF, showing that in all experiments the highest Epi VFR was observed either in Sep Epi or the adjacent RV Epi location (electrode RV1). Finally, it is worth noting that throughout the entire length of LDVF studied, the VFR time course was very similar in LV Endo, Sep Mid, and Sep Epi (see Supplemental Fig. 3). Since Sep Epi and Sep Mid do not have Purkinje fibers and are not adjacent to LV Endo in canine hearts, these data indicate that Purkinje fiber distribution and function may not be the main determinants of the VFR time course during LDVF.

Optical mapping in isolated hearts. The purpose of optical mapping experiments was to analyze the right-to-left and intrachamber gradients in VFR, APD, and DI during LDVF with high spatial resolution. Typical examples of VFR distribution maps and individual optical recordings during LDVF are shown in Fig. 5. In the experiment shown in Fig. 5*A*, the field of view predominantly covered the LV and a small portion of RV. At the onset of LDVF, the VFR distribution was relatively uniform, and there were no large-scale differences between the LV and RV. At 8 min of LDVF, the VFR distribution was markedly heterogeneous, with the fastest domain (~4.5 Hz, green) situated in the RV and LV adjacent to the LAD. The largest part of the LV was activated at a VFR of ~3 Hz (blue). Importantly, there was an area in the LV with an extremely low activation rate (<1 Hz, dark purple). The single-pixel recordings (Fig. 5*A*, *sites a*--*c*) were selected in such a way as to represent the three major frequency domains in the LV observed at 8 min of LDVF. At the onset of LDVF, the activation rate was similar between the three locations. However, at 8 min of LDVF, *site a* was the fastest, *site c* was intermediate, and in *site b* there was a single large-amplitude AP followed by a few small deflections, which are most likely due to electrotonus from the adjacent *site c*. Based on selected threshold criteria (see METHODS), our algorithm picked only the first (large) AP during the 4-s recording in *site b* compared with many more in *sites a* and *c* (asterisks in Fig. 6*A*). Note that *site c*, which exhibited a rhythmic series of suprathreshold APs,

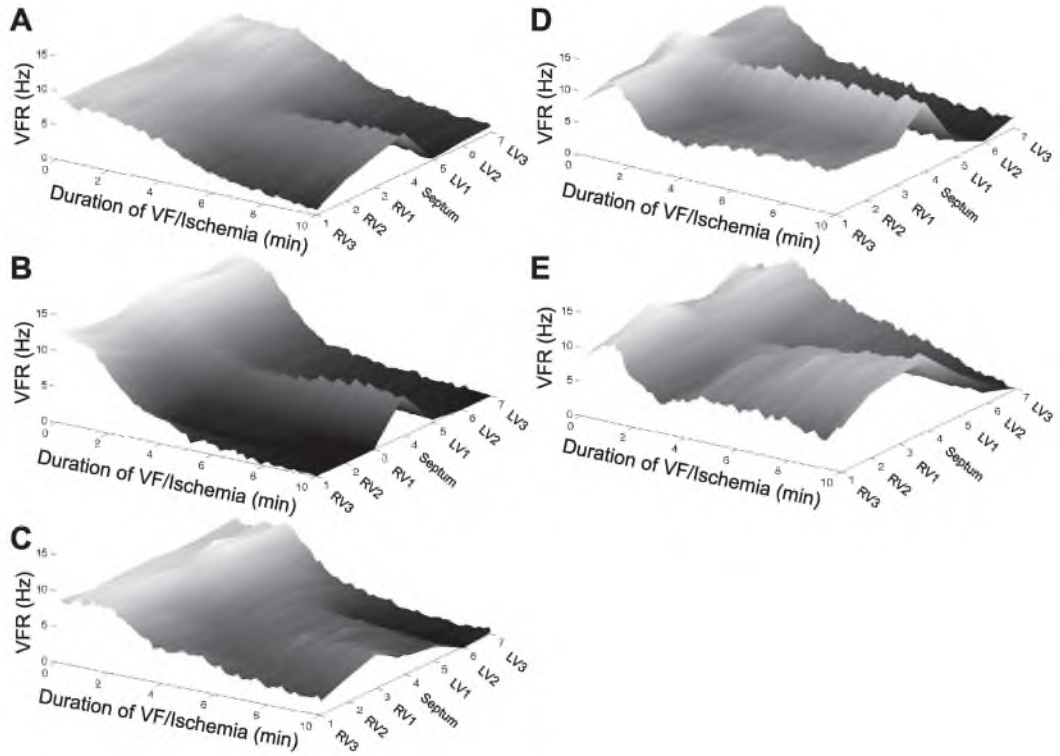

Fig. 4. Epicardial distribution of VFR during LDVF in five experiments in situ (*A*–*E*). Lighter shades of grey indicate higher VFR. Note that in all experiments there is a local maximum in Epi VFR distribution either in the Sep or adjacent RV position (RV1) after 3–4 min of LDVF.

was only ~2 mm away from *site b*, which was barely excitable. *Site b* became completely silent by 10 min of LDVF, whereas the RV-Sep portion and rightmost part of the LV were still excitable (not shown).

In the experiment shown in Fig. 5*B*, the field of view predominantly covered the RV and a small portion of LV. Similar to the preceding example, at the onset of LDVF, the VFR distribution was relatively uniform, and there were no large-scale differences between the LV and RV. At 10 min of LDVF, however, the VFR distribution was extremely heterogeneous. The highest VFR was observed in an apical part of RV (~6 Hz, green). There were also two active areas in the more basal portions of the RV (~3 Hz, blue), whereas the rest of the RV and the visible region of the LV had a VFR below 1 Hz (dark purple) or were completely inexcitable (black). Individual recordings from *sites a-c* showed similar fast activations at the onset of LDVF and striking differences at 10 min of LDVF. Specifically, *site a* exhibited fast and highly periodic activity, *site b* was completely silent, and *site c* was also highly periodic but was activated at half the rate of *site a*. Waves originating in the 6-Hz domain (green) did not propagate into the 3-Hz domain (blue) within the field of view. In fact, these two domains were separated by a thin inexcitable area (indicated by a white arrow in Fig. 6*B*) such that the waves from both domains converged and stopped at this area (not shown). Yet, *sites a* and *c* were phase locked in a 2:1 pattern, as shown in Fig. 5*C*. Indeed, activation in *site c* followed every other activation in *site a* with a fixed time delay. Thus, unless this is a perfect coincidence, which is highly unlikely, *site c* is electrically connected to *site a*, perhaps via an intramural excitable pathway.

A highly heterogeneous VFR distribution with patches of inexcitable areas in the RV and LV, as shown in Fig. 5, was typical for advanced stages of LDVF (after 4–5 min of no perfusion). The transitions between high and low VFR could be very sharp, with local VFR gradients reaching 4–5 Hz/mm (not shown). A common feature of VFR maps was the presence of the highest VFR in the RV localized near the LAD. Examples of heterogeneous VFR maps from each optical mapping experiment are shown in Supplemental Fig. 4. Consistent with the presence of areas with VFR = 0 in VFR maps, activation maps showed areas of no activation at advanced stages of LDVF (see examples in Supplemental Fig. 5*D*).

Figure 6 shows a quantitative analysis of the differences between the RV and LV that emerged during LDVF. Figure 6*A* shows that the average VFR was consistently higher in the RV than in the LV throughout 10 min of LDVF, with the exception of 0 min of LDVF. Figure 6*B* shows that average DI was longer in the LV than in the RV. Figure 6*C* shows that average APD was slightly shorter in the LV than in the RV between 2 and 8 min of LDVF. Note that whereas DI increased quickly during LDVF in both the LV and RV, APD changed little with time of LDVF in both chambers. Finally, Fig. 6*D* shows percentages of excitable areas in the LV and RV maps as a function of LDVF duration. Note that after 3 min of LDVF, the

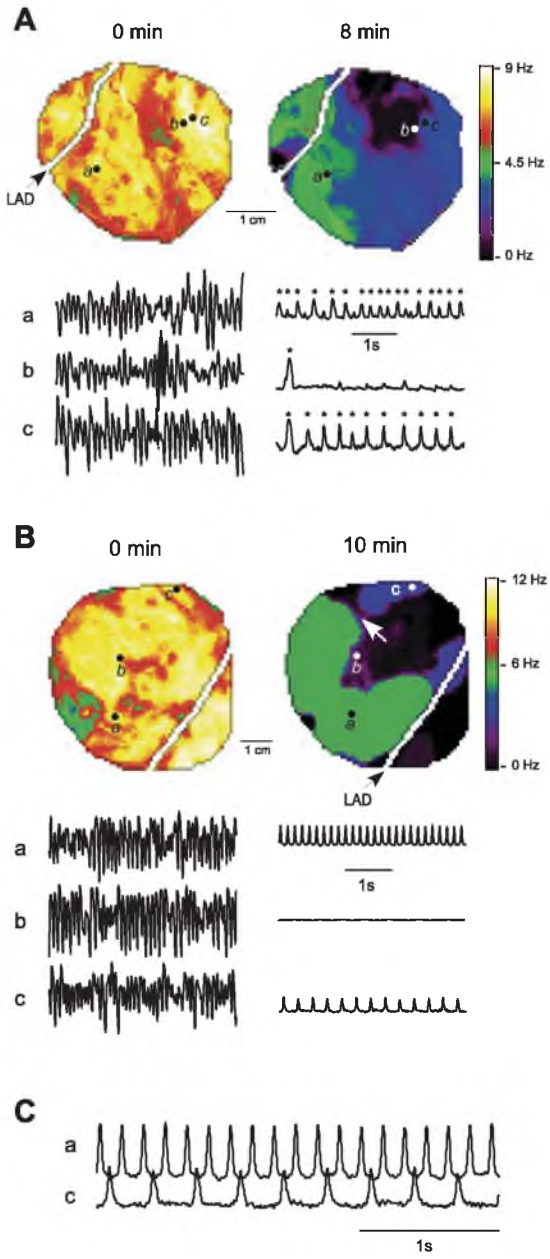

Fig. 5. Examples of VFR distribution measured in Epi optical maps in isolated hearts at the early and late stages of LDVF. *A*: experiment with predominantly LV optical mapping. *Top*, VFR maps at 0 min (*right*) and 8 min (*left*) of LDVF. *Bottom*, single-pixel recordings from *sites a–c* (indicated on the respective VFR maps with circles). *B*: experiment with predominantly RV optical mapping. *Top*, VFR maps at 0 min (*right*) and 10 min (*left*) of LDVF. The arrow in the 10-min map indicates a thin inexcitable area (black, VFR = 0) separating two active areas (green, VFR ~ 6 Hz; blue, VFR ~ 3 Hz). *Bottom*, the same layout as in *A*. *C*: single-pixel recordings of *sites a* and *c* from *B* shown with an expanded time scale. Note the fixed 2:1 phase relationship between activations in these two locations, suggesting that *sites a* and *c* have a common source of excitation even though they do not communicate within the imaged area. Note the extremely high level of VFR heterogeneity in both the RV and LV at the advanced stages of LDVF.

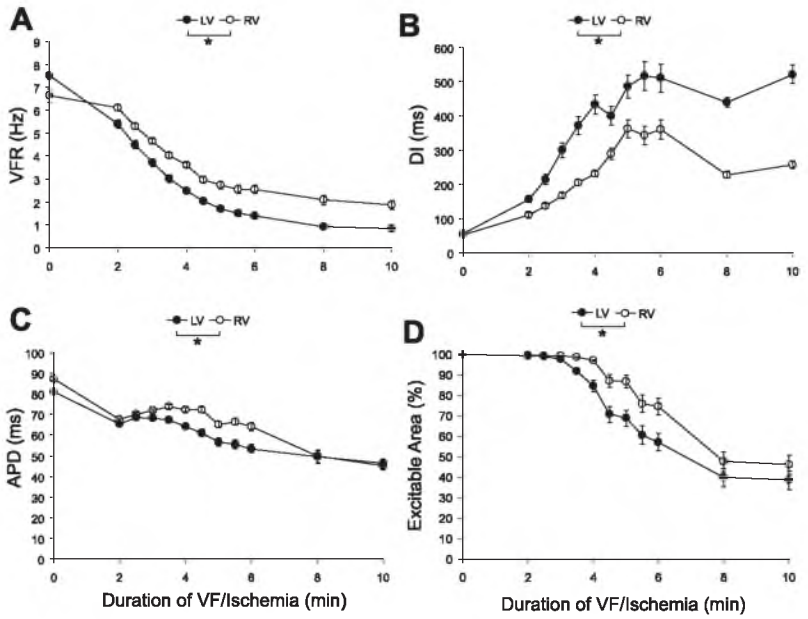

Fig. 6. Right-to-left differences in the time courses of VFR (*A*), diastolic interval (DI; *B*), action potential duration (APD; *C*), and percentage of excitable area (*D*) in Epi optical maps during LDVF. *Statistically significant difference between respective curves by two-way ANOVA.

percentage of the excitable area in the LV progressively decreased, followed by a similar decrease in the RV after an ~1-min delay. The differences between the time courses of all measured parameters in the RV versus LV were statistically significant using two-way ANOVA ($P < 0.05$).

Figure 7 shows that average VFCL (inverse of VFR) was strongly correlated with the duration of average DI in both chambers at all time points during LDVF. In contrast, VFCL was only weakly inversely correlated with the average APD. Thus, VFCL was not determined by APD dispersion but rather by dispersion in DI, which reflects the degree of postrepolarization refractoriness. It should also be noted that no functional relationship could be found between APD and the preceding DI at any stage of LDVF (not shown), which is consistent with previous reports (16, 19).

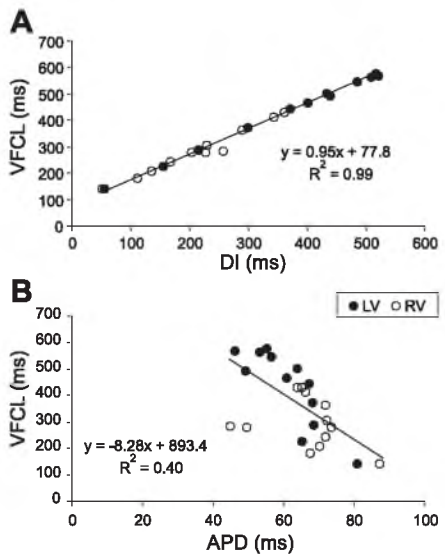

Fig. 7. *A* and *B*: scatterplots of VF cycle length (VFCL) measured in the RV and LV at all time points of LDVF versus DI (*A*) and APD (*B*). There was a strong direct correlation between VFCL and DI (*A*) and a weak inverse correlation between VFCL and APD (*B*).

Stability of reentry and breakthrough patterns in optical maps. Epi optical maps revealed multiple wavelets/short-living rotors in both chambers until relatively late stages of LDVF (~5–6 min). During this period of time, Epi activation maps were extremely complex and fragmented with only rare occasions of complete reentrant patterns (see Supplemental Fig. 5). At 0 min of LDVF, the maximum duration and number of rotations of reentrant circuits were larger in the RV than in the LV (see Table 1). At 6 min of LDVF, the maximum number of rotations in the RV was not different from that at 0 min LDVF, whereas the maximum lifespan was longer, consistent with prolonged VFCL at this later stage of LDVF. No reentry was observed in the LV at 6 min of LDVF. In 7 of 10 experiments,

Table 1. *Maximal lifespan of repetitive reentrant patterns in epicardial optical maps*

	Maximum Lifespan, ms	Maximum Number of Rotations
Right ventricle		
0 min of LDVF	504 ± 188	4.3 ± 1.2
6 min of LDVF	906 ± 278*	4.7 ± 1.5
Left ventricle		
0 min of LDVF	166.6 ± 3.0*	1.7 ± 0.6*
6 min of LDVF	No reentry	No reentry

Values are means ± SE. LDVF, long-duration ventricular fibrillation. *$P <$ 0.05 vs. the right ventricle at 0 min of LDVF.

repetitive breakthrough patterns were observed in the RV close to the LAD at least in one of the movies recorded after 4 min of LDVF (see Fig. 8*D*). The breakthrough patterns appeared in approximately the same location in at least 50% of activations recorded in the same movie, and transitions from a breakthrough to a reentrant pattern and vice versa in the same location were observed. Repetitive breakthrough patterns were not present in the RV at 0 min of LDVF and were not present in the LV throughout the entire duration of LDVF.

An example of transitions between focal and reentrant pattern in the same location at a late stage of LDVF are shown in Fig. 8, *A–C*. Figure 8*A*,*1* shows a snapshot of a phase movie taken at 8 min of LDVF, which revealed a total of seven coexisting singularity points in the mapped area. The white arrowhead indicates the rotor, which was sustained for about seven rotations and was the dominant source in the area. The rotor was replaced by a breakthrough pattern in the same location (black arrows in Fig. 8*A*,*2*) which lasted for another 9–10 cycles. The breakthrough pattern then reverted back to reentry (white arrow in Fig. 8*A*,*3*). Figure 8*B* shows an activation map computed for the movie taken at 10 min of LDVF. On this map, the colors from red to magenta show a progression of wavefronts emanated by a stable and highly periodic focal source in the RV (black arrows in Fig. 9*B*). The focal source was situated approximately in the same site as the focal/reentrant source observed 2 min earlier and shown in Fig. 8*A*. The waves emitted by the RV source failed to cross the LAD and activate the LV. However, a portion of the LV was activated, at a much slower rate, by a repetitive planar wave (white arrow in Fig. 9*B*), which was apparently unrelated to the fast source in the RV.

Figure 8*C* shows a unique case of stable Epi reentry observed in the same experiment at 16 min of LDVF (and hence beyond the standard duration of LDVF analyzed in this study). The reentrant circuit was located in the basal RV not far from the LAD (counterclockwise arrow in Fig. 8*C*) and was sus-

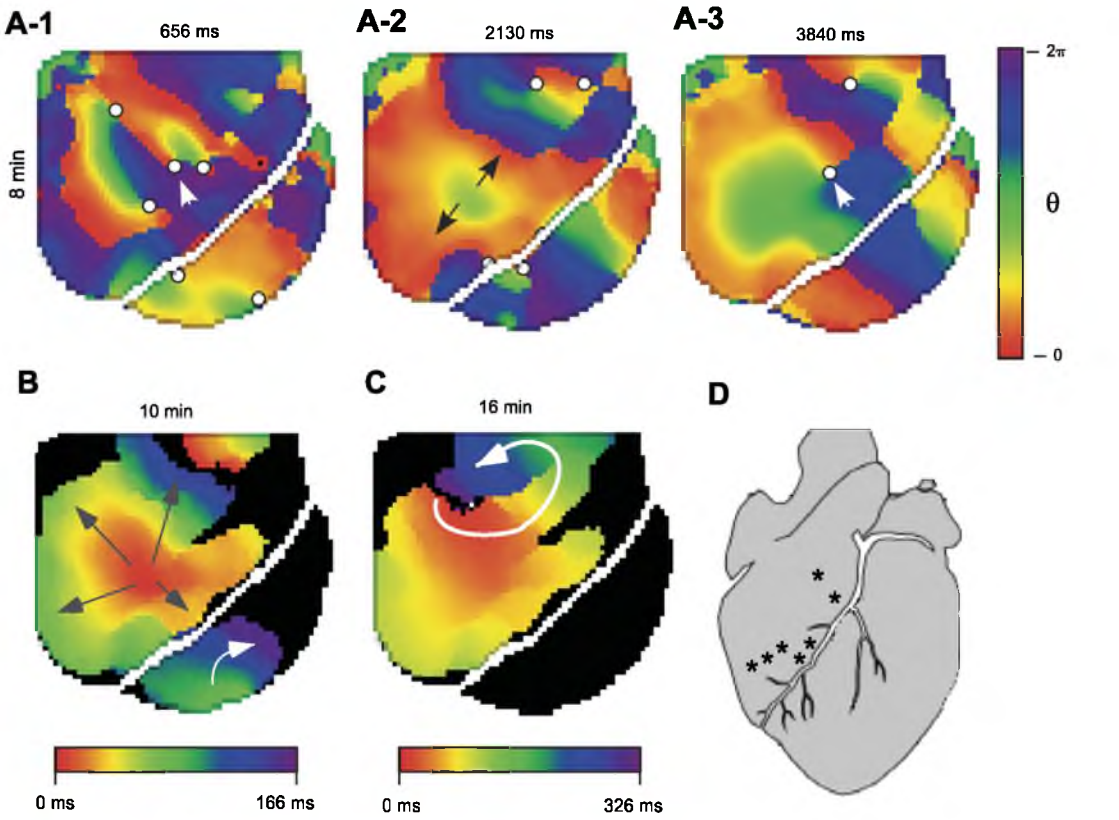

Fig. 8. Examples of transitions between the focal and reentrant pattern in the RV at the late stages of LDVF. *A*: individual frames of a phase movie at 8 min of LDVF. In *1*, several singularity points coexist in the mapped area; the point indicated by the white arrow is the leading source of activation in the mapped area for at least seven cycles. In *2*, the reentrant source is replaced by a repetitive focal source in approximately the same location (black arrows). In *3*, the focal source has reverted back to a repetitive reentrant source (white arrow) in approximately the same location. *B*: activation map at 10 min of LDVF showing a stable focal pattern (black arrows) in the same location as the focal and reentrant sources shown in *A*,*1–3*. This focal source activates the RV but not the LV. The LV is activated by a planar wave (white arrow), which is apparently unrelated to the source in the RV. Red, early activation; magenta, late activation. The red front in the basal RV (*B*, *top*) shows the excitation wave generated in the previous cycle that is exiting the field of view when a new focal wave emerges. *C*: unique example of stable Epi reentry in the RV (white arrow) at a very late stage of LDVF (16 min). *D*: approximate locations of repetitive breakthrough patterns observed in 7 of 10 hearts.

tained throughout the 6-s-long movie. Note that the reentrant waves did not penetrate into the LV, which was completely silent at this late stage of LDVF. Figure 8*D* shows the approximate locations of repetitive breakthrough patterns observed in 7 of 10 hearts.

DISCUSSION

This study provides an extensive analysis of heterogeneous electrical alterations occurring in the canine heart in response to the combined challenges of high excitation rate and ischemia during LDVF. The main finding of this study is the evidence of interchamber and intrachamber heterogeneities of a magnitude comparable to the much more studied gradients between Endo and Epi. In particular, our study revealed the presence of fully inexcitable areas interweaved with still excitable areas in both ventricles during the later stages of LDVF. Additionally, our optical mapping data complement and extend previous work by Kong et al. (19) showing that the right-to-left VFR gradient, similarly to the Endo-to-Epi VFR gradient, is largely determined by the nonuniform distribution of postrepolarization refractoriness amid a relatively invariant APD.

Gradients of the activation rate and sources of fastest activation during VF in globally ischemic hearts. The progressive disparity of VFR between Endo and Epi of both the LV and RV (higher VFR in Endo) during VF in a nonperfused canine heart has been previously shown by several groups (5, 27, 41). It was also documented that RV Epi was faster than LV Epi after 3 min of LDVF and that LV Endo was faster than RV Endo during the first 10 min of LDVF (5). In the rabbit heart, there was an Endo-to-Epi gradient in the LV, but not in the RV, and a right-to-left VFR gradient was present in Epi (42). In contrast to dog and rabbit hearts, in the pig heart, LV Epi was slightly faster than LV Endo and LV Epi was slightly faster than RV Epi at least during the first 3 min of LDVF (see Fig. 3 in Ref. 27). From these results, one can conclude that the overall pattern of VFR distribution during LDVF is complex and species dependent. Yet, the most striking feature is the consistent presence of a large Endo-to-Epi gradient in the LV of both dog and rabbit hearts and the absence thereof (or a slight inverse gradient) in the LV of the pig heart. Based on the principally different arrangement of the Purkinje network (confined to Endo in the dog and rabbit and transmural in the pig), it was postulated that the transmural distribution of VFR during LDVF reflects the dominant role of Purkinje fibers in the maintenance of VF in the ischemic heart. Hence, in dog and rabbit ventricles, the rapid sources of VF are concentrated in Endo, whereas in the pig heart they are distributed throughout the wall thickness. More direct evidence for this hypothesis stemmed from experiments in which Endo ablation with Lugol solution eliminated the transmural VFR gradient (5, 8) or accelerated spontaneous VF termination in isolated LV preparation (8) and from the observation of an increasing incidence of focal patterns in intramural layers of the porcine heart during LDVF (20).

Our quantification of spatial VFR gradients in the canine LV and RV is consistent with a previous report (27) showing the simultaneous presence of both Endo-to-Epi and RV-to-LV gradients of VFR during LDVF. In addition, we found that patterns of activation of the RV and LV during LDVF differ in several respects. First, in the RV, there are no significant differences between Endo and Mid, and, thus, the VFR gradient is mostly present in the outer half of the RV wall. In the LV, however, there is a significant gradient between Endo and Mid as well as between Mid and Epi. Second, RV Epi maintains excitability for a longer time than LV Epi. Third, repetitive reentrant activity is present in the RV but not in the LV at late stages of LDVF. We also found that activation of the Sep (at least at its anterior junction with the RV and LV) deviates from the Purkinje paradigm for LDVF maintenance. In fact, the sites of fastest activation in the Sep were found within 5–6 mm from Epi, which is at least 4 to 5 mm away from the nearest Endo surface containing the Purkinje layer (see Supplemental Fig. 1). Sep Epi locations were consistently faster than surrounding RV Epi and LV Epi locations (see Figs. 3 and 4). Moreover, throughout 10 min of LDVF, the activation rate in Sep Epi and Sep Mid was similar to that in LV Endo (see Supplemental Fig. 3*B*). Thus, based on the fastest VFR criterion, it is possible that Sep Epi and Sep Mid layers may harbor sources maintaining LDVF. This possibility is confirmed by observations of sustained focal and reentrant sources in the vicinity of the RV-Sep junction in Epi optical maps (see Fig. 8). A similar preferential clustering of sustained Epi sources near the Sep has been previously observed during LDVF in the rabbit heart (42). Those authors attributed Sep Epi breakthroughs to a possibility that sub-Endo structures such as papillary muscle insertions located at or near the Sep can anchor and stabilize intramural reentrant sources, which would appear as stable Epi breakthroughs.

This explanation may hold true for the case of the canine heart, where a large papillary muscle is located on the right side of the Sep. However, relatively stable reentrant circuits are also present on Epi of the RV-Sep junction. We think it is possible that the special fiber arrangement with abrupt changes in fiber orientation in the RV-Sep junction may favor the stabilization of reentrant sources in this area, especially when combined with the very slow conduction velocity, short APD, and partial cell-to-cell uncoupling present during ischemia. The ability of the RV-Sep junction to support high-frequency sources during LDVF may also be related to increased mechanical stretch in this area (which is often thinner than the lateral RV wall and Sep) resulting from the sustained RV pressure increase occurring during LDVF (22, 26). Due to the activation of mechanosensitive channels and/or modulation of other ionic channels and transporters, stretch promotes conduction block and reentry and may contribute to the generation of ectopic triggers during ischemia (17, 25). It has also been shown that stretch increases VFR and/or the density of singularity points during normoxemic VF (6, 26) and thus potentially can modulate the organization of VF in ischemic hearts. In conclusion, the unique pattern of activation of the RV-Sep junction during LDVF may be due to a combination of structural and mechanical properties of this region that set it apart from the adjacent RV and LV free walls. However, these assumptions await experimental confirmation.

Mosaic inexcitability during LDVF. A novel finding of this study is the highly heterogeneous pattern of electrical depression in Epi of both the RV and LV during later stages of LDVF (see Fig. 6). Indeed, even though on average VFR was higher in the RV than in the LV, in both chambers there were fully unexcitable regions interweaved with regions maintaining electrical activity. Such areas of local inexcitability were not

observed during LDVF in porcine hearts (16). Clearly, these local Epi gradients cannot be explained in terms of Purkinje fiber distribution and function. The mechanisms responsible for these local gradients remain unknown. One possible mechanism is related to the heterogeneous activation of ATP-sensitive K^+ channel current ($I_{K,ACh}$) secondary to mitochondrial depolarization during ischemia caused by opening of the mitochondrial inner membrane anion channel (IMAC) (1). During global ischemia in the guinea pig heart, an agonist of IMAC, FGIN-127, exacerbated the electrical depression caused by ischemia and induced regional inexcitability at ~10 min of ischemia. It should be noted, however, that the study by Akar et al. (1) did not directly demonstrated the link between regional inexcitability and mitochondrial depolarization. A study (24) using confocal microscopy to image the mitochondrial potential in rat hearts revealed a mosaic presence of cells with depolarized mitochondrial potential among cells with mitochondria still fully polarized. However, the cells exhibiting mitochondrial depolarization appeared only relatively late in ischemia (~20–30 min) and were observed much more frequently upon reperfusion. In addition, they did not form macroscopically continuous regions, which could explain the inexcitable areas observed in our experiments. Thus, the link between mitochondrial depolarization and electrical depression in early ischemia remains unconfirmed. We cannot exclude, however, that the electrical depression dependent on IMAC channel activation is more pronounced under conditions used in our study (LDVF in canine hearts) than in previous studies using small mammalian hearts without VF. It is also possible that the regional inexcitability in Epi of the canine ventricles is promoted by partial cellular uncoupling, which may help to establish a sharp separation between inexcitable and excitable areas. Canine ventricular Epi may be more susceptible to uncoupling during ischemia due to lower expression of connexin43 in Epi compared with deeper layers of the ventricular wall (29). The inexcitable areas observed in this study may hamper the ability of defibrillation shocks applied during advanced stages of LDVF to synchronize the ventricles and may also facilitate the formation of reentrant circuits, which would reinitiate VF after shock application.

Right-to-left gradients in APD and DI during LDVF. To the best of our knowledge, this is the first reported analysis of right-to-left differences in DI and APD during LDVF in the canine heart. In general, VFCL reflects the local effective refractory period (ERP) under the assumption that the tissue is activated as soon as it is capable of conducting an electrical wave. This assumption is reasonable if conduction is not restricted by anatomic barriers and is sustained predominantly by functional reentrant circuits. With the normal availability of fast Na^+ current (I_{Na}), the tissue is able to generate an AP almost immediately upon repolarization from previous excitation, ERP approximates APD well, and, therefore, DIs are short during VF. However, as ischemia develops and causes a decrease in excitability, ERP extends beyond APD (postrepolarization refractoriness). Consequently, DIs during ischemic VF are prolonged (19, 28, 43). Thus, one can assume that in the ischemic heart, the length of DI during VF is a reasonably good indicator of local postrepolarization refractoriness.

Our results clearly show that the right-to-left gradients in VFCL are determined by gradients in DI (and, hence, presumably, by postrepolarization refractoriness) amid a relatively invariant APD over both chambers and all time points of LDVF (see Fig. 8). In fact, there was a slightly longer APD in the RV versus in the LV, which is consistent with observations of a gradient of the same direction observed during pacing in the ischemic rabbit heart (23). In any case, despite the slightly longer APD in the RV than in the LV, VFCL was shorter in the RV than in the LV. Overall, the relationship between VFCL, DI, and APD was very similar to that recently reported by Kong et al. (19). These authors showed that the transmural gradient of VFCL across the LV wall was due to the differences in DI amid a relatively constant APD. Thus, an Endo-to-Epi APD gradient observed in normoxemic canine and human hearts at physiological pacing rates (3, 12) is not present during LDVF and does not influence the VFR gradient in the canine heart. While it is not practically possible to measure ERP in a rigorous manner during the fast and irregular rhythms characteristic of LDVF, our rough estimates of ERP differences between Epi and Endo locations in the LV and RV paced at a relatively fast frequency of 4 Hz during global ischemia are consistent with the presence of ERP gradients both between Endo and Epi and between the RV and LV (see Supplemental Figs. 6–8). Taken together, the arguments above support the notion that both transmural and right-to-left VFR gradients during ischemia in the canine heart are universally determined by the distribution of postrepolarization refractoriness.

LDVF mechanism: sources versus substrate. As mentioned above, the focus of recent relevant studies was on the role of Purkinje fibers as sources of activation maintaining LDVF. The strongest evidence supporting the leading role of Purkinje fibers in the dog heart is the elimination of the transmural gradient after the ablation of Endo with Lugol solution and also earlier spontaneous termination of LDVF in isolated slab preparations (5, 8). As we argued above, the outer layers of the RV-Sep junction may be another source of fast activations apparently unrelated to the fast sources in Endo. Thus, the observation of earlier termination in ablated isolated slabs of the LV free wall (8) may not be applicable to whole hearts with an intact Sep and RV.

It should be noted, however, that the identification of the sources is only one aspect of LDVF. The picture of LDVF will remain incomplete without an understanding of the "substrate," i.e., the response of the ventricles to fast sources of electrical activity. Regardless of whether or not Purkinje fibers are the predominant source of electrical waves, the question remains as to why the electrical depression develops faster in some regions of the ventricle than in others. The large left-to-right and intrachamber VFR gradients shown in this study are most likely unrelated to Purkinje fiber distribution. We argued above that VFR may be regarded as an important index of local electrical depression (and ensuing postrepolarization refractoriness) that appears to be highly nonuniform in the canine heart. During ischemia and VF, a number of ionic currents as well as other factors can contribute to heterogeneous electrical depression. It has been shown that $I_{K,ATP}$ activation can be different between Endo and Epi myocytes (10). We could not find any evidence of differential activation of $I_{K,ATP}$ in the RV versus in the LV during ischemia in the relevant literature. However, the fact that the LV simultaneously has a shorter APD and longer DIs than the RV during LDVF (see Fig. 7) would be consistent with larger $I_{K,ATP}$ in the LV than in the

RV. Indeed, increased time-independent outward K^+ current in the partially depolarized myocardium is expected to accelerate repolarization, on one hand, and to prolong postrepolarization refractoriness, on the other hand. Other K^+ currents whose activation is enhanced under conditions of ischemia and/or a high rate of excitation may also be involved, such as Na^+-activated K^+ current (18). Another possible mechanism of heterogeneous electrical depression during LDVF is the dispersion in the inactivation properties of I_{Na}. Cordeiro at al. (7) have recently shown that Epi cells have a more negative half-inactivation voltage than Endo cells. This property confers a greater sensitivity of ventricular Epi to electrical depression caused by an elevation of extracellular K^+ and thus may contribute to the transmural VFR gradient observed during VF in the globally ischemic heart. Although right-to-left differences in the voltage dependence of I_{Na} inactivation were not reported, in the rabbit heart the right-to-left VFR gradient during LDVF was reproducible by elevating K^+ in the normally oxygenated fibrillating heart (4), indicating chamber-specific differences in the sensitivity to hyperkalemia. We have already mentioned a possible role of mechanical stretch in the maintenance of fast and sustained sources in the RV-Sep area. It is also possible that the distribution of stretch contributes to the transmural gradient of VFR and excitability, since both experimental and computational studies (11, 17, 38) have indicated larger strain in Endo. In particular, right-to-left and/or transmural gradients in mechanical stretch may modulate the spatial distribution of $I_{K,ATP}$ activation, since a reduction in ATP content under ischemic conditions sensitizes ATP-sensitive K^+ channels to stretch (21, 36, 37).

Although the mechanisms discussed above seem to be the most relevant because they are enhanced under conditions presented by LDVF, a number of heterogeneously distributed ionic channels, such as those associated with transient outward K^+ current, the rapid component of delayed rectifier K^+ current, and inward rectifier K^+ current (33), may be involved in nonuniform electrical depression during LDVF.

VF evolution: comparison with previous studies. In his seminal work, Wiggers (40) described four different stages of VF in the open-chested dog: *1*) undulatory or tachysystolic (1–2 s); *2*) convulsive incoordination (15–40 s); *3*) tremulous incoordination (2–3 min); and *4*) progressive atonic incoordination, which usually starts 2–5 min after the onset of VF. This classification was based on the visual analysis of high-speed movies of cardiac contraction. In a more recent study in the same animal model, Huang et al. (15) distinguished five stages (*stages i–v*) during the first 10 min of VF, based on a quantitative analysis of spatiotemporal dynamics of wavefronts extracted from multielectrode Epi maps. They found a nonmonotonic evolution of activation patterns during LDVF, with a transient phase of increased organization and the incidence of reentry between 1 and 3 min after VF onset and a rapid decrease in these parameters in later phases of VF. These authors also observed a steady decrease in the number of wavefronts as LDVF progressed concomitant with a steady increase in the number of breakhtroughs and the incidence of conduction block.

To the extent that it is possible to compare results obtained with different recording and analysis techniques, our present study is consistent with previous observations in several aspects. Similar to Huang et al. (15), we observed a transitory increase in the occurrence of reentry between ~2 and 4 min of LDVF (see Supplemental Fig. 5, *B* and *C*). This approximately corresponds to Wigger's tremulous incoordination phase, during which he noted the presence of "contraction waves. . .circling around in very limited areas" (40). During the next stage (atonic incoordination), Wiggers (40) noted that some areas completely lost contractility, whereas in other areas, especially those close to large vessels and to the right side of the LAD, contractions still persisted. These early observations are fully confirmed by our optical mapping results showing a mosaic distribution of excited and nonexcited areas during this stage of LDVF, with excitability more preserved in areas close to the LAD and in the RV (see Supplemental Fig. 4). Similarly, Huang et al. (15) reported a progressive decrease in the number of wavefronts in LV Epi, which approached zero by 10 min of LDVF. Thus, different studies in dogs agree in their observation of a rapid loss of excitability in LV Epi. It is worth noting, however, that in porcine and rabbit hearts, LV Epi maintains excitability throughout the first 10 min of LDVF (16, 42). This difference may be due to interspecies differences in the ionic channel distribution/function and/or differences in the severity of metabolic stress caused by combined effects of ischemia and LDVF.

Conclusion and significance. Recent studies of LDVF have been focused on the role of Purkinje fibers in LDVF maintenance. Our data indicate that both sources of activity and substrate during LDVF in the canine heart are not exclusively determined by the relationship between Purkinje fibers and the working myocardium. The pattern of activation becomes ever more divergent during the course of LDVF, revealing simultaneous differences between Endo and Epi, RV, LV, and Sep, and within each chamber or wall type. Regardless of whether or not Purkinje fibers maintain self-sustained electrical activity at advanced stages of LDVF, for the purposes of successful defibrillation and resuscitation, it is at least as important whether or not a critical mass of the myocardium can respond in a synchronous manner to an electric shock and any stimulus after defibrillation shock. The presence of large inexcitable areas in the LV and RV may affect the outcome of defibrillation shock and raises the possibility of forming reentrant circuits around inexcitable regions after shock and reinitiation of VF. Thus, future studies concerning LDVF should be more focused on understanding the reasons why the electrical depression develops faster in some regions of the ventricle than in others and how electrical depression heterogeneities interact with the defibrillation shock.

Limitations. In our experiments, LDVF began when perfusion was stopped. In a patient, the termination of perfusion may be more gradual. However, most likely, this difference would affect, at most, the first 1–3 min of LDVF. The main limitation of any mapping technique is incomplete coverage of the three-dimensional pattern of ventricular activation. However, the magnitude of the observed heterogeneities could only increase if we mapped larger regions. The thickness of the ventricular wall is highly nonuniform, whereas the length of the plunge needle electrodes used in both the RV and LV was fixed to accommodate the largest wall thickness in the respective chambers. Thus, in some locations, the most Endo leads were outside the ventricular wall. Despite our best efforts to identify and exclude such leads (see METHODS), an error in this process could have led to an underestimation of the transmural

VFR gradient in the RV and LV. However, the fact that transmural gradients were still detected in both chambers and were consistent with a previous report (5) indicates that this potential problem was of limited influence. Whereas residual motion artifacts could have been present at the early stage of LDVF despite mechanical restraint, the largest interchamber and intrachamber gradients were observed after contractility was completely abolished by the ischemic process. Therefore, the presence of motion artifacts could not have overestimated the magnitude of the gradients. Other common limitations of optical mapping were discussed in our previous publication (16).

ACKNOWLEDGMENTS

The superb technical assistance of Jayne Davis, Alicja Booth, and Nancy Allen is greatly appreciated.

GRANTS

This work was supported by National Heart, Lung, and Blood Institute Grant 5-R01-HL-088444 and by Nora Eccles Treadwell Foundation research grant (to A. V. Zaitsev).

DISCLOSURES

No conflicts of interest, financial or otherwise, are declared by the author(s).

REFERENCES

1. **Akar FG, Aon MA, Tomaselli GF, O'Rourke B.** The mitochondrial origin of postischemic arrhythmias. *J Clin Invest* 115: 3527–3535, 2005.
2. **Allison JS, Qin H, Dosdall DJ, Huang J, Newton JC, Allred JD, Smith WM, Ideker RE.** The transmural activation sequence in porcine and canine left ventricle is markedly different during long-duration ventricular fibrillation. *J Cardiovasc Electrophysiol* 18: 1306–1312, 2007.
3. **Antzelevitch C, Sicouri S, Litovsky SH, Lukas A, Krishnan SC, Di Diego JM, Gintant GA, Liu DW.** Heterogeneity within the ventricular wall. Electrophysiology and pharmacology of epicardial, endocardial, and M cells. *Circ Res* 69: 1427–1449, 1991.
4. **Caldwell J, Burton FL, Smith GL, Cobbe SM.** Heterogeneity of ventricular fibrillation dominant frequency during global ischemia in isolated rabbit hearts. *J Cardiovasc Electrophysiol* 18: 854–861, 2007.
5. **Cha YM, Uchida T, Wolf PL, Peters BB, Fishbein MC, Karagueuzian HS, Chen PS.** Effects of chemical subendocardial ablation on activation rate gradient during ventricular fibrillation. *Am J Physiol Heart Circ Physiol* 269: H1998–H2009, 1995.
6. **Chorro FJ, Trapero I, Guerrero J, Such LM, Canoves J, Mainar L, Ferrero A, Blasco E, Sanchis J, Millet J, Tormos A, Bodi V, Alberola A.** Modification of ventricular fibrillation activation patterns induced by local stretching. *J Cardiovasc Electrophysiol* 16: 1087–1096, 2005.
7. **Cordeiro JM, Mazza M, Goodrow R, Ulahannan N, Antzelevitch C, Di Diego JM.** Functionally distinct sodium channels in ventricular epicardial and endocardial cells contribute to a greater sensitivity of the epicardium to electrical depression. *Am J Physiol Heart Circ Physiol* 295: H154–H162, 2008.
8. **Dosdall DJ, Tabereaux PB, Kim JJ, Walcott GP, Rogers JM, Killingsworth CR, Huang J, Robertson PG, Smith WM, Ideker RE.** Chemical ablation of the Purkinje system causes early termination and activation rate slowing of long-duration ventricular fibrillation in dogs. *Am J Physiol Heart Circ Physiol* 295: H883–H889, 2008.
9. **Evans FG, Rogers JM, Smith WM, Ideker RE.** Automatic detection of conduction block based on time-frequency analysis of unipolar electrograms. *IEEE Trans Biomed Eng* 46: 1090–1097, 1999.
10. **Furukawa T, Kimura S, Furukawa N, Bassett AL, Myerburg RJ.** Role of cardiac ATP-regulated potassium channels in differential responses of endocardial and epicardial cells to ischemia. *Circ Res* 68: 1693–1702, 1991.
11. **Gallagher KP, Osakada G, Matsuzaki M, Miller M, Kemper WS, Ross J Jr.** Nonuniformity of inner and outer systolic wall thickening in conscious dogs. *Am J Physiol Heart Circ Physiol* 249: H241–H248, 1985.
12. **Glukhov AV, Fedorov VV, Lou Q, Ravikumar VK, Kalish PW, Schuessler RB, Moazami N, Efimov IR.** Transmural dispersion of repolarization in failing and nonfailing human ventricle. *Circ Res* 106: 981–991, 2010.
13. **Gray RA, Pertsov AM, Jalife J.** Spatial and temporal organization during cardiac fibrillation. *Nature* 392: 75–78, 1998.
14. **Hong MF, Dorian P.** Update on advanced life support and resuscitation techniques. *Arrhythmias Curr Opin Cardiol* 20: 1–6, 2005.
15. **Huang J, Rogers JM, Killingsworth CR, Singh KP, Smith WM, Ideker RE.** Evolution of activation patterns during long-duration ventricular fibrillation in dogs. *Am J Physiol Heart Circ Physiol* 286: H1193–H1200, 2004.
16. **Huizar JF, Warren MD, Shvedko AG, Kalifa J, Moreno J, Mironov SF, Jalife J, Zaitsev AV.** Three distinct phases of VF during global ischemia in the isolated blood-perfused pig heart. *Am J Physiol Heart Circ Physiol* 293: H1617–H1628, 2007.
17. **Jie X, Gurev V, Trayanova N.** Mechanisms of mechanically induced spontaneous arrhythmias in acute regional ischemia. *Circ Res* 106: 185–192, 2010.
18. **Kameyama M, Kakei M, Sato R, Shibasaki T, Matsuda H, Irisawa H.** Intracellular Na^+ activates a K^+ channel in mammalian cardiac cells. *Nature* 309: 354–356, 1984.
19. **Kong W, Ideker RE, Fast VG.** Transmural optical measurements of V_m dynamics during long-duration ventricular fibrillation in canine hearts. *Heart Rhythm* 6: 796–802, 2009.
20. **Li L, Jin Q, Huang J, Cheng KA, Ideker RE.** Intramural foci during long duration fibrillation in the pig ventricle. *Circ Res* 102:1256–1264. 2008.
21. **Li W, Kohl P, Trayanova N.** Myocardial ischemia lowers precordial thump efficacy: an inquiry into mechanisms using three-dimensional simulations. *Heart Rhythm* 3: 179–186, 2006.
22. **Mashiro I, Cohn JN, Heckel R, Nelson RR, Franciosa JA.** Left and right ventricular dimensions during ventricular fibrillation in the dog. *Am J Physiol Heart Circ Physiol* 235: H231–H236, 1978.
23. **Pandit SV, Shibayama J, Mironov S, Anumonwo J, Vikstrom K, Jalife J.** Electrophysiological changes in left versus right ventricle during global ischemia and reperfusion: role of sarcolemmal K-ATP channels (Abstract). *Heart Rhythm* 5: S112, 2008.
24. **Matsumoto-Ida M, Akao M, Takeda T, Kato M, Kita T.** Real-time 2-photon imaging of mitochondrial function in perfused rat hearts subjected to ischemia/reperfusion. *Circulation* 114: 1497–1503, 2006.
25. **McNary TG, Sohn K, Taccardi B, Sachse FB.** Experimental and computational studies of strain-conduction velocity relationships in cardiac tissue. *Prog Biophys Mol Biol* 97: 383–400, 2006.
26. **Moreno J, Zaitsev AV, Warren M, Berenfeld O, Kalifa J, Lucca E, Mironov SF, Guha PK, Jalife J.** Effect of remodelling, stretch and ischaemia on ventricular fibrillation frequency and dynamics in a heart failure model. *Cardiovasc Res* 65: 158–166, 2005.
27. **Newton JC, Smith WM, Ideker RE.** Estimated global transmural distribution of activation rate and conduction block during porcine and canine ventricular fibrillation. *Circ Res* 94: 836–842, 2004.
28. **Robertson PG, Huang J, Chen KA, Chen X, Dosdall DJ, Tabereaux PB, Smith WM, Ideker RE.** Increased cycle length during long-duration ventricular fibrillation is caused by decreased upstroke velocity as well as prolonged refractoriness. *Heart Rhythm* 6: 378–384, 2009.
29. **Poelzing S, Akar FG, Baron E, Rosenbaum DS.** Heterogeneous connexin43 expression produces electrophysiological heterogeneities across ventricular wall. *Am J Physiol Heart Circ Physiol* 286: H2001–H2009, 2004.
30. **Rogers JM, Melnick SB, Huang J.** Fiberglass needle electrodes for transmural cardiac mapping. *IEEE Transact Biomed Eng* 49: 1639–1641. 2002.
31. **Roth R, Stewart R, Rogers K.** Out-of-hospital cardiac arrest: factors associated with survival. *Ann Emerg Med* 13: 237–243, 1984.
32. **Samie FH, Berenfeld O, Anumonvo J, Mironov SF, Udassi S, Beaumont J, Taffet S, Pertsov AM, Jalife J.** Rectification of the background potassium current. A determinant of rotor dynamics in ventricular fibrillation. *Circ Res* 89: 1216–1223, 2001.
33. **Schram G, Pourrier M, Melnyk P, Nattel S.** Differential distribution of cardiac ion channel expression as a basis for regional specialization in electrical function. *Circ Res* 90: 939–950, 2002.
34. **Tabereaux PB, Walcott GP, Rogers JM, Kim J, Dosdall DJ, Robertson PG, Killingsworth CR, Smith WM, Ideker RE.** Activation patterns of purkinje fibers during long-duration ventricular fibrillation in an isolated canine heart model. *Circulation* 116: 1113–1119, 2007.

35. **Taccardi B, Punske BB, Macchi E, MacLeod RS, Ershler PR.** Epicardial and intramural excitation during ventricular pacing: effect of myocardial structure. *Am J Physiol Heart Circ Physiol* 294: H1753–H1766, 2008.
36. **Van Wagoner DR.** Mechanosensitive gating of atrial ATP-sensitive potassium channels. *Circ Res* 72: 973–983, 1993.
37. **Van Wagoner DR, Lamorgese M.** Ischemia potentiates the mechanosensitive modulation of atrial ATP-sensitive potassium channels. *Ann NY Acad Sci* 723: 392–395, 1994.
38. **Vetter F, McCulloch A.** Mechanoelectric feedback in a model of the passively inflated left ventricle. *Ann Biomed Eng* 29: 414–426, 2001.
39. **Warren M, Guha PK, Berenfeld O, Zaitsev A, Anumonwo JMB, Dhamoon AS, Bagwe S, Taffet SM, Jalife J.** Blockade of the inward rectifying potassium current terminates ventricular fibrillation in the guinea pig heart. *J Cardiovasc Electrophysiol* 14: 621–631, 2003.
40. **Wiggers CJ, Bell JR, Paine M.** Studies of ventricular fibrillation caused by electric shock. II. Cinematographic and electrocardiographic observations of the natural process in the dog's heart: its inhibition by potassium and the revival of coordinated beats by calcium. *Am Heart J* 5: 351–365, 1930.
41. **Worley SJ, Swain JL, Colavita PG, Smith WM, Ideker RE.** Development of an endocardial-epicardial gradient of activation rate during electrically induced, sustained ventricular fibrillation in dogs. *Am J Cardiol* 55: 813–820, 1985.
42. **Wu TJ, Lin SF, Hsieh YC, Ting CT, Chen PS.** Ventricular fibrillation during no-flow global ischemia in isolated rabbit hearts. *J Cardiovasc Electrophysiol* 17: 1112–1120, 2006.
43. **Zaitsev AV, Guha PK, Sarmast F, Kolli A, Berenfeld O, Pertsov AM, de Groot JR, Coronel R, Jalife J.** Wavebreak formation during ventricular fibrillation in the isolated, regionally ischemic pig heart. *Circ Res* 92: 546–553, 2003.

CHAPTER 5

ROLE OF K_{ATP} CHANNEL IN ELECTRICAL DEPRESSION AND ASYSTOLE DURING LONG-DURATION VENTRICULAR FIBRILLATION IN EX VIVO CANINE

The research in this chapter was published in the *American Journal of Physiology: Heart and Circulatory Physiology.* Tyson G. Taylor, Paul W. Venable, Junko Shibayama, Mark Warren, and Alexey V. Zaitsev.: 'Role of K_{ATP} channel in electrical depression and asystole during long-duration ventricular fibrillation in ex vivo cainine heart.' Am J Physio Heart Circ Physiol, 2013, 302, pp. H2396-H2409. Reprinted with permission of the American Physiology Society.

Am J Physiol Heart Circ Physiol 302: H2396–H2409, 2012.
First published March 31, 2012; doi:10.1152/ajpheart.00752.2011.

Role of K_{ATP} channel in electrical depression and asystole during long-duration ventricular fibrillation in ex vivo canine heart

Tyson G. Taylor,* Paul W. Venable,* Junko Shibayama, Mark Warren, and Alexey V. Zaitsev
Nora Eccles Harrison Cardiovascular Research and Training Institute, University of Utah, Salt Lake City, Utah

Submitted 29 July 2011; accepted in final form 22 March 2012

Taylor TG, Venable PW, Shibayama J, Warren M, Zaitsev AV. Role of K_{ATP} channel in electrical depression and asystole during long-duration ventricular fibrillation in ex vivo canine heart. *Am J Physiol Heart Circ Physiol* 302: H2396–H2409, 2012. First published March 31, 2012; doi:10.1152/ajpheart.00752.2011.—Long-duration ventricular fibrillation (LDVF) in the globally ischemic heart is characterized by transmurally heterogeneous decline in ventricular fibrillation rate (VFR), emergence of inexcitable regions, and eventual global asystole. Rapid loss of both local and global excitability is detrimental to successful defibrillation and resuscitation during cardiac arrest. We sought to assess the role of the ATP-sensitive potassium current (I_{KATP}) in the timing and spatial pattern of electrical depression during LDVF in a structurally normal canine heart. We analyzed endo-, mid-, and epicardial unipolar electrograms and epicardial optical recordings in the left ventricle of isolated canine hearts during 10 min of LDVF in the absence (control) and presence of an I_{KATP} blocker glybenclamide (60 μM). In all myocardial layers, average VFR was the same or higher in glybenclamide-treated than in control hearts. The difference increased with time of LDVF and was overall significant in all layers ($P < 0.05$). However, glybenclamide did not significantly affect the transmural VFR gradient. In epicardial optical recordings, glybenclamide shortened diastolic intervals, prolonged action potential duration, and decreased the percentage of inexcitable area (all differences $P < 0.001$). During 10 min of LDVF, asystole occurred in 55.6% of control and none of glybenclamide-treated hearts ($P < 0.05$). In three hearts paced after the onset of asystole, there was no response to LV epicardial or atrial pacing. In structurally normal canine hearts, I_{KATP} opening during LDVF is a major factor in the onset of local and global inexcitability, whereas it has a limited role in overall deceleration of VFR and the transmural VFR gradient.

adenosine 5′-triphosphate-sensitive potassium channel; glybenclamide; myocardial ischemia; optical mapping

VENTRICULAR FIBRILLATION (VF) is a major cause of sudden cardiac death and a common context of cardiopulmonary resuscitation. In the setting of out-of-hospital cardiac arrest, VF intervention is often delayed for at least several minutes until first responders arrive at the scene, detect cardiac rhythm, and initiate life-saving procedures. Such relatively long-duration VF (LDVF) is characterized by a nonuniform depression of electrical activity, manifested as a transmural gradient in VF rate (VFR) in canine (2, 6, 14, 30, 43, 56, 62, 67) and human (37) hearts. An extreme form of heterogeneous electrical depression was observed in epicardial optical maps, where sharply demarcated inexcitable areas emerged within the fibrillating myocardium (62). Heterogeneous loss of excitability may promote initiation of VF upon reperfusion of a globally ischemic heart (1).

Untreated, LDVF eventually degenerates into asystole, a complete cessation of electrical activity in the heart. In the context of out-of-hospital cardiac arrest, asystole is a "non-shockable" rhythm associated with a very poor prognosis of survival to hospital discharge (22, 25, 44). In recent years, the reported incidence of asystole as the first recorded rhythm during sudden cardiac arrest (SCA) has increased compared with the incidence of VF (8, 48). This may indicate a trend towards faster degeneration of VF into asystole in the clinical setting. Considering that the window of opportunity for successful resuscitation is limited to ~10 min after the onset of SCA (52), the rapidity at which electrical depression develops during the course of LDVF may have a significant impact on survival in this setting.

The factors determining the timing of local and global electrical standstill in the course of LDVF remain largely unknown. One of the most prominent mechanisms linking metabolic stress and electrical activity during ischemia is the ATP-sensitive potassium current (I_{KATP}; Ref. 17). I_{KATP} is principally regulated by the blocking effect of ATP and activating effect of MgADP but is also modulated by a plethora of signaling pathways (17). The complexity of I_{KATP} regulation at least partially explains the difficulty to pinpoint the actual events and conditions that trigger opening of the channel during ischemia. A possible role of I_{KATP} in the maintenance of LDVF was recently highlighted by Farid et al. (15). These authors found that blockade of I_{KATP} in hearts explanted from patients with end-stage heart failure resulted in an increased incidence of spontaneous VF termination, an overall decrease in VFR, and a diminished transmural difference in VFR compared with control conditions. The authors attributed these effects of glybenclamide to the prevention of the action potential duration (APD) shortening presumably caused by I_{KATP} activation in this model of LDVF (15). Furthermore, these authors suggested that I_{KATP} blockade could be a rational strategy to improve outcomes of SCA caused by VF. The importance of their results notwithstanding, the study by Farid at al. has left several important questions unanswered. First, their study was performed in hearts explanted from patients with end-stage heart failure, which is an extreme and terminal condition even within the population afflicted with this disease. Moreover, in these patients VF is not a predominant rhythm causing SCA (35); thus LDVF in these hearts may not be representative of the cases of SCA due to VF, which are often a consequence of acute triggering events occurring in hearts without advanced structural abnormalities (7). Second, they studied the effect of I_{KATP} blockade only during the first 3 min of LDVF, a time window that is much shorter than the typical interval between collapse and initiation of life-saving proce-

* T. G. Taylor and P. W. Venable contributed equally to this study.

Address for reprint requests and other correspondence: A. V. Zaitsev, Cardiovascular research and Training Institute,Univ. of Utah, 95 South 2000 East, Salt Lake City, UT 84112-5000 (e-mail: zaitsev@cvrti.utah.edu).

dures (54). The outcomes could be different at later stages of LDVF, which may be more relevant to out-of-hospital SCA. Third, the rhythm following VF termination was not reported. Clearly, if VF termination was followed by global inexcitability, such an outcome of I_{KATP} blockade could hardly be considered beneficial. Lastly, APD prolongation by glybenclamide may not necessarily prolong the VF cycle length (VFCL). During LDVF, the excitation cycle lengths poorly correlates with APD and is largely determined by the length of diastolic intervals (DIs), which get progressively longer in the course of LDVF (30, 49, 62).

While ideally these questions would be addressed using hearts from human donors representing the general population, in practice this goal is hard to attain. Apart from the rarity of this research opportunity, it is almost impossible to control the history of ischemic or hypoxic exposure of human hearts rejected for the purposes of transplantation and made available for research. However, such exposure(s) may cause preconditioning effects that may not affect results obtained under normoxemic conditions but that may alter the outcomes of the tested LDVF (58). With the above considerations in mind we were motivated to perform a study aimed to ascertain the role of I_{KATP} in the dynamics and outcomes of LDVF occurring in a structurally normal canine heart, which is close to human heart in terms of size, ionic channel make-up and Purkinje fiber distribution. In our study, we assessed the effects of I_{KATP} blockade by glybenclamide on the transmural VFR gradient, APD derived from epicardial optical recordings, and the timing of the onset of local and global inexcitability in the course of LDVF. Contrary to the observations in explanted failed human hearts (15), we found that K_{ATP} channel blockade did not significantly alter the transmural VFR gradient but delayed VF termination and maintained on average a slightly higher VF rate compared with control despite a slight increase in optical APD. Additional experiments were performed to exclude the role of side effects of glybenclamide with respect to other potassium currents such as the rapid component of the delayed rectifier current (I_{Kr}) and the transient outward current (I_{to}). We conclude that in structurally normal hearts K_{ATP} channels are a major factor in the transition from a state of depressed excitability to complete electrical standstill, but they have a limited role in the transmural VFR gradient during LDVF. These results underscore the important differences in the effects of I_{KATP} blockade in normal vs. severely failing hearts. Possible reasons for these differences are discussed.

MATERIALS AND METHODS

This investigation conformed to the *Guide for the Care and Use of Laboratory Animals* published by the National Institutes of Health (NIH publication No. 85-23, revised 1996). The animal protocols were approved by the University of Utah Institutional Animal Care and Use Committee (Protocol No. 10-09005).

Study groups. A total of 28 dogs, 14 random source dogs (27.0 ± 1.3 kg, 9 males, 5 females) and 14 purpose-bred dogs (21.6 ± 0.8 kg, 7 males, 7 females) were used in this study. The source of dogs changed in the course of the study due to recently enacted institutional mandates. Nine hearts served as the control group. Six hearts were treated with an I_{KATP} blocker glybenclamide (GLYB; 60 μM). To exclude the possibility that the observed effects of glybenclamide were confounded by partial blockade of I_{Kr} (51), an additional six hearts were treated with a selective blocker of I_{Kr} dofetilide (DOF; 1 μM). To exclude the possibility that the observed effects of glybenclamide were confounded by partial blockade of the transient outward potassium current I_{to} (53) (26), a group of six hearts was treated with a combination of a K_{ATP} channel opener chromakalim (10 μM) and I_{to} blocker 4-aminopyridine (1 mM; CRO + 4AP). Assuming that glybenclamide at a concentration of 60 μM induces a significant degree of I_{to} blockade, our comparison between CRO + 4AP and GLYB groups allowed us to contrast the effects of I_{KATP} activation and blockade under relatively uniform conditions of I_{to} inhibition. One additional heart was treated with cromakalim only and was used for assessment of the effect of this drug on VFR under conditions of normal perfusion and oxygenation.

Experimental protocol. The dogs were premedicated with acepromazine (0.1 ml/10 kg), Telazol (0.1 ml/kg), or propofol (7.45 mg/kg) and maintained with sodium pentobarbital (32.5 mg/kg). Intubation was accomplished with a cuffed endotracheal tube, and mechanical ventilation was maintained at 10–15 cycles/min (tidal volume: 15–20 cc/kg). Following isolation via midline sternotomy, the hearts were perfused in a Langendorff apparatus with a mixture of blood and Tyrode solution as described in detail in our previous publications (27, 68). Briefly, the blood-Tyrode mixture was oxygenated (CO_2 5%-O_2 95%), heated (37°C), and filtered using standard pediatric heart perfusion units from various vendors. Perfusate was collected for recirculation with collector tubes inserted into the right and the left ventricles via cuts in the appendages of the respective atria. The heart was then placed in a temperature-controlled bath with heated water-jacketed transparent glass walls. The bath was filled with warmed Tyrode solution, which was continuously pumped, without recirculation, at a rate of 80–150 ml/min. The oxygen content in the superfusate was removed by continuous gassing with a 95% N_2/5% CO_2 mixture. The temperatures in the right ventricular cavity, superfusate, and water jacket were maintained at 37 ± 0.5°C during both normal coronary perfusion and ischemia. The gradient of temperature across the left ventricular wall did not exceed 1°C. In all hearts, immediately preceding the induction of ischemia, the perfusion was switched to Tyrode solution with the dual purpose of ensuring constant composition of the extracellular milieu at the onset of LDVF and enhancing the voltage-sensitive signal for the purpose of improving resolution of low-amplitude signals at advanced stages of LDVF. VF was induced using a 9V DC battery 10 s to 5 min before the onset of global ischemia initiated by interruption of aortic perfusion. No perceptible differences in the measured parameters were found between experiments with respect to the duration of VF before the onset of ischemia; therefore, in all experiments the time of LDVF was counted from the moment when perfusion was stopped.

In the GLYB group, glybenclamide (60 μM) was added to the recirculating blood-Tyrode mixture 20–30 min before the onset of LDVF and its successful delivery to the heart was verified by observing an increase in the aortic pressure caused by the vasoconstricting effect of glybenclamide (12). In this study, the aortic pressure increased by 35 ± 5% after administration of glybenclamide. In the DOF group, dofetilide (1 μM) was added to the circulating solution 10 min prior to the onset of LDVF in six hearts. In the CRO + 4AP group, cromakalim (10 μM) and 4-aminopyridine (1 mM) were added to the recirculating mixture in alternating order 20 and 10 min before the onset of LDVF; in three hearts cromakalim was added first while in three more hearts 4-aminopyridine was added first. Thus, in a total of six hearts constituting the CRO + 4AP group, both cromakalim and 4-aminopyridine were present in the perfusate for ≥10 min before the onset of LDVF. In DOF and CRO + 4AP groups, brief (1-min) episodes of VF were induced before and 10 min after administration of each drug and VFR was measured during the last 4 s of 1-min VF episodes. In this way, the individual effects of all drugs on VFR in normally perfused hearts could be assessed. After that, VF was promptly terminated by a defibrillation shock with the remaining experimental protocol being the same as in control and GLYB groups.

In all experiments only data from the first 10 min of LDVF were compared. If asystole occurred with abrupt and continued silence (>60 s) during LDVF the right atrium, LV epicardium and LV

endocardium were paced at 3 and 10 times end-diastolic preischemic threshold to determine excitability.

High-resolution epicardial optical mapping. Details of optical mapping are given in our previous publication (62). Briefly, we used a high-resolution electron-multiplied CCD camera (iXon DU-860D; Andor Technology, Belfast, UK) to image fluorescence of the voltage-sensitive dye Di-4-ANEPPS (Molecular Probes, Carlsbad, CA). The field of view covered the epicardial surface of the anterior LV including a portion of the left anterior descending coronary artery (Fig. 1). The size of the field of view varied between 40 × 40 mm and 65 × 65 mm. To minimize motion artifacts, the heart was gently pressed against the glass chamber wall as previously described (27, 68). No electromechanical uncouplers were used. Five second-long movies were acquired every 30 s from 0 to 10 min of LDVF. To minimize phototoxicity, exposure to the excitation light was limited to 7 s per movie by means of an electronic shutter synchronized with the video camera.

Analysis of optical signals. Spatial distributions of VFR, APD, and DI at different time points during LDVF were estimated in optical mapping data using custom routines developed in PV-Wave software (Visual Numerics, Boulder, CO). Dominant frequency of the Fourier spectrum was not used to estimate VFR because it did not reliably represent the perceived number of activations per unit of time at advanced stages of LDVF when the action potential is characterized by very short APD and long DI. Instead, we used an algorithm to detect individual action potentials in single pixel recordings similar to that described in our previous publications (27, 62). In brief, the depolarization and repolarization phases of each optical action potential (OAP) were detected. The time points at which the depolarization and repolarization phases crossed a line drawn at 40% level of the absolute maximum in the respective signal (ΔF_{max}) were determined. From these time points, APD, DI, and VFCL were calculated for each cycle. The algorithm rejected noise based on thresholds set for APD (<10 ms), VF cycle length (<30 ms), absolute O AP amplitude (<15 levels of brightness), and percent O AP amplitude with respect to the time sequence maximum (<5% of ΔF_{max}). VFR maps were created by dividing the number of OAPs by the duration of the analyzed movie. Areas with no OAPs detected throughout the entire movie were considered to be inexcitable and having a VFR = 0. The lack of activation in continuous areas having VFR = 0 was confirmed by visual inspection of movies. Such areas were counted for the purposes of determining the average VFR and percentage of inexcitable area but were excluded from the calculation of average APD and DI.

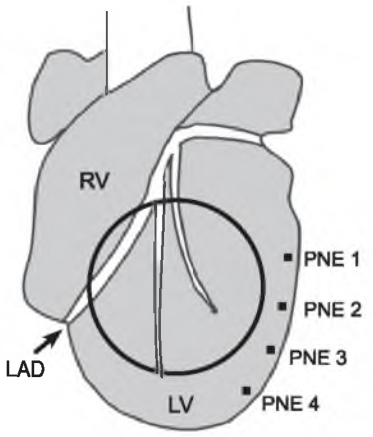

Fig. 1. Schematic representation of mapping modalities used in this study. Circle denotes the area imaged with the optical mapping system, including predominantly anterior left ventricular (LV) and a narrow region of right ventrice (RV; the latter was excluded from analysis). Black squares denote approximate positions of plunge needle electrodes (PNE 1-PNE 4). Electrodes were placed in the lateral LV close to the margin of the imaged area. LAD, left anterior descending coronary artery.

Electrical recordings. Volume-conducted ECG were recorded from two electrodes attached to the walls of the superfusion chamber with ground electrode attached to the bottom. Plunge needle electrodes with 10 evenly spaced unipolar leads (inter-lead, distance, 1.6 mm) were manufactured in-house following the design developed by Rogers et al. (50). The needles were placed in the lateral LV free wall adjacent to the optically mapped area as shown schematically in Fig. 1. The distance between needles was 10–15 mm. Unipolar electrograms from all contacts of the needle electrodes and volume-conductor ECG were recorded continuously during the first 10 min of LDVF at a sampling rate of 1 kHz using a custom-made multichannel data acquisition system as described previously (57). VF termination was defined as the first time point at which the ECG no longer showed VF/VT for 20 consecutive seconds. Asystole was defined as spontaneous VF termination and complete electrical silence (ECG signal indistinguishable from noise with amplitude <10% of ECG amplitude measured at 0 min of LDVF) lasting for ≥20 s.

Electrode data analysis. Unipolar electrograms were analyzed using custom software developed in the Matlab (MathWorks, Natick, MA) framework. The electrograms were first filtered using a 60-Hz notch filter. We applied the Hilbert Transform to unipolar electrograms as previously described (36, 41). Hilbert transform converts fluctuating voltage signal into its corresponding phase so that consecutive cycles of activation are represented by changes in phase from 0 to 2π. Thus the number of phase transitions from 2π to 0 per unit of time gives an estimate of frequency. To decrease the influence of noise, the activation cycles with length <33 ms and amplitude of the waveform between two consecutive phase transitions <10% of the electrogram amplitude measured at 0 min of LDVF were excluded from the total cycle counts. After that, VFR was calculated as the average number of activations per second over 4-s intervals taken at 4 s after LDVF induction and at min 1 to 10 of LDVF. For simplicity, the first time point will be referred to as 0 min LDVF.

Whereas the length of the plunge needle electrodes was constant and designed to span the largest thickness observed in LV of the canine heart, the actual thickness of the ventricular wall is highly nonuniform. Thus in some cases plunge needle electrodes were longer than the wall thickness at the site of insertion. The contacts protruding from the ventricular wall were excluded from analysis based on the following criteria (62): *1*) leads with signal-to-noise ratio <200%; *2*) low VFR at 0 min of LDVF (slower by 5 Hz or more compared with the average VFR measured in all locations); *3*) decrease of VFR to below 2 Hz within the first min of LDVF; and *4*) observation of a progressively decreasing electrogram amplitude towards more distal leads while maintaining the same morphology as more proximal leads in the same needle. In the latter case, the most proximal lead from the group of leads with identical morphology was designated as the endocardial (ENDO) location in the needle. The position of the epicardial (EPI) lead could be easily ensured by visual inspection. In some experiments, the LV cavity was opened after the experiment and the positions of the ENDO leads in plunge needles were verified by visual inspection of the endocardium. After determination of the most distal lead in contact with the myocardial wall (ENDO), the mid-myocardial lead (MID) was chosen as the one closest to being equidistant between EPI and ENDO.

Statistical analysis. In the data collected from the plunge needle electrodes, the time course of VFR was statistically compared in a 2 × 3 matrix with dimensions of experimental group (control and GLYB) and location (EPI, MID, and ENDO) using a two-way ANOVA with post hoc multiple comparisons and Bonferroni correction. In each experiment, the data from EPI, MID, and ENDO locations were represented by average values from all four plunge needle electrodes inserted in the LV lateral wall (see Fig. 1). Note that

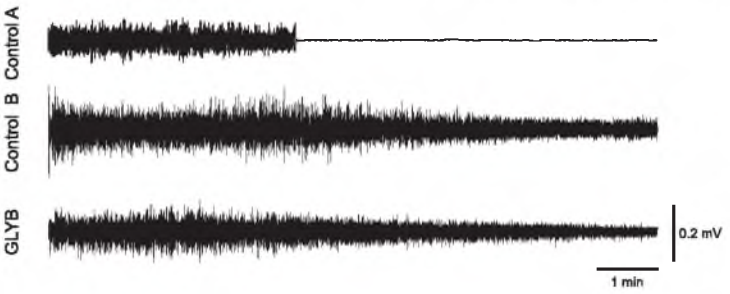

Fig. 2. Examples of volume-conducted ECGs obtained from a control heart with early asystole (*control A*), control heart with no asystole within 10 min of long-duration ventricular fibrillation (LDVF; *control B*) and a heart treated with glybenclamide (GLYB).

the statistical significance indicated the differences between the means at all time points of LDVF in different locations. No conclusions regarding differences at individual time points were made due to a prohibitively large number of required pairwise comparisons. In the data collected from optical recordings, average values of VFR, APD, DI, and percentage of inexcitable area were calculated for each time point during LDVF. A two-way ANOVA was performed with post hoc multiple comparisons and Bonferroni correction to compare the time courses of these parameters between control and GLYB groups. Similar to statistical treatment of the electrode data, the statistical significance indicated the differences between the mean values of measured parameters at all time points of LDVF. Timing of asystole was compared between control and GLYB hearts using a log-rank test applied to Kaplan-Meier survival curves. Comparisons of VFR between multiple groups at baseline and 10 min of LDVF were made using *t*-tests with Bonferroni correction for multiple pairwise comparisons. Data are given in mean ± SE. A difference at $P < 0.05$ was considered statistically significant.

RESULTS

Effect of glybenclamide on the timing of global asystole. Figure 2 shows examples of volume-conducted ECG in two control hearts (*control A* and *control B*) and one GLYB heart. In the *control A* heart, the ECG shows abrupt termination of VF followed by the lack of any electrical activity. In *control B* and GLYB hearts, LDVF persists for the entire 10-min interval. In all cases, the event of asystole detected in volume-conductor ECG coincided with the lack of activity in all optical and electrical recordings.

Figure 3 shows the cumulative probability of asystole in the absence and the presence of glybenclamide (60 μM). It can be seen that in the absence of the drug the likelihood of asystole cumulatively increased between 4 and 10 min of LDVF reaching 55.6% (5 out of 9 hearts) by the end of the tested interval. In four out of five asystolic hearts, VF terminated abruptly. In one heart, VF was followed by ~30 s of ventricular tachycardia at a cycle length of ~360 ms followed by asystole. In contrast, in the presence of 60 μM glybenclamide asystole did not occur in six out of six hearts within the first 10 min of LDVF. The difference in the timing of asystole between control and glybenclamide-treated hearts was statistically significant ($P < 0.05$) by log-rank test.

In three control hearts that experienced complete asystole we applied pacing in LV EPI, LV ENDO and right atrium following VF termination. The stimulus strength was set at 3 times and 10 times preischemic end-diastolic excitation threshold. In two of three hearts, none of the locations elicited a response, while in one heart only LV ENDO responded, and only to the largest stimulus (10 times preischemic threshold). Thus asystole in these hearts was associated with profound depression of excitability.

Effect of glybenclamide on the transmural VFR distribution. Examples of transmural unipolar electrograms can be found in Fig. 4. Statistical analysis of transmural VFR distribution in the presence and the absence of glybenclamide is presented in Fig. 5. Figure 5, *A* and *B*, shows VFR values vs. time of no perfusion in different layers of LV wall (ENDO, MID, and EPI) in control and GLYB hearts, respectively. It is clear that an ENDO-to-EPI gradient in VFR was consistently present both in the absence and in the presence of glybenclamide. In both groups, most of the transmural VFR difference was concentrated between EPI and MID. Accordingly, both ENDO and MID were statistically different from EPI, but there was no statistical difference between ENDO and MID in both groups.

Figure 5*C* shows the time course of the transmural VFR gradient (estimated as the difference between ENDO and EPI) in the two groups derived from the same data as shown in Fig. 5, *A* and *B*. In the control group, the transmural VFR gradient reached peak at 7 min of LDVF and decreased again by 10 min of LDVF, when VFR in all layers converged to very low values (see Fig. 5*A*). Interestingly, the dynamics of VFR gradient in GLYB group was somewhat reciprocal to that in the control group, such that the maximal gradient was reached at 3 min, decreased between 3 and 8 min, and then increased again at 10 min of LDVF. In any case, the overall dynamics of the VFR gradient was not statistically different between GLYB and control groups.

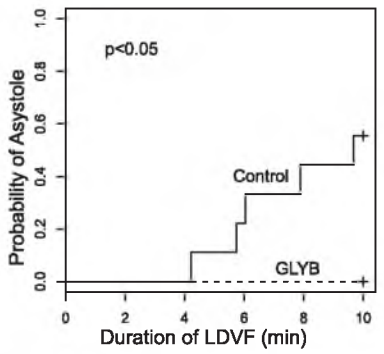

Fig. 3. Cumulative probability of asystole during 10 min of LDVF in the absence (solid line) and the presence (dashed line) of glybenclamide (60 μM). In control ~50% of hearts experienced asystole, whereas in the presence of glybenclamide asystole did not occur (significantly different at $P < 0.05$).

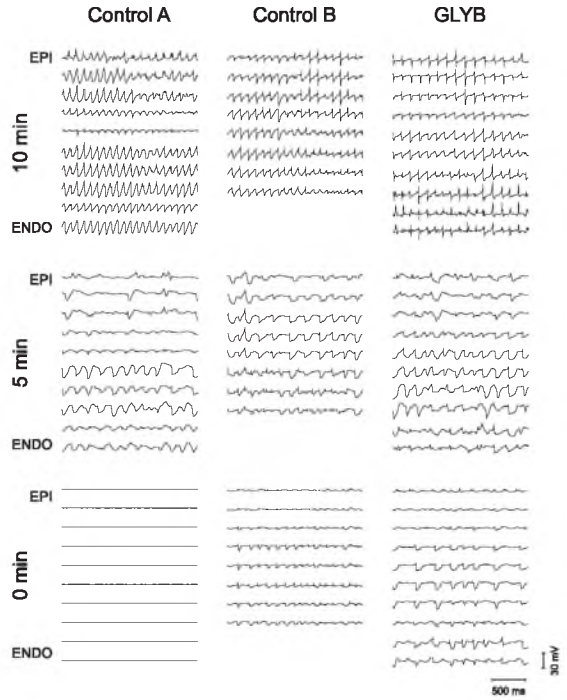

Fig. 4. Representative examples of unipolar electrograms from a plunge needle electrode spanning the thickness of the lateral LV wall during LDVF. *Control A* (*left column*) shows data from a control heart in which LDVF deteriorated to asystole. *Control B* (*center column*) show data from a control heart which maintained VF for at least 10 min of ischemia. GLYB (*right column*) shows data from a heart representing the glybenclamide group. At 0 min of ischemia (*top row*), VFR is similar between the different LV layers and between the *control A*, *control B*, and GLYB hearts. At 5 min of ischemia (*middle row*) an ENDO-to-EPI gradient (VFR faster in ENDO) develops in all hearts regardless of the absence or presence of glybenclamide. At 10 min of ischemia (*bottom row*), no activity can be seen in *control A* heart, whereas *control B* heart and GLYB heart still maintain electrical activity in ENDO and mid-myocardial leads (MID) but not EPI. Note that in the *control B* example only 8 electrograms are shown because the two most distal leads of the plunge needle were in the LV cavity and were not in contact with the myocardium. See text for more detail.

Figure 6 shows the same data as in Fig. 5, but this time the VFR curves are grouped by myocardial layer (EPI, MID, and ENDO). It can be seen that VFR in GLYB group was never lower, but became progressively higher than in control group throughout 10 min of LDVF. The divergence between control and GLYB groups was apparent first in ENDO (at ~1 min of LDVF) then in MID (at 2~3 min of LDVF) and then in EPI (at ~4 min of LDVF). The difference in VFR between control and GLYB groups was statistically significant in all layers.

Effect of glybenclamide on the epicardial VFR, APD, DI, and percentage of inexcitable area. While the electrode data described above enabled us to estimate the effect of glybenclamide on VFR in transmural layers of myocardium, optical mapping, albeit limited to the epicardial surface, enabled us to assess the effect of glybenclamide on APD, DI, and the extent of unexcited regions during LDVF (62). Examples of single pixel recordings are presented in Fig. 7. Figure 8 shows spatial distribution of VFR in a representative control (Fig. 8, *top*) and GLYB heart (Fig. 8, *bottom*). A palette of colors (from red to black) denotes different VFRs (from 11 to 0 Hz). Progressive decrease in VFR can be seen in both hearts; however, in the control heart the VFR decline occurs much faster. Focal loss of excitability emerges in the center of the mapped area as early as 4 min of LDVF and spreads to the entire mapped area by 5.5 min of LDVF. Later (at 8 min of LDVF), a small pocket of activity (VFR: ~1.5 Hz) reemerges in the right ventricular-septal area adjacent to the LAD, but it fails to activate LV. In contrast, in the representative GLYB heart (Fig. 8, *bottom*) activity is maintained in the entire mapped area throughout the first 10 min of LDVF. Note that a heterogeneous depression of activity is still present, but it does not reach the critical point of complete inexcitability.

Figure 9 shows the results of statistical analysis of OAPs obtained from the LV epicardium. Figure 9, *A–D*, shows the average values of VFR, APD, DI and percent of inexcitable

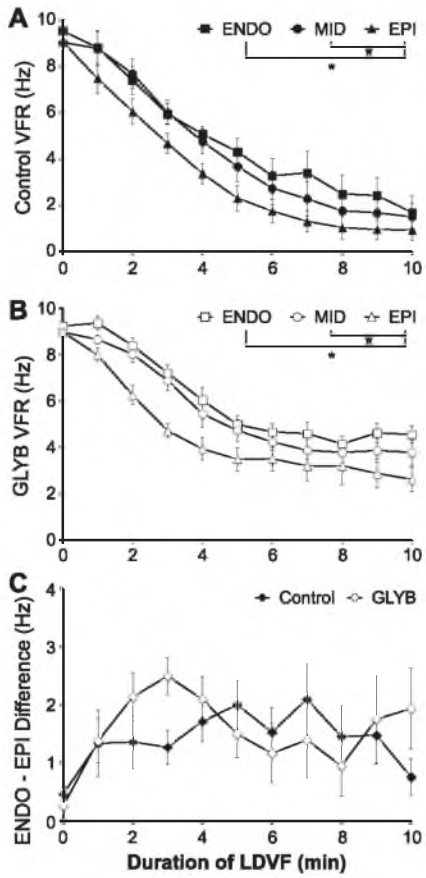

Fig. 5. Transmural distribution of VFR in LV during LDVF. *A* and *B*: VFR time course in ENDO (■, □), MID (●, ○), and EPI (▲, △) in control and glybenclamide groups, respectively. *C*: ENDO-EPI VFR difference in control and glybenclamide groups (derived from the same data as shown in *A* and *B*). ♦, controls; ◊ glybenclamide. *$P < 0.05$, significant difference between the curves by two-way ANOVA. Note that glybenclamide does not have a significant effect on the transmural VFR gradient.

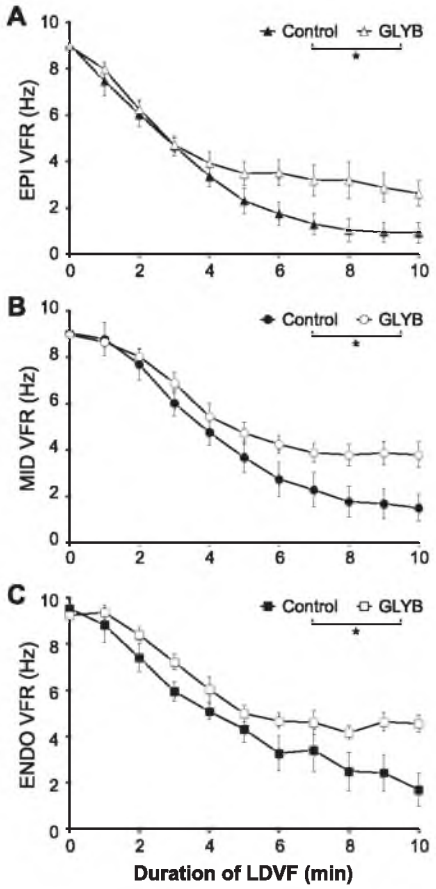

Fig. 6. Effect of glybenclamide on VFR time course in different layers of LV wall. Data are the same as in Fig. 5, but VFR curves are grouped by layer. *A–C*: represent EPI, MID, and ENDO, respectively. It is seen that glybenclamide maintained higher VFR in all layers, the difference increasing with the time of LDVF. This effect was statistically significant in all layers ($P < 0.05$).

area as a function of LDVF duration, respectively. It can be seen that glybenclamide postponed VFR decline in the epicardium; at each time point starting from 2 min of LDVF VFR was higher in GLYB than in control groups (Fig. 9*A*). The difference in VFR between control and GLYB groups increased with time reaching 1.5–2.0 Hz after 6 min of LDVF. Concomitant with VFR increase, glybenclamide significantly decreased average DI (Fig. 9*B*) while increasing APD (Fig. 9*C*). The most dramatic effect of glybenclamide treatment, however, was the prevention of local epicardial inexcitability (Fig. 9*D*). On average 57% of the mapped area in LV epicardium was inexcitable in control hearts vs. only 14% in GLYB hearts, by 10 min of LDVF. All differences shown in Fig. 9 were statistically significant ($P < 0.001$).

Possible confounding effects of glybenclmide. Figures 10 and 11 compare the VFR data obtained in control and GLYB groups with the data obtained from additional groups (CRO + 4AP and DOF, see MATERIALS AND METHODS), which served the purpose of addressing possible confounding effects of glybenclamide. In Fig. 10, VFR averaged across all myocardial layers was compared in the four groups during nonischemic VF (Fig. 10*A*) and at 10 min of ischemic VF (i.e., LDVF; Fig. 10*B*). In addition, Fig. 10*A* shows VFR measured in the presence of CRO and 4-AP alone, which was possible in CRO + 4AP group due to alternate order of the administration of the two drugs before the onset of LDVF (see MATERIALS AND METHODS). Figure 11 shows the VFR time course during LDVF in the four groups (control, GLYB, CRO + 4AP, and DOF). The data from control and GLYB groups are the same as in Figs. 5 and 6. VFR time course was compared among the four groups during late stage LDVF (from 5 to 10 min).

The first confounding factor to address is a substantial block of I_{to} by glybenclamide at the concentration used in this study (26). It was shown that blockade of I_{to} by 4-aminopyridine has a differential effect on the canine epicardium and endocardium during myocardial ischemia (33, 34), thus raising a possibility that I_{to} could contribute to the transmural VFR gradient during LDVF. However, 4-aminopyridine is not selective and was also shown to be a potent blocker of K_{ATP} (24). Thus the effects of both 4-aminopyridine and glybenclamide can be confounded by blockade, to various degrees, of both K_{ATP} and I_{to}. In this situation we tested the effect of 4-aminopyridine on VFR in the presence of K_{ATP} channel opener cromakalim. As shown in Fig. 10*A*, cromakalim very significantly increased VFR in nonischemic hearts (9.22 ± 0.27 vs. 19.00 ± 0.57 $P < 0.05$). However, 4-aminopyridine did not have any significant effect on VFR in either untreated (9.22 ± 0.27 vs. 8.78 ± 0.40) or cromakalim-treated (19.00 ± 0.57 vs. 17.57 ± 0.76) hearts under conditions of normal perfusion (see Fig. 10*A*). Despite the fact that during nonischemic VF the hearts from CRO + 4AP group had a much higher VFR than GLYB group, at 10 min of ischemic VF (LDVF) the relationship was reversed, that is, VFR in CRO + 4AP group was significantly lower than in GLYB group (0.40 ± 0.21 vs. 3.66 ± 0.33, $P < 0.05$; see Fig. 10*B*). As can be seen in Fig. 11, the reversal of the difference in VFR between the two groups occurred around ~4 min of LDVF. Collectively, these observations can be interpreted as follows: *1*) K_{ATP} activation increases VFR in nonischemic hearts but decreases VFR at advanced stages of ischemia; *2*) K_{ATP} blockade by glybenclamide prevents VFR decrease when K_{ATP} channel is activated at advanced stages of ischemia; and *3*) I_{to} blockade does not affect VFR regardless of opened or closed state of K_{ATP} channel. These arguments are further substantiated in the DISCUSSION.

Another potential confounding factor is a partial blockade by glybenclamide of the rapid component of the delayed rectifier potassium current, I_{Kr} (51). To address this issue, we treated six additional hearts with dofetilide (1 μM) before the onset of LDVF. As can be seen in Fig. 10A, dofetilide significantly decreased VFR in nonischemic hearts (9.22 ± 0.27 vs. 6.51 ± 0.24, $P < 0.05$). Also, at 10 min of LDVF VFR averaged across all layers was significantly lower in DOF group than in GLYB group (0.35 ± 0.29 vs. 3.66 ± 0.33, $P < 0.05$, see Fig. 10*B*). In fact, dofetilide caused a decrease in VFR in all layers throughout the entire episode of LDVF, the effect almost opposite to that of glybenclamide (see Fig. 11). Thus dofetilide did not reproduce the effects of glybenclamide in the setting of LDVF.

Finally, it should be noted that 6/6 GLYB hearts remained in VF, whereas only 4/9 Control, 2/6 CRO + 4AP, and 0/6 DOF hearts remained in VF at 10 min of ischemia. This further

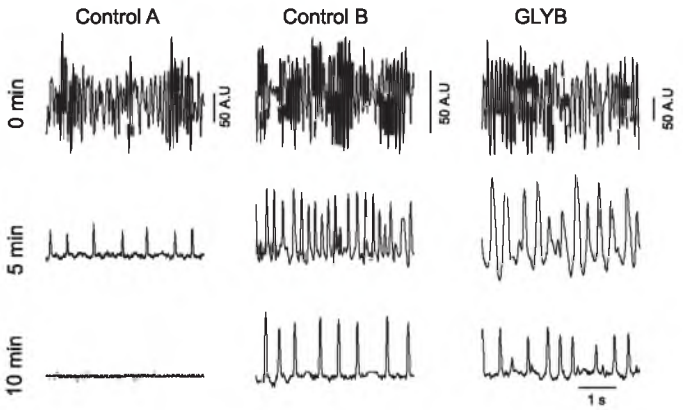

Fig. 7. Representative examples of single pixel recordings of optical action potential (OAPs) at different time points of LDVF. *Control A* (*left column*) shows data from a control heart in which LDVF deteriorated to asystole. *Control B* (*center column*) show data from a control heart which maintained VF for at least 10 min of ischemia. GLYB (*right column*) shows data from a heart representing glybenclamide group. At 0 min of ischemia (*top row*), high frequency activations with virtually absent diastolic intervals can be seen in all presented recordings. At 5 of ischemia (*middle row*), the OAP from *control A* heart exhibits a large degree of electrical depression manifested as very slow VFR and short APD amid very long diastolic interval (DI). At the same time, in both *control B* and GLYB hearts the respective OAPs exhibit more robust fibrillatory activity, albeit with slower VFR and longer DIs than at 0 min of LDVF. At 10 min of ischemia (*bottom row*), no activity is detectable in *control A* heart. In *control B* and GLYB hearts the fibrillatory activity is still present but VFR is slower and DIs are longer than at 5 min of LDVF. The large difference in the speed of electrical depression between the two selected control hearts is representative of large variation observed in the entire control group, which is also reflected in the large values of standard error in the measurements of DI and percentage of inexcitable area (see Fig. 9, *C* and *D*).

supports the unique role of glybenclamide in maintaining VF in structurally normal globally ischemic canine hearts.

DISCUSSION

In this study we investigated the role of K_{ATP} channels in the evolution of LDVF in structurally normal canine heart. The main finding is that K_{ATP} channel blockade by glybenclamide significantly delayed the transition from depressed excitability to complete electrical standstill during LDVF. However, K_{ATP} channel blockade had only modest effect on the speed of VFR decline and the transmural VFR gradient.

Efficacy and specificity of glybenclamide as an I_{KATP} blocker during LDVF. It should be noted that efficacy of glybenclamide and other sulfonylureas may be limited in the presence of elevated intracellular ADP concentration ($[ADP]_i$) during ischemia, so that concentrations from 30 to 100 μM may be required to achieve significant blockade of K_{ATP} channels (63). The extent of $[ADP]_i$ elevation during acute ischemia is not well known and may differ between different species and/or experimental models. Our experiments using glybenclamide in concentrations ~30 μM showed only marginal differences between treated and nontreated hearts (not shown) whereas other investigators were able to see effects of glybenclamide during ischemia with respect to various electrophysiological parameters at concentrations as low as 1–10 μM (3, 13, 46). However, most of the studies using low concentrations of glybenclamide were performed in isolated cells or thin superfused preparations. In our experiments, glybenclamide was delivered via coronary circulation which could reduce the effective concentration of the drug visible to cardiac myocytes due to drug binding with the membranes of blood cells and/or endothelium (9). Furthermore, the apparently lower efficacy of glybenclamide in our study could be due to more pronounced rise in $[ADP]_i$, presumably as a result of greater energy imbalance during LDVF as opposed to ischemia alone. In any case, the concentration of glybenclamide used in our study was sufficient to reveal a significant role of K_{ATP} channels in the development of inexcitability and asystole during LDVF. However, we cannot exclude that the role of I_{KATP} with respect to the speed of VFR decline and transmural VFR distribution during LDVF is larger than what can be inferred from the results of this study.

Whereas a relatively high concentration of glybenclamide (60 μM) was necessary to achieve a sufficient blockade of K_{ATP}, this concentration could also potentially block other channels. Previous studies (31) have shown that glybenclamide can also reduce both the sodium-potassium pump (Na-K pump) current and L-type calcium current (I_{CaL}) by ~18% at 60 μM. Despite the partial blockade of the Na-K pump Venkatesh et al. (63) have shown that during ischemia, high concentrations of glybenclamide (up to 100 μM) reduces extracellular K^+ accumulation, suggesting Na-K pump blockade plays a limited role, if any. It is unlikely that partial I_{CaL} blockade by glybenclamide affected the main results of this study (delay of inexcitability and asystole), since decrease in I_{CaL} should promote inexcitability because during ischemia I_{CaL} plays a larger role in supporting propagation in partially depolarized myocardium (55). One could argue that an inhibition of I_{CaL} by glybenclamide can preserve electrical activity by reducing contractility and thus energy expenditure during LDVF. However, glybenclamide at a concentration similar to that used in this study (100 μM) actually moderately increases contractility in nonischemic hearts and does not affect the decline in contractility during ischemia (e.g., see Fig. 6 in Ref. 63). The increase in contractility by glybenclamide was also demonstrated in isolated ventricular myocytes (28). This effect occurred despite decrease in the peak I_{CaL} and was associated with increase in intracellular calcium by a mechanism not fully understood

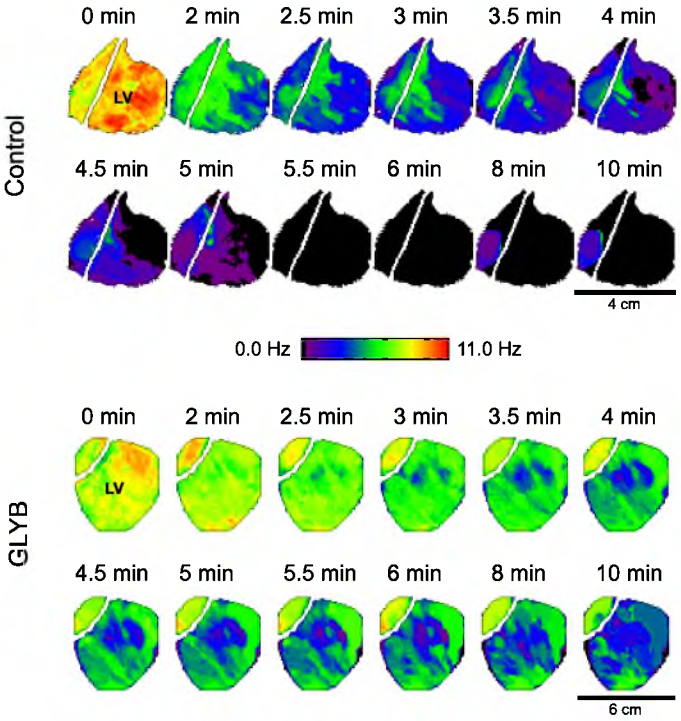

Fig. 8. Representative examples of VFR distribution maps derived from optical mapping of anterior LV during LDVF in a control (*top*) and a glybenclamide-treated (*bottom*) heart. Labels above the maps indicate the respective time points during LDVF. Colors (from black to red) indicate VFR in Hz (from 0 to 11 Hz). Note that the overall VFR decline occurs faster in the control than in the glybenclamide heart. Note also that in the control heart inexcitable areas (black) start to emerge as early as at 4 min of LDVF and culminate in complete absence of activation by 5.5 min of ischemia. At 8 min, highly localized and slow activity reemerges at the RV-septal junction but fails to activate LV. In GLYB heart, VFR decline occurs slower than in control and, despite VFR slowing, the entire mapped area maintains excitability throughout 10 min of global ischemia.

(28). Thus neither electrophysiological nor contractile factors associated with modest I_{CaL} inhibition caused by glybenclamide can explain the outcomes of this study.

Another concern is a reported 40% reduction in I_{Kr} in the presence of 60 μM glybenclamide (51). To address the potential effect of glybenclamide on I_{Kr} during ischemia, we elected to determine what role I_{Kr} blockade would play in electrical depression during LDVF. Dofetilide was chosen due to its properties as a highly specific and effective I_{Kr} blocker: dofetilide blocks almost 100% of I_{Kr} at 1 μM and has virtually no effect on the slow component of the delayed rectifying potassium current (5). Dofetilide shows dose-dependent block of

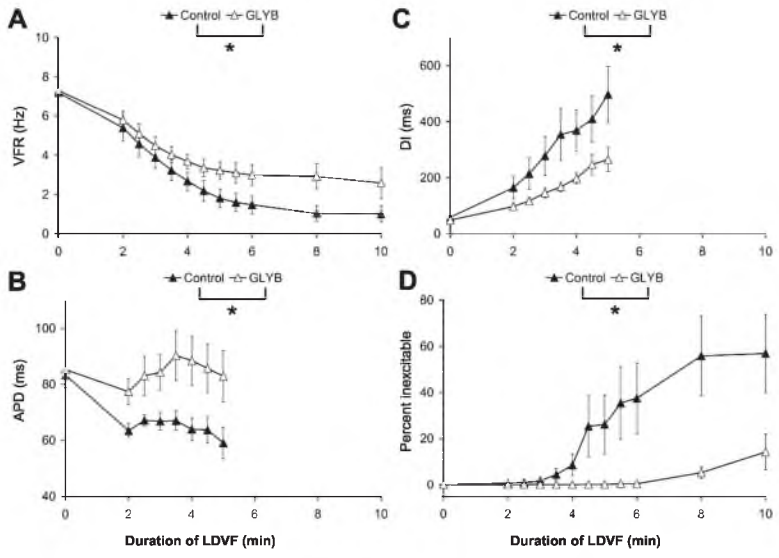

Fig. 9. Comparison of the time courses of VFR (*A*), DI (*B*), APD (*C*), and the percentage of inexcitable area (*D*) in epicardial optical maps during LDVF in control and GLYB hearts. *$P <$ 0.05, statistically significant difference between the respective curves by two-way ANOVA.

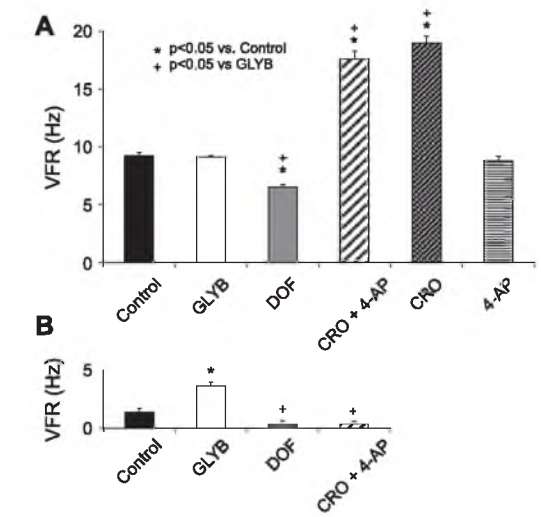

Fig. 10. Comparison of VFR averaged across all myocardial layers in different groups during nonischemic VF (*A*) and at 10 min of LDVF (*B*). GLYB, 60 μM; DOF, dofetilide (1 μM); CRO, cromakalim (10 μM); 4-AP, 4-aminopyridine (1 mM); CRO + 4AP, combination of cromakalim and 4-aminopyridine. See text for more detail.

I_{KATP} but at much higher concentrations than what was used in our study (EC_{50} of 51 ± 1 μM in inside-out patches, and lesser efficacy when dofetilide is applied outside the cell; Ref. 65). Comparing the effects of glybenclamide and dofetilide in our study suggests that potential blockade of I_{Kr} by 60 μM glybenclamide does not affect the main phenomenon, since dofetilide lowered VFR whereas glybenclamide increased VFR (see Fig. 11). Also, dofetilide aborted LDVF in all experiments, whereas glybenclamide maintained LDVF in all experiments, within the tested 10-min interval. It is of interest that dofetilide appeared to preferentially decrease VFR in ENDO (see Fig. 11). Assuming a leading role of endocardial Purkinje fibers in maintaining LDVF in dog heart (56), the prominent antifibrillatory effect of dofetilide observed in this study could be explained in terms of efficient suppression of arrhythmic sources associated with ischemic Purkinje fibers. This intriguing possibility is beyond the scope of the current study but merits further investigation.

Another concern caused by the use of 60 uM of glybenclamide is the substantial (~60%) blockade of I_{to} (26). It was suggested that I_{to} plays an important role in setting up conditions for heterogeneous APD distribution and reentry during simulated ischemia by promoting loss of the action potential "dome" on the epicardium, which could be prevented by the I_{to} blocker 4-aminopyridine (33, 34). Thus blockade of I_{to} by glybenclamide could, in theory, contribute to the effects of glybenclamide on LDVF observed in this study. It should be noted however, that the effects of 4-aminopyridine on APD during ischemia were sensitive to stimulation rates and were largely absent at rates >2 Hz (the lower bound of activation rates observed during LDVF in our study). This can be explained by relatively slow reactivation kinetics of I_{to} in canine ventricular myocytes (32) and/or reverse use dependence of block by 4-aminopyridine (4). In addition, the suggested role of I_{to} was demonstrated only during "simulated" ischemia (33, 34) and was exclusively based on the effects of 4-aminopyridine, a relatively nonselective potassium channel blocker. At millimolar concentrations needed for efficient I_{to} blockade 4-aminopyridine can cause significant inhibition of I_{KATP} (IC_{50} of 2.1 ± 0.3 mM; Ref. 24).

In our study, we tested the combined effects of 4-aminopyridine and a K_{ATP} opener cromakalim. In nonischemic hearts, 4-aminopyridine did not have any significant effect on VFR both in the absence and in the presence of cromakalim (see Fig. 10*A*). This suggests that blockade by 4-aminopyridine of either I_{to} or K_{ATP} does not have any significant role in determining the excitation rate during VF. In contrast, activation of K_{ATP} had a dramatic effect on VFR in nonischemic hearts, increasing VFR almost twofold over nontreated hearts. In the course of LDVF the difference in VFR between CRO + 4AP and GLYB groups progressively diminished until the VFR curves in the two groups crossed over, so that VFR in CRO + 4AP group became lower than in GLYB group (see Fig. 11). It is striking that whenever the effect of glybenclamide was detectable

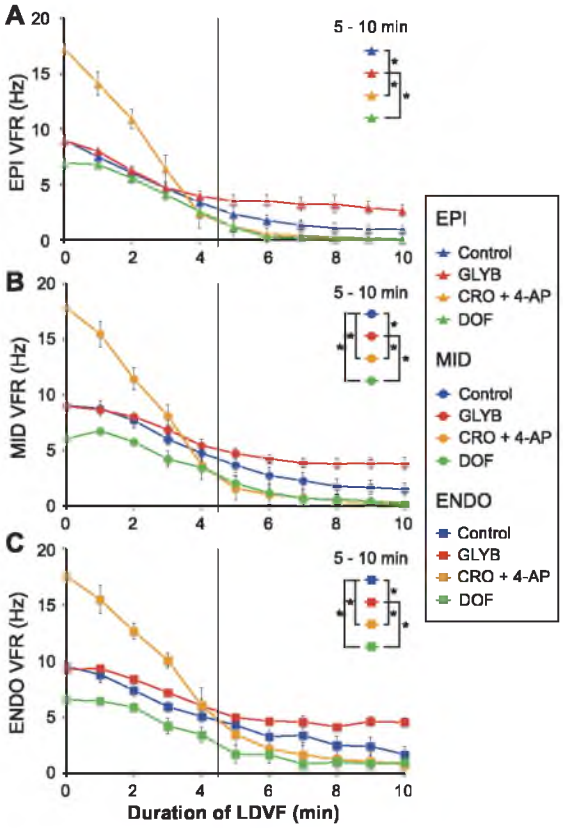

Fig. 11. VFR time course during LDVF in control, GLYB, CRO + 4AP, and DOF groups. Data from control and GLYB groups are the same as in Figs. 5 and 6. VFR time course was compared among the 4 groups during late stage LDVF (from 5 to 10 min) using a two-way ANOVA. *A–C*: represent EPI, MID, and ENDO, respectively. *Statistical differences between individual groups.

(namely, 2–4 min after the onset of LDVF) it was opposite to the effect exerted by the combination of cromakalim and 4-aminopyririne. Assuming that inhibition of I_{to} was at least the same (or larger) in CRO + 4AP than in GLYB group, the polar difference between these two groups can hardly be explained in terms of I_{to} blockade. Rather, this difference would be consistent with the idea that after 4 min of LDVF activation of K_{ATP} by cromakalim further promotes electrical depression manifested as VFR decline, whereas blockade of K_{ATP} by glybenclamide prevents that effect.

Summarizing arguments above, we conclude that the main effects of glybenclamide observed in this study, namely, maintenance of higher VFR and excitable state during LDVF are best explained in terms of K_{ATP} blockade since among all known possible targets of glybenclamide only K_{ATP} channel opening is relevant to loss of excitability during ischemia, as discussed in more detail below.

I_{KATP} and electrical depression during LDVF. During myocardial ischemia, a number of factors promote depression of excitability and conduction failure including hyperkalemia, acidosis, and activation of I_{KATP} (55). Opening of K_{ATP} channels during LDVF may facilitate loss of excitability in two ways: first, by its contribution to the level of extracellular K^+ concentration ($[K^+]_o$) increase (66), and second, by creating conditions of source-sink mismatch when I_{Na} is already reduced due to elevated $[K^+]_o$ (55). In isolated ventricular cardiomyocytes, complete loss of excitability can occur when K_{ATP} is sufficiently activated in response to mitochondrial depolarization, even without any increase in $[K^+]_o$ (1). We are not aware of any published data regarding the dynamics of $[K^+]_o$ during LDVF. Although, in the center of the ischemic zone of regionally ischemic isolated canine hearts paced at cycle length of 350–450 ms, $[K^+]_o$ reached ~8 mM after 8 min of coronary occlusion (11). At that level of K^+ elevation, ~20% of unipolar electrograms in the ischemic zone exhibited "block" morphology (i.e., lack of negative intrinsic deflection), which can be interpreted as indicative of conduction block at the recording site. In our study, a similar percentage of inexcitable sites was achieved ~4 min earlier in the course of LDVF (see Fig. 9*D*). This comparison suggests that either the level of $[K^+]_o$ or the level of I_{KATP} activation, or both, could be considerably higher during LDVF than ischemia alone, perhaps due to ionic and/or metabolic consequences of very high excitation rate.

K_{ATP} channel activation and heterogeneities in VFR and excitability during LDVF. It has been shown that epicardial myocytes are more susceptible to the electrophysiological effects of ischemia than are endocardial cells, in particular with regard to ischemia-induced APD shortening. Several studies (19, 39, 40) have implicated the higher level of K_{ATP} channel expression and/or activation on the epicardium in this phenomenon. In contrast to those earlier studies, Farid et al. (15) reported a higher expression of K_{ATP} subunits in the endocardium of failing human hearts, which was consistent in their study with preferential effect of glybenclamide (slowing of the excitation rate during LDVF) in the endocardium. The authors attributed this effect to preferential prolongation of APD by glybenclamide in endocardial cells but provided very limited evidence to support that statement.

In our study, pretreatment with glybenclamide slightly prolonged APD in the epicardium during the combination of VF and ischemia, which is consistent with the known effect of I_{KATP} blockade with respect to APD during ischemia alone. However, this was of little consequence for the dynamics of VFR. If prolongation of APD were the only effect of glybenclamide, then we would expect a prolongation of VFCL (hence, a decrease in VFR). On the contrary, epicardial VFCL shortened and VFR increased in the presence of glybenclamide, despite prolongation of APD although concomitant with shortening of DI. Therefore, at least in the epicardium, the effect of glybenclamide on VFR was determined by its effect on DI. Using intramural optrodes, Kong et al. (30) recently showed that the activation rate during LDVF in all layers of the ventricular wall was predominantly determined by DI amid a relatively constant APD. Unfortunately, we did not have means to measure the effect of glybenclamide on APD and DI during LDVF in intramural layers. However, extrapolating the results obtained with optical mapping on the epicardium, it is likely that the VFR increase observed in mid- and endocardial electrograms in the presence of glybenclamide is also associated with shortening of DI.

In light of previous studies suggesting differential properties of K_{ATP} channels in the endocardium vs. epicardium (39, 40). it is surprising that K_{ATP} channel blockade did not affect the transmural VFR gradient in our study (see Fig. 5). If the VFR gradient were predominantly due to transmural differences in K_{ATP} activation, then blockade of this channel should have abolished the gradient. In fact, such abolishment was observed during LDVF in explanted failed human hearts (15), in stark contrast to our results (possible reasons for this discrepancy will be discussed below). The lack of effect of glybenclamide in our study indicates that other factor(s) are sufficient to create conditions for the VFR gradient during LDVF in the structurally normal canine heart. Note that once a VFR gradient is established due to these other factors, the (presumably) higher availability of K_{ATP} channels in the epicardium can be offset by a lower value of total depolarization time in the epicardium due to fewer action potentials with shorter APDs. As a result, even though more channels are opened, the total current over a period of time will be small because most of the time the membrane potential will be close to the potassium equilibrium potential. Factors contributing to the transmural VFR gradient during LDVF may include transmural differences in properties of I_{Na} inactivation (10); transmural distribution of mechanical stress (20, 64) with attendant changes in the function of stretch-activated channels and other channels, including K_{ATP} (60, 61); lower expression of connexin 43 in the epicardium compared with deeper layers of the ventricular wall (47); and heterogeneous expression/function of several other channels and tranporters [for more detailed discussion, see our previous publication (62)].

Even though K_{ATP} channel blockade markedly reduced the percentage of inexcitable area, it did not remove local (at the scale of millimeters) heterogeneities observed with optical mapping in the epicardium. Such local heterogeneities in the degree of electrical depression during LDVF may be related to spatially heterogeneous elevation of $[K^+]_o$, which can be observed even during global ischemia (29). The reasons for small-scale heterogeneities in the electrophysiological effects of (apparently uniform) global ischemia remain unknown.

Role of K_{ATP} channel in asystole and outcomes of resuscitation. During global ischemia associated with cardiac arrest of any etiology, asystole should inevitably occur, if not intervened, as a natural step towards death. However, the timing and the circumstances of asystole do matter. In the setting of out-of-hospital sudden cardiac arrest (OHSCA), asystole is not treatable with defibrillation shock and is associated with an extremely low rate of survival (23). In recent years, the incidence of asystole as the initial presenting rhythm remained the same or increased, amid a robust decrease in the incidence of VF (8, 48). At this point, one can only speculate what has caused the change in the proportion between VF and asystole in the OHSCA population. In most cases, the rhythm precipitating cardiac arrest in the out-of-hospital setting is not known. Recordings obtained from postmortem interrogation of Holter monitors, implantable cardioverter defibrillators, or implantable loop recorders in selected groups of patients with prior history of heart disease showed that from 40 to 80% of these patients had VF as the terminal rhythm at the time of unexpected death (21, 35, 38). The incidence of VF as the rhythm preceding death was generally lower in patients with advanced stages of heart failure (35) and higher in patients with prior myocardial infarction (21). It should be noted that the high-risk sudden cardiac death patients being monitored either in hospital or ambulatory are likely to be different from the residents in the general community that have sudden cardiac death, often as the very first manifestation of heart disease (7). Thus it is very difficult to estimate at this point what proportion of asystole in OHSCA is due to early transition from VF to asystole as opposed to asystole as a culmination of severe bradycardia and pulseless electrical activity (45). However, in both scenarios the mechanism of rapid deterioration to asystole may involve enhanced activation of I_{KATP}, which may affect not only ventricles but also atria and/or the specialized conducting system of the heart. At least in the three asystolic hearts where we attached pacing and recording electrodes to the right atrium, atria did not show any spontaneous activity and did not respond to stimulation after VF termination. This observation warrants closer attention to the role of supraventricular tissues in the events occurring during cardiac arrest. Indeed, suppression of the sinus node activity due to activation of I_{KATP} (18) alone may be sufficient to prevent restoration of spontaneous circulation under these conditions. These assumptions have to be tested in future studies.

Our study shows that activation of I_{KATP} is a major determinant of asystole as the outcome of LDVF. That is, blockade of K_{ATP} channel supports maintenance of VF within the clinically relevant time window. This is consistent with a previous study by Tang et al. (58) using an open-chest rat model of resuscitation, where activation of K_{ATP} channel either by use of a K_{ATP} channel agonist or by ischemic preconditioning promoted spontaneous VF termination. In our study, however, VF termination was followed by asystole (adverse outcome) whereas in that study it was followed by restoration of sinus rhythm (benign outcome). The discrepancy may be due to differences between species and/or experimental conditions. However, it brings up an important point that in the setting of LDVF the net effect of K_{ATP} channel activation/blockade depends on the balance between the effects with respect to VF dynamics and the effects with respect to generation and delivery of the sinus node impulses to the ventricles.

Comparison to explanted cardiomyopathic human heart. A recently published study by Farid et al. (15) investigated the role of I_{KATP} in the dynamics and the outcome of LDVF induced in Langendorff-perfused hearts explanted from human patients with end-stage heart failure. The difference between our study and that by Farid et al. is quite striking; essentially, the results are opposite in many respects. The most important difference is that in our study glybenclamide prevented VF termination, whereas in their study this drug promoted VF termination in the globally ischemic heart. In our study, there was no major effect of glybenclamide with respect to the difference in excitation rate during LDVF between ENDO and EPI; in their study, this difference was effectively eliminated by glybenclamide. Lastly, in our study, there was no detectable effect of glybenclamide at the onset of LDVF; in their study that effect was profound (see their Fig. 4*A*).

The latter difference, in fact, may be key to the discrepant results. Excluding trivial explanations in terms of unintentional metabolic stresses associated with various stages of preparation preceding the actual experiment, the prominent effect of glybenclamide in an essentially nonischemic heart may be related to the fact that the hearts at advanced stages of dilated cardiomyopathy are metabolically compromised to such extent that I_{KATP} is activated even without overt ischemia. This assumption would be consistent with reports indicating severe energy deprivation in failing hearts (42), and a possibility that K_{ATP} channel regulation is altered in response to congestive heart failure (16).

Another factor in the difference between LDVF dynamics in normal vs. failing hearts (ignoring for the moment interspecies differences) may be related to downregulation of repolarizing potassium currents such as I_{to} and I_{Kr} in failing hearts (59). This may lead to a significant prolongation of APD, which in turn may slow down the excitation rate during VF. In agreement with this conjecture, blockade of I_{Kr} with dofetilide in our model significantly decreased VF rate in both nonischemic and ischemic hearts (see Figs. 10 and 11). Moreover, dofetilide affected VF maintenance so that in two out of six hearts treated with dofetilide VF stopped spontaneously within 1 or 2 min after its induction (not shown), an event never observed in untreated canine hearts.

If the two assumptions mentioned above (downregulation of voltage-dependent potassium currents and an apparent upregulation of I_{KATP} in failing human hearts) are correct, the difference between our study and that by Farid et al. could be explained in terms of different timing of K_{ATP} activation in the two models and varying role of I_{KATP} in LDVF dynamics depending on the stage of ischemia. Our data show that when K_{ATP} is deliberately activated, its effect changes in the course of LDVF, which might depend on the magnitude of other detrimental factors of ischemia such as extracellular potassium accumulation. Namely, K_{ATP} activation increases VFR in the early stage (3–4 min) and decreases VFR at the late stage (5–10 min) of LDVF (see Fig. 11). Based on the effects of K_{ATP} blockade by glybenclamide, it appears that the principal difference between the normal canine heart and failing human hearts is the level of K_{ATP} activation at the early stage of LDVF: high in failing human hearts vs. low in normal canine hearts. Note that the study by Farid et al. (15) was limited to only the first 3 min of LDVF, the time frame when K_{ATP} activation is expected to increase VFR and, conversely, K_{ATP}

blockade is expected to reduce VFR if K_{ATP} channel is activated. Note also that in failing human hearts the very existence of sustained VF may require K_{ATP} activation to overcome the antifibrillatory effect of dramatic APD prolongation caused by downregulation of repolarizing potassium currents. In this regard, it is interesting to note that prevalence of VF as the rhythm causing cardiac arrest is low in patients with advanced stages of heart failure compared with other cardiac conditions (21, 35, 38).

Clinical implications. Together with previous publications, our study underscores the very complex role of K_{ATP} channel in cardiac arrest. While in the structurally normal canine heart, K_{ATP} channel blockade supports maintenance of VF in globally ischemic heart (this study), in failing human heart the effect is exactly opposite: VF termination (15). The latter outcome is good only if it is followed by restoration of spontaneous rhythm, but is lethal if it is followed by asystole. K_{ATP} channel activation can promote loss of excitability (this study) and postreperfusion arrhythmias (1), yet upon resuscitation and reperfusion enhanced K_{ATP} channel activation can also afford better recovery of hemodynamics and, ultimately, survival (58). Future therapeutic strategies aimed at improving the outcomes of cardiac arrest must therefore address the challenge of separating the adverse effects of K_{ATP} channel activation from the protective ones.

Limitations. Limitations related to the reduced blocking efficacy of glybenclamide in the presence of elevated $[ADP]_i$ (63) and potential blockade of I_{Kr}, I_{to}, and other nonspecific effects have been thoroughly addressed above. Other common limitations of the ex vivo model of LDVF, plunge needle electrodes, and optical mapping are discussed in our previous publications (27, 62).

ACKNOWLEDGMENTS

We are indebted to Jayne H. Davis, Alicja Booth, and Nancy C. Allen for excellent technical support.

GRANTS

This work was supported by National Heart, Lung, and Blood Institute Grants 5R01-HL-088444 and 1RO1-HL-103877 (to A..V. Zaitsev) and 1F32-HL-097576 (to J. Shibayama) and a Nora Eccles Treadwell Foundation Research Grant (to A. V. Zaitsev).

DISCLOSURES

No conflicts of interest, financial or otherwise, are declared by the author(s).

AUTHOR CONTRIBUTIONS

Author contributions: T.G.T. and A.V.Z. conception and design of research; T.G.T., P.W.V., J.S., M.W., and A.V.Z. performed experiments; T.G.T., P.W.V., and A.V.Z. analyzed data; T.G.T., P.W.V., J.S., M.W., and A.V.Z. interpreted results of experiments; T.G.T. and P.W.V. prepared figures; T.G.T. and A.V.Z. drafted manuscript; T.G.T. and A.V.Z. edited and revised manuscript; T.G.T. and A.V.Z. approved final version of manuscript.

REFERENCES

1. **Akar FG, Aon MA, Tomaselli GF, O'Rourke B.** The mitochondrial origin of postischemic arrhythmias. *J Clin Invest* 115: 3527–3535, 2005.
2. **Allison JS, Qin H, Dosdall DJ, Huang J, Newton JC, Allred JD, Smith WM, Ideker RE.** The transmural activation sequence in porcine and canine left ventricle is markedly different during long-duration ventricular fibrillation. *J Cardiovasc Electrophysiol* 18: 1306–1312, 2007.
3. **Baker JE, Contney SJ, Gross GJ, Bosnjak ZJ.** KATP channel activation in a rabbit model of chronic myocardial hypoxia. *J Mol Cell Cardiol* 29: 845–848, 1997.
4. **Campbell DL, Qu Y, Rasmusson RL, Strauss HC.** The calcium-independent transient outward potassium current in isolated ferret right ventricular myocytes. II. Closed state reverse use-dependent block by 4-aminopyridine. *J Gen Physiol* 101: 603–626, 1993.
5. **Carmeliet E.** Voltage- and time-dependent block of the delayed K+ current in cardiac myocytes by dofetilide. *J Pharmacol Exp Ther* 262: 809–817, 1992.
6. **Cha YM, Uchida T, Wolf PL, Peters BB, Fishbein MC, Karagueuzian HS, Chen PS.** Effects of chemical subendocardial ablation on activation rate gradient during ventricular fibrillation. *Am J Physiol Heart Circ Physiol* 269: H1998–H2009, 1995.
7. **Chugh SS, Reinier K, Teodorescu C, Evanado A, Kehr E, Al Samara M, Mariani R, Gunson K, Jui J.** Epidemiology of sudden cardiac death: clinical and research implications. *Prog Cardiovasc Dis* 51: 213–228, 2008.
8. **Cobb LA, Fahrenbruch CE, Olsufka M, Copass MK.** Changing incidence of out-of-hospital ventricular fibrillation, 1980–2000. *JAMA* 288: 3008–3013, 2002.
9. **Conway MA, Nelson MT, Brayden JE.** 2-Deoxyglucose-induced vasodilation and hyperpolarization in rat coronary artery are reversed by glibenclamide. *Am J Physiol Heart Circ Physiol* 266: H1322–H1326. 1994.
10. **Cordeiro JM, Mazza M, Goodrow R, Ulahannan N, Antzelevitch C, Di Diego JM.** Functionally distinct sodium channels in ventricular epicardial and endocardial cells contribute to a greater sensitivity of the epicardium to electrical depression. *Am J Physiol Heart Circ Physiol* 295: H154–H162, 2008.
11. **Coronel R, Fiolet JW, Wilms-Schopman JG, Opthof T, Schaapherder AF, Janse MJ.** Distribution of extracellular potassium and electrophysiologic changes during two-stage coronary ligation in the isolated, perfused canine heart. *Circulation* 80: 165–177, 1989.
12. **Daut J, Maier-Rudolph W, von Beckerath N, Mehrke G, Gunther K, Goedel-Meinen L.** Hypoxic dilation of coronary arteries is mediated by ATP-sensitive potassium channels. *Science* 247: 1341–1344, 1990.
13. **Di Diego JM, Antzelevitch C.** Pinacidil-induced electrical heterogeneity and extrasystolic activity in canine ventricular tissues. Does activation of ATP-regulated potassium current promote phase 2 reentry? *Circulation* 88: 1177–1189, 1993.
14. **Dosdall DJ, Tabereaux PB, Kim JJ, Walcott GP, Rogers JM, Killingsworth CR, Huang J, Robertson PG, Smith WM, Ideker RE.** Chemical ablation of the Purkinje system causes early termination and activation rate slowing of long-duration ventricular fibrillation in dogs. *Am J Physiol Heart Circ Physiol* 295: H883–H889, 2008.
15. **Farid TA, Nair K, Masse S, Azam MA, Maguy A, Lai PF, Umapathy K, Dorian P, Chauhan V, Varro A, Al-Hesayen A, Waxman M, Nattel S, Nanthakumar K.** Role of KATP channels in the maintenance of ventricular fibrillation in cardiomyopathic human hearts. *Circ Res* 109: 1309–1318, 2011.
16. **Fedorov VV, Glukhov AV, Ambrosi CM, Kostecki G, Chang R, Janks D, Schuessler RB, Moazami N, Nichols CG, Efimov IR.** Effects of KATP channel openers diazoxide and pinacidil in coronary-perfused atria and ventricles from failing and non-failing human hearts. *J Mol Cell Cardiol* 51: 215–225, 2011.
17. **Flagg TP, Nichols CG.** Sarcolemmal K(ATP) channels: what do we really know? *J Mol Cell Cardiol* 39: 61–70, 2005.
18. **Fukuzaki K, Sato T, Miki T, Seino S, Nakaya H.** Role of sarcolemmal ATP-sensitive K^+ channels in the regulation of sinoatrial node automaticity: an evaluation using Kir6.2-deficient mice. *J Physiol* 586: 2767–2778, 2008.
19. **Furukawa T, Kimura S, Furukawa N, Bassett AL, Myerburg RJ.** Role of cardiac ATP-regulated potassium channels in differential responses of endocardial and epicardial cells to ischemia. *Circ Res* 68: 1693–1702, 1991.
20. **Gallagher KP, Osakada G, Matsuzaki M, Miller M, Kemper WS, Ross J Jr.** Nonuniformity of inner and outer systolic wall thickening in conscious dogs. *Am J Physiol Heart Circ Physiol* 249: H241–H248, 1985.
21. **Gang UJ, Jons C, Jorgensen RM, Abildstrom SZ, Haarbo J, Messier MD, Huikuri HV, Thomsen PE.** Heart rhythm at the time of death documented by an implantable loop recorder. *Europace* 12: 254–260, 2010.
22. **Hallstrom A, Herlitz J, Kajino K, Olasveengen TM.** Treatment of asystole and PEA. *Resuscitation* 80: 975–976, 2009.
23. **Hallstrom A, Rea TD, Mosesso VN Jr, Cobb LA, Anton AR, Van Ottingham L, Sayre MR, Christenson J.** The relationship between

shocks and survival in out-of-hospital cardiac arrest patients initially found in PEA or asystole. *Resuscitation* 74: 418–426, 2007.

24. **Haworth RA, Goknur AB, Berkoff HA.** Inhibition of ATP-sensitive potassium channels of adult rat heart cells by antiarrhythmic drugs. *Circ Res* 65: 1157–1160, 1989.
25. **Herlitz J, Svensson L, Engdahl J, Silfverstolpe J.** Characteristics and outcome in out-of-hospital cardiac arrest when patients are found in a non-shockable rhythm. *Resuscitation* 76: 31–36, 2008.
26. **Hernandez-Benito MJ, Macianskiene R, Sipido KR, Flameng W, Mubagwa K.** Suppression of transient outward potassium currents in mouse ventricular myocytes by imidazole antimycotics and by glybenclamide. *J Pharmacol Exp Ther* 298: 598–606, 2001.
27. **Huizar JF, Warren MD, Shvedko AG, Kalifa J, Moreno J, Mironov S, Jalife J, Zaitsev AV.** Three distinct phases of VF during global ischemia in the isolated blood-perfused pig heart. *Am J Physiol Heart Circ Physiol* 293: H1617–H1628, 2007.
28. **Khatib SY, Boyett MR.** Effects of glyburide (glibenclamide) on myocardial function in Langendorff perfused rabbit heart and on myocardial contractility and slow calcium current in guinea-pig single myocytes. *Mol Cell Biochem* 242: 81–87, 2003.
29. **Kim JJCS, Gabris B, Waggoner A, Salama G.** Optical measurements of extracellular potassium accumulation (EKA) during ischemia with new potassium sensitive dyes. *Heart Rhythm* 7: S261, 2010.
30. **Kong W, Ideker RE, Fast VG.** Transmural optical measurements of Vm dynamics during long-duration ventricular fibrillation in canine hearts. *Heart Rhythm* 6: 796–802, 2009.
31. **Lee SY, Lee CO.** Inhibition of Na^+-K^+ pump and L-type Ca^{2+} channel by glibenclamide in Guinea pig ventricular myocytes. *J Pharmacol Exp Ther* 312: 61–68, 2005.
32. **Liu DW, Gintant GA, Antzelevitch C.** Ionic bases for electrophysiological distinctions among epicardial, midmyocardial, and endocardial myocytes from the free wall of the canine left ventricle. *Circ Res* 72: 671–687, 1993.
33. **Lukas A, Antzelevitch C.** Differences in the electrophysiological response of canine ventricular epicardium and endocardium to ischemia. Role of the transient outward current. *Circulation* 88: 2903–2915, 1993.
34. **Lukas A, Antzelevitch C.** Phase 2 reentry as a mechanism of initiation of circus movement reentry in canine epicardium exposed to simulated ischemia. *Cardiovasc Res* 32: 593–603, 1996.
35. **Luu M, Stevenson WG, Stevenson LW, Baron K, Walden J.** Diverse mechanisms of unexpected cardiac arrest in advanced heart failure. *Circulation* 80: 1675–1680, 1989.
36. **Massé S, Downar E, Chauhan V, Sevaptsidis E, Nanthakumar K.** Ventricular fibrillation in myopathic human hearts: mechanistic insights from in vivo global endocardial and epicardial mapping. *Am J Physiol Heart Circ Physiol* 292: H2589–H2597, 2007.
37. **Masse S, Farid T, Dorian P, Umapathy K, Nair K, Asta J, Ross H, Rao V, Sevaptsidis E, Nanthakumar K.** Effect of global ischemia and reperfusion during ventricular fibrillation in myopathic human hearts. *Am J Physiol Heart Circ Physiol* 297: H1984–H1991, 2009.
38. **Mitchell LB, Pineda EA, Titus JL, Bartosch PM, Benditt DG.** Sudden death in patients with implantable cardioverter defibrillators: the importance of post-shock electromechanical dissociation. *J Am Coll Cardiol* 39: 1323–1328, 2002.
39. **Miyoshi S, Miyazaki T, Asanagi M, Moritani K, Ogawa S.** Differential role of epicardial and endocardial K(ATP) channels in potassium accumulation during regional ischemia induced by embolization of a coronary artery with latex. *J Cardiovasc Electrophysiol* 9: 292–298, 1998.
40. **Miyoshi S, Miyazaki T, Moritani K, Ogawa S.** Different responses of epicardium and endocardium to KATP channel modulators during regional ischemia. *Am J Physiol Heart Circ Physiol* 271: H140–H147, 1996.
41. **Nash MP, Mourad A, Clayton RH, Sutton PM, Bradley CP, Hayward M, Paterson DJ, Taggart P.** Evidence for multiple mechanisms in human ventricular fibrillation. *Circulation* 114: 536–542, 2006.
42. **Neubauer S.** The Failing Heart - An Engine Out of Fuel. *N Engl J Med* 356: 1140–1151, 2007.
43. **Newton JC, Smith WM, Ideker RE.** Estimated global transmural distribution of activation rate and conduction block during porcine and canine ventricular fibrillation. *Circ Res* 94: 836–842, 2004.
44. **Olasveengen TM, Samdal M, Steen PA, Wik L, Sunde K.** Progressing from initial non-shockable rhythms to a shockable rhythm is associated with improved outcome after out-of-hospital cardiac arrest. *Resuscitation* 80: 24–29, 2009.
45. **Parish DC, Dinesh Chandra KM, Dane FC.** Success changes the problem: why ventricular fibrillation is declining, why pulseless electrical activity is emerging, and what to do about it. *Resuscitation* 58: 31–35, 2003.
46. **Picard S, Rouet R, Ducouret P, Puddu PE, Flais F, Criniti A, Monti F, Gerard JL.** KATP channels and "border zone": arrhythmias: role of the repolarization dispersion between normal and ischaemic ventricular regions. *Br J Pharmacol* 127: 1687–1695, 1999.
47. **Poelzing S, Akar FG, Baron E, Rosenbaum DS.** Heterogeneous connexin43 expression produces electrophysiological heterogeneities across ventricular wall. *Am J Physiol Heart Circ Physiol* 286: H2001–H2009, 2004.
48. **Polentini MS, Pirrallo RG, McGill W.** The changing incidence of ventricular fibrillation in Milwaukee, Wisconsin (1992–2002). *Prehosp Emerg Care* 10: 52–60, 2006.
49. **Robertson PG, Huang J, Chen KA, Chen X, Dosdall DJ, Tabereaux PB, Smith WM, Ideker RE.** Increased cycle length during long-duration ventricular fibrillation is caused by decreased upstroke velocity as well as prolonged refractoriness. *Heart Rhythm* 6: 378–384, 2009.
50. **Rogers JM, Melnick SB, Huang J.** Fiberglass needle electrodes for transmural cardiac mapping. *IEEE Trans Biomed Eng* 49: 1639–1641. 2002.
51. **Rosati B, Rocchetti M, Zaza A, Wanke E.** Sulfonylureas blockade of neural and cardiac HERG channels. *FEBS Lett* 440: 125–130, 1998.
52. **Roth R, Stewart RD, Rogers K, Cannon GM.** Out-of-hospital cardiac arrest: factors associated with survival. *Ann Emerg Med* 13: 237–243, 1984.
53. **Schaffer P, Pelzmann B, Bernhart E, Lang P, Mächler H, Rigler B, Koidl B.** The sulphonylurea glibenclamide inhibits voltage dependent potassium currents in human atrial and ventricular myocytes. *Br J Pharmacol* 128: 1175–1180, 1999.
54. **Schneider T, Martens PR, Paschen H, Kuisma M, Wolcke B, Gliner BE, Russell JK, Weaver WD, Bossaert L, Chamberlain D.** Multicenter, randomized, controlled trial of 150-j biphasic shocks compared with 200- to 360-j monophasic shocks in the resuscitation of out-of-hospital cardiac arrest victims. *Circulation* 102: 1780–1787, 2000.
55. **Shaw RM, Rudy Y.** Electrophysiologic effects of acute myocardial ischemia. A mechanistic investigation of action potential conduction and conduction failure. *Circ Res* 80: 124–138, 1997.
56. **Tabereaux PB, Walcott GP, Rogers JM, Kim J, Dosdall DJ, Robertson PG, Killingsworth CR, Smith WM, Ideker RE.** Activation patterns of Purkinje fibers during long-duration ventricular fibrillation in an isolated canine heart model. *Circulation* 116: 1113–1119, 2007.
57. **Taccardi B, Punske BB, Macchi E, Macleod RS, Ershler PR.** Epicardial and intramural excitation during ventricular pacing: effect of myocardial structure. *Am J Physiol Heart Circ Physiol* 294: H1753–H1766, 2008.
58. **Tang W, Weil MH, Sun S, Pernat A, Mason E.** KATP channel activation reduces the severity of postresuscitation myocardial dysfunction. *Am J Physiol Heart Circ Physiol* 279: H1609–H1615, 2000.
59. **Tsuji Y, Opthof T, Kamiya K, Yasui K, Liu W, Lu Z, Kodama I.** Pacing-induced heart failure causes a reduction of delayed rectifier potassium currents along with decreases in calcium and transient outward currents in rabbit ventricle. *Cardiovasc Res* 48: 300–309, 2000.
60. **Van Wagoner DR.** Mechanosensitive gating of atrial ATP-sensitive potassium channels. *Circ Res* 72: 973–983, 1993.
61. **Van Wagoner DR, Lamorgese M.** Ischemia potentiates the mechanosensitive modulation of atrial ATP-sensitive potassium channels. *Ann NY Acad Sci* 723: 392–395, 1994.
62. **Venable PW, Taylor TG, Shibayama J, Warren M, Zaitsev AV.** Complex structure of electrophysiological gradients emerging during long-duration ventricular fibrillation in the canine heart. *Am J Physiol Heart Circ Physiol* 299: H1405–H1418, 2010.
63. **Venkatesh N, Lamp ST, Weiss JN.** Sulfonylureas, ATP-sensitive K+ channels, and cellular K+ loss during hypoxia, ischemia, and metabolic inhibition in mammalian ventricle. *Circ Res* 69: 623–637, 1991.
64. **Vetter FJ, McCulloch AD.** Mechanoelectric feedback in a model of the passively inflated left ventricle. *Ann Biomed Eng* 29: 414–426, 2001.
65. **West PD, Bursill JA, Wyse KR, Martin DK, Campbell TJ.** Effect of Dofetilide and d-Sotalol on the ATP-Sensitive Potassium Channel of Rabbit Ventricular Myocytes. *J Cardiovasc Pharmacol Ther* 1: 307–312. 1996.

66. **Wilde AA, Escande D, Schumacher CA, Thuringer D, Mestre M, Fiolet JW, Janse MJ.** Potassium accumulation in the globally ischemic mammalian heart. A role for the ATP-sensitive potassium channel. *Circ Res* 67: 835–843, 1990.
67. **Worley SJ, Swain JL, Colavita PG, Smith WM, Ideker RE.** Development of an endocardial-epicardial gradient of activation rate during electrically induced, sustained ventricular fibrillation in dogs. *Am J Cardiol* 55: 813–820, 1985.
68. **Zaitsev AV, Guha PK, Sarmast F, Kolli A, Berenfeld O, Pertsov AM, de Groot JR, Coronel R, Jalife J.** Wavebreak formation during ventricular fibrillation in the isolated, regionally ischemic pig heart. *Circ Res* 92: 546–553, 2003.

CHAPTER 6

DETECTION OF MITOCONDRIAL DEPOLARIZATION/RECOVERY DURING ISCHAEMIA-REPERFUSION USING SPECTRAL PROPERTIES OF CONFOCALLY RECORDED TMRM FLUORESCENCE

The research in this chapter was published in the *Journal of Physiology*. Paul W. Venable, Tyson G. Taylor, Katie J. Sciuto, Jerry Zhao, Junko Shibayama, Mark Warren, Kenneth W. Spitzer, and Alexey V. Zaitsev.: 'Detection of mitochondrial depolarization/recovery during ischaemia-repufusion using spectral properties of confocally recorded TMRM fluorescence.' J Physiol, 2013 Jun 1, 591 (Pt 11), pp 2781-94. Reprinted with permission of the Journal of Physiology.

J Physiol 591.11 (2013) pp 2781–2794

TECHNIQUES FOR PHYSIOLOGY

Detection of mitochondrial depolarization/recovery during ischaemia–reperfusion using spectral properties of confocally recorded TMRM fluorescence

Paul W. Venable, Tyson G. Taylor, Katie J. Sciuto, Jerry Zhao, Junko Shibayama, Mark Warren, Kenneth W. Spitzer and Alexey V. Zaitsev

Nora Eccles Harrison Cardiovascular Research and Training Institute, University of Utah, Salt Lake City, UT, USA

Key points

- Mitochondrial inner membrane potential ($\Delta\Psi_m$) collapse during myocardial ischaemia is one of the key events determining the physiological consequences of ischaemic attack in terms of post-ischaemic arrhythmias and cell survival.
- Timing and pattern of $\Delta\Psi_m$ collapse during ischaemia remain controversial, in part due to difficulties in interpreting the fluorescence of potentiometric cationic probes commonly used for assessment of $\Delta\Psi_m$ in cellular and multicellular experimental models.
- This manuscript presents a new method for monitoring $\Delta\Psi_m$ in whole hearts based on the regular arrangement of mitochondria in cardiac myocytes, thus permitting detection of $\Delta\Psi_m$ collapse using spectral analysis of fluorescence.
- The proposed method will help to ascertain the role of mitochondrial function in acute cardiovascular conditions, such as acute myocardial infarction or sudden cardiac arrest.

Abstract Timing and pattern of mitochondrial potential ($\Delta\Psi_m$) depolarization during no-flow ischaemia–reperfusion (I–R) remain controversial, at least in part due to difficulties in interpreting the changes in the fluorescence of $\Delta\Psi_m$-sensitive dyes such as TMRM. The objective of this study was to develop a new approach for interpreting confocal TMRM signals during I–R based on spatial periodicity of mitochondrial packaging in ventricular cardiomyocytes. TMRM fluorescence (F_{TMRM}) was recorded from Langendorff-perfused rabbit hearts immobilized with blebbistatin using either a confocal microscope or an optical mapping system. The hearts were studied under normal conditions, during mitochondrial uncoupling using the protonophore FCCP, and during I–R. Confocal images of F_{TMRM} were subjected to spatial Fourier transform which revealed distinct peaks at a spatial frequency of ~2 μm^{-1}. The area under the peak (MPA) progressively decreased upon application of increasing concentrations of FCCP (0.3–20 μM), becoming undetectable at 5–20 μM FCCP. During ischaemia, a dramatic decrease in MPA, reaching the low/undetectable level comparable to that induced by 5–20 μM FCCP, was observed between 27 and 69 min of ischaemia. Upon reperfusion, a heterogeneous MPA recovery was observed, but not a *de novo* MPA decrease. Both confocal and wide-field imaging registered a consistent decrease in spatially averaged F_{TMRM} in the presence of 5 μM FCCP, but no consistent change in this parameter during I–R. We conclude that MPA derived from confocal images provides a sensitive and specific indicator of significant mitochondrial depolarization or

 DOI: 10.1113/jphysiol.2012.248153

recovery during I–R. In contrast, spatially averaged F_{TMRM} is not a reliable indicator of $\Delta\Psi_m$ changes during I–R.

(Received 7 December 2012; accepted after revision 18 March 2013; first published online 25 March 2013)
Corresponding author A. V. Zaitsev: Nora Eccles Harrison Cardiovascular Research and Training Institute, University of Utah, 95 S 2000 E, Salt Lake City, UT 84112-5000, USA. Email: zaitsev@cvrti.utah.edu

Abbreviations $\Delta\Psi_m$, mitochondrial membrane potential; FCCP, carbonylcyanide-*p*-trifluoromethoxyphenyl hydrazone (a protonophore and potent uncoupler of oxidative phosphorylation); F_{TMRM}, fluorescence of TMRM; mean F_{TMRM}, spatially averaged fluorescence of TMRM; IAA, sodium iodoacetate (an inhibitor of anaerobic glycolysis); I–R, ischaemia–reperfusion; LV, left ventricle; MPA, mitochondrial peak area; ROI, region of interest; RV, right ventricle; SD/mean of F_{TMRM}, standard deviation of TMRM fluorescence over space divided by the mean; SPT, spatial Fourier transform; TMRM, tetramethylrhodamine methyl ester (a cationic fluorescent dye).

Introduction

The dynamics of $\Delta\Psi_m$ loss and recovery during I–R have been implicated in the immediate (loss of excitability, post-ischaemic arrhythmias; Akar *et al.* 2005) and long-term (cell survival or death; Petronilli *et al.* 2001) outcomes of a regional ischaemic event due to coronary occlusion, or global ischaemia due to cardiac arrest or trauma. To date, however, most of these concepts are based on knowledge obtained in isolated mitochondria or isolated cardiomyocytes, model systems which cannot fully recapitulate all the essential features of I–R in whole hearts. In recent years, several groups started studying the dynamics of $\Delta\Psi_m$ during I–R or its surrogates in whole hearts by monitoring fluorescence emitted by the rhodamine-based cationic dyes TMRM and TMRE using either confocal microcopy (Matsumoto-Ida *et al.* 2006; Slodzinski *et al.* 2008; Kato *et al.* 2009; Davidson *et al.* 2012) or wide-field optical mapping (Jin *et al.* 2010; Lyon *et al.* 2010). Reviewing these studies, one cannot fail to notice a diversity of outcomes with regard to the timing (early (Lyon *et al.* 2010) or late (Matsumoto-Ida *et al.* 2006; Slodzinski *et al.* 2008; Kato *et al.* 2009) in ischaemia, or upon reperfusion (Matsumoto-Ida *et al.* 2006; Slodzinski *et al.* 2008; Davidson *et al.* 2012)) and spatial pattern (mosaic (Matsumoto-Ida *et al.* 2006; Slodzinski *et al.* 2008; Davidson *et al.* 2012), diffuse (Kato *et al.* 2009), or propagating as a wave (Lyon *et al.* 2010)) of delta $\Delta\Psi_m$ depolarization during I–R. Without better understanding of the actual dynamics of $\Delta\Psi_m$ during realistic I–R, it will be impossible to translate the vast amount of prior knowledge obtained in reductionist approaches to the level of integrative physiology and eventually to the level of human cardiac disease.

At least in part, the variability in results may be due to the difficulty of interpreting changes in fluorescence emitted by the dyes used to monitor $\Delta\Psi_m$ (superbly reviewed by Duchen *et al.* (2003)). In the first approximation, the cationic dyes TMRM and TMRE distribute across the extracellular space, cytosol and mitochondrial matrix based on a 3-chamber Nernstian system which is governed by both $\Delta\Psi_m$ and the sarcolemmal transmembrane potential ($\Delta\Psi_s$). This leads to the highest concentration of the dye in the most negatively charged compartment, the mitochondrial matrix. Mitochondrial depolarization causes a redistribution of the dye between the mitochondrial matrix and the cytosol, with subsequent redistribution to extracellular space. The difficulty stems from the fact that individual mitochondria in cardiac myocytes cannot be reliably resolved as separate objects, even using confocal microscopy, and therefore the event and the degree of the dye redistribution has to be assessed from spatially averaged measurements that unavoidably include contributions from compartments other than the mitochondrial matrix. In the worst-case scenario, if the total pool of dye molecules in the compartments contributing to the recorded fluorescence does not change, then $\Delta\Psi_m$ loss may not be detectable at all. Notably, during no-flow ischaemia the total pool of the fluorophores in all myocardial compartments *does remain the same*, thus the ability to detect $\Delta\Psi_m$ depolarization is critically dependent on separating the movement of the dye between mitochondria and cytosol from other redistributions, including those which might be unrelated to $\Delta\Psi_m$ dissipation.

Amid these inherent difficulties and the diversity of previous observations, we sought to develop a new approach, which would be a more reliable and sensitive index of $\Delta\Psi_m$ loss in intact ventricular myocardium during no-flow ischaemia. Here we present a method taking advantage of spectral properties of confocally recorded TMRM fluorescence (F_{TMRM}), resulting from the spatially periodic arrangement of mitochondria within ventricular myocytes. This method permits detection of redistribution of a cationic fluorophore which is highly specific to mitochondrial depolarization. We provide evidence that, in confocal imaging, the spectral method is superior to tracking the mean F_{TMRM} level or its spatial dispersion (Brennan *et al.* 2006) and, unlike the other two measures, allows detection of the *complete* $\Delta\Psi_m$ *loss* event with a high degree of certainty.

Methods

Ethical approval

All procedures involving animals were approved by the Animal Care and Use Committee of the University of Utah and complied with the National Institutes of Health *Guide for the Care and Use of Laboratory Animals* 1996.

Isolated adult rabbit ventricular myocytes

Adult ventricular myocytes were isolated from rabbit hearts ($n = 3$) by enzymatic digestion as previously described (Skolnick *et al.* 1998; Ajiro *et al.* 2011). Animals were killed by I.V. injection of 130 mg kg^{-1} sodium pentobarbital, then the excised heart was attached to an aortic cannula and perfused with solutions gassed with 100% O_2 and held at 37°C, pH 7.3. The heart was first perfused for 5 min with a 0 mM Ca^{2+} solution containing (in mM): 92.0 NaCl, 4.4 KCl, 11.0 dextrose, 5.0 $MgCl_2$, 20.0 taurine, 5.0 creatine, 5.0 sodium pyruvate, 1.0 NaH_2PO_4, 24.0 Hepes, and 12.5 NaOH. This was followed by 13–15 min of perfusion with the same solution containing 0.075 mg ml^{-1} collagenase P (Roche Diagnostic, Manheim, Germany), 0.05 mg ml^{-1} protease (type XIV, Sigma Chemical, St Louis, MO, USA), and 0.05 mM $CaCl_2$. The heart was then perfused for 5 min with the same solution containing no enzymes. The left ventricle was minced and shaken for 10 min, and then filtered through a nylon mesh. Cells were stored at room temperature in normal Hepes-buffered solution containing 1.1 mM $CaCl_2$. All myocytes used in this study were rod shaped, had well-defined striations, and did not spontaneously contract. Experiments were performed within 10 h of isolation.

Cells were incubated in 400 nM tetramethyl rhodamine perchlorate methyl ester (TMRM) for 3–10 min at ambient temperature, placed in a perfusion chamber mounted on the stage of an inverted confocal microscope (Zeiss LSM 510, Carl Zeiss, Germany) and perfused with normal Hepes solution (126 mM NaCl, 1.0 mM $MgCl_2$, 4.4 mM KCl, 1.1 mM $CaCl_2$, 11 mM dextrose, 24 mM Hepes) at 37°C. Cells were confocally imaged using an oil-immersion 40× objective lens. F_{TMRM} was excited using a 543 nm laser and collected using a 560 long pass filter. To uncouple mitochondria and induce $\Delta\Psi_m$ depolarization, perfusion was rapidly switched to Hepes solution containing various concentrations of protonophore carbonylcyanide-*p*-trifluoromethoxyphenylhydrazone (FCCP).

Langendorff-perfused rabbit heart

Adult rabbits of either sex were killed by I.V. injection of 130 mg kg^{-1} sodium pentobarbital. Hearts were removed and attached to the Langendorff apparatus in less than 3 min. Hearts were perfused with Tyrode's solution (130 mM NaCl, 24 mM $NaHCO_3$, 1.2 mM NaH_2PO_4, 1.0 mM $MgCl_2$, 5.6 mM glucose, 4.0 mM KCl, 1.8 mM $CaCl_2$ and 0.1 g l^{-1} albumin) at a fixed rate of 30 ml min^{-1}. After an equilibration period of 35 min the heart was perfused with Tyrode's solution containing TMRM (450 nM) and the electromechanical uncoupler blebbistatin (5.7 μM, Sigma-Aldrich, St Louis, USA; Fedorov *et al.* 2007) for 30 min, unless stated otherwise. For the remainder of the experiment, hearts were perfused with Tyrode's solution containing blebbistatin. In some experiments the mitochondrial uncoupler FCCP (5 μM) and an inhibitor of glycolysis, sodium iodoacetate (15 mM), were added to the perfusate. Global ischaemia was initiated by cessation of aortic perfusion and maintained for at least 60 min, followed by reperfusion. Volume-conducted ECG was monitored continuously throughout the protocol. A bipolar pacing electrode was inserted into the depth of the left ventricular (LV) anterio-basal free wall and the pacing threshold was periodically measured throughout the experiment.

Confocal imaging in the whole heart

Langendorff-perfused hearts ($n = 12$) were placed in a custom confocal imaging chamber (Supplemental Fig. 1). Temperature was monitored in the right ventricular (RV) chamber and near the imaged epicardial area and was maintained in both sites at 37.7 ± 0.5°C throughout the experimental protocol. During ischaemia the temperature was maintained by the combined action of superfusion with Tyrode's solution bypassed from the aortic cannula and inflow of warm moisturized air into the imaging chamber (see Supplemental Fig. 1). The posterior LV epicardial surface was imaged in a line scan mode using a Zeiss LSM 510 confocal microscope with a 20× objective lens, giving a field of view of 450 μm × 450 μm, with resolution of 0.439 μm per pixel. The slice thickness was 2.7 μm. When z-stacks were obtained, 9 to 14 slices were taken at the distance of 2.7 μm between the centres of each slice. TMRM was excited using a 543 nm laser; emission was collected using a 560 nm long pass filter. The laser power and detector gain was adjusted to ensure the TMRM signal was not saturated. The mean TMRM fluorescence (F_{TMRM}) was calculated after applying manual masking to exclude grossly areas not containing solid sheets of myocardial cells. The identification and quantification of mitochondrial spectral peaks was performed using the Fourier transform function available in ImageJ and custom software routines as described in the Results.

Wide-field optical mapping in the whole heart

Hearts ($n = 11$) were fully immersed in a superfusion solution inside the imaging chamber to maintain the

temperature at 37°C both during normoxic perfusion and no-flow ischaemia. During no-flow ischaemia the superfusion was switched to a hypoxic solution gassed with 95% N_2–5% CO_2. TMRM was excited by a 532 nm solid-state laser (Coherent, Santa Clara, CA, USA). Emitted fluorescence was collected by an EMCCD camera (iXon DU-860D, Andor Technology, Belfast, UK) using a 600 ± 40 nm bandpass filter. The imaging area was 3 cm × 3 cm encompassing the entire posterior view of the right and left ventricles (see Supplemental Fig. 8). Wide-field images were analysed using Scroll (Sergey Mironov, Center for Arrhythmia Research, University of Michigan, USA) after a careful manual selection of the area exclusive to RV and LV in each heart. The details of different measurements applied to the wide-field TMRM images are described in Results.

Results

Spectral analysis and MPA computation

The idea of using spectral analysis to track mitochondrial polarization was suggested by a highly regular, 'crystal-like' pattern of mitochondrial arrangement in ventricular myocytes, such that individual mitochondria usually span a sarcomere (Vendelin *et al.* 2005). Thus, fluorescence emitted by dyes preferentially accumulating in mitochondria might reflect the highly periodic spacing of the z-disks. We first validated this idea in isolated cells. Figure 1 shows TMRM fluorescence and transmitted light images of an isolated ventricular cardiomyocyte taken in the absence (panels *Aa* and *Ac*) and in the presence (panels *Ab* and *Ad*) of the mitochondrial uncoupler FCCP (20 μM). The high concentration of the uncoupler was chosen to ensure complete dissipation of $\Delta\Psi_m$. Indeed, one can see that the brightness of F_{TMRM} is greatly reduced in the presence of FCCP (Fig. 1*Ab*), as is expected due to redistribution between mitochondrial matrix, cytosol and the (virtually infinite) perfusion bath. In addition, the spatial pattern of F_{TMRM} image is dramatically altered. Specifically, the 'granularity' apparent in the control image (Fig. 1*Aa*) is completely lost in the presence of FCCP (Fig. 1*Ab*). A zoomed-in fluorescent image of the cardiomyocyte (Fig. 1*B*) shows an example of regular mitochondrial arrangement (with a period of ~2 μm, see red arrows in Fig. 1*Ba*) along the longitudinal axis of the cell, which is abolished by application of FCCP (Fig. 1*Bb*). Such periodic features, even those not obvious by eye, can be revealed by spectral analysis.

Figure 1*Ca–d* shows spatial Fourier transformations (SFTs) of the images shown in Fig. 1*Aa–d*, respectively. By convention, the SFT spectra are displayed in polar coordinates, where the distance from the centre (radius) represents the size of periodic features and the angle represents the orientation of the features (see Supplemental Fig. 2). Note that *in the absence of FCCP* the SFT spectra of both the F_{TMRM} and transmitted light images (Fig. 1*Ca* and *c*) show distinct bands (see red arrows) at the radius corresponding to a spacing interval of ~2 μm and at the angle corresponding to the longitudinal axis of the cell (see yellow dashed line). *In the presence of FCCP*, however, the bands corresponding to spacing interval of ~2 μm are visible only in the SFT spectrum of the transmitted light image (Fig. 1*Cd*), but are absent in the SFT spectrum of F_{TMRM} image (Fig. 1*Cb*). These observations suggest that the periodic features imposed by structure (presumably z-disks) are not affected by FCCP, whereas the periodic fluctuations of TMRM concentration along the longitudinal axis of the cell have dissipated.

Figure 2 shows that the essential spectral features observed in single myocytes are fully present in the spectrum of a F_{TMRM} image obtained from a whole heart (Fig. 2*A*). In particular, the bands corresponding to spatial intervals of ~2 μm and aligned with the longitudinal axis of the myocytes are readily recognizable (Fig. 2*B*). We will refer to these bands/peaks as 'mitochondrial peaks'. In order to quantify the magnitude of these peaks we developed an algorithm illustrated in Fig. 2. Angles from 0 to π rad were scanned at small angular increments. At each angle Θ, the spectral power within the sector centred at Θ and having a user-defined angular half-width (ΔΘ) was computed as the function of radius (r) and normalized to the arc length. Due to two-fold rotational symmetry of the SFT spectrum, the same calculation was performed for the sector centred at the angle of Θ + π rad (see the two red lines in Fig. 2*B*) and the results were added at each value of r. At the angle Θ approximately corresponding to the longitudinal axis of the myocytes (Θ_{LONG}), the resulting one-dimensional spectral profile showed a well-defined mitochondrial peak and sometimes its first harmonic (see Fig. 2*C*). In order to assess, at least semi-quantitatively, the degree of mitochondrial polarization, we estimated the area under the peak. The algorithm first searched for the absolute maximum in the user-defined search range. This range should be based on the expected range of variation of the sarcomere length, which should be quite narrow for any particular species and experimental model. We found, however, that the position of the mitochondrial peak is different between isolated cardiomyocytes (~1.95 μm cycle^{-1}), normoxemic ventricular tissue (~2.4 μm cycle^{-1}) and ischaemic ventricular tissue (~2.0 μm cycle^{-1}) (see Supplemental Figs 3 and 5). When the maximum was found, the background-subtracted area within the user-defined half-width on each side of the peak (red arrowheads in Fig. 2*C*) was computed yielding MPA (green area in Fig. 2*C*). The algorithm selected the highest MPA values among all scanned angles Θ. Whenever mitochondrial peaks were detectable, the highest MPA value was always found at the angle approximately

corresponding to Θ_{axis}. However, when mitochondrial peaks were not present (due to $\Delta\Psi_m$ dissipation), the algorithm could yield a low MPA value picked at a random angle and a random spatial frequency. Such cases are easily identifiable upon close inspection and can be classified as 'non-detectable'. Alternatively, the false-detected peaks can be tolerated, or MPA can be re-measured at a fixed, user-defined Θ and spatial frequency. In our experience, the choice among these options did not affect the principal conclusion of a significant $\Delta\Psi_m$ loss. The values of input parameters used in this study are shown in Supplemental Table 1.

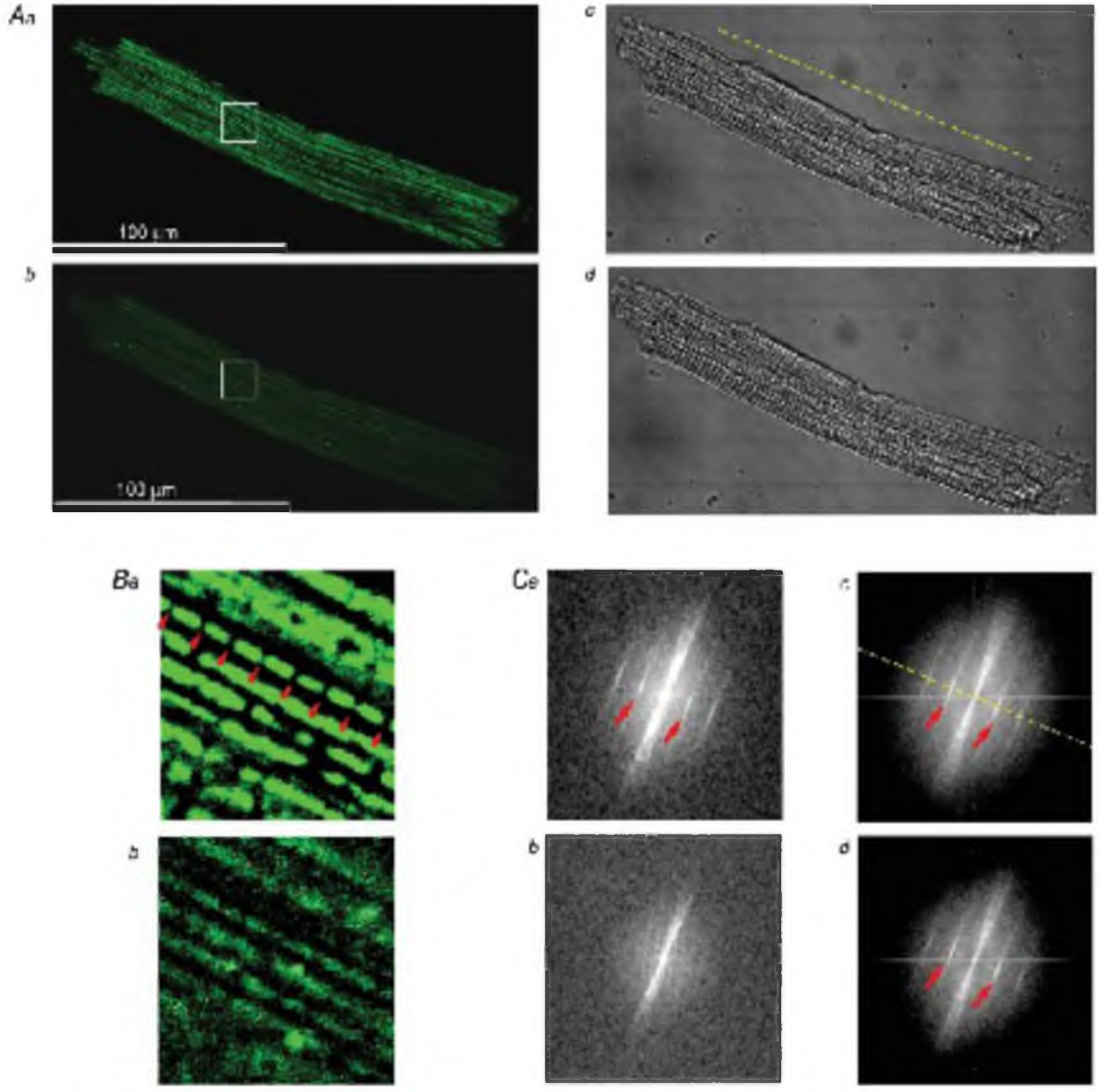

Figure 1. Spatial Fourier transform (SFT) reveals $\Delta\Psi_m$-dependent spatial periodicity in confocal images of F_{TMRM}

Aa and *b*, F_{TMRM} image of a single ventricular cardiomyocyte before and after, respectively, administration of 20 µM FCCP. *Ac* and *d*, transmitted light images corresponding to those shown in *Aa* and *b*, respectively. *Ba* and *b*, zoomed-in region of interests indicated by the white square in *Aa* and *b*, respectively. Note the presence of a highly periodic array of mitochondria at baseline spaced at ~2 µm (red arrows in *Ba*) and lack thereof after application of FCCP (*Bb*). *Ca–d*, SFT spectra of images shown in *Aa–d*, respectively. The spectral peaks (red arrows) in *Ca*, *Cc*, and *Cd* correspond to the spatial period of ~2 µm. The fact that after mitochondrial uncoupling by FCCP these peaks are absent in the SFT of the F_{TMRM} image (*Cb*), but are preserved in the SFT of the transmitted light image (*Cd*) suggests that these peaks are specific to TMRM accumulation in charged mitochondria. Yellow dashed line, the longitudinal axis of the myocyte.

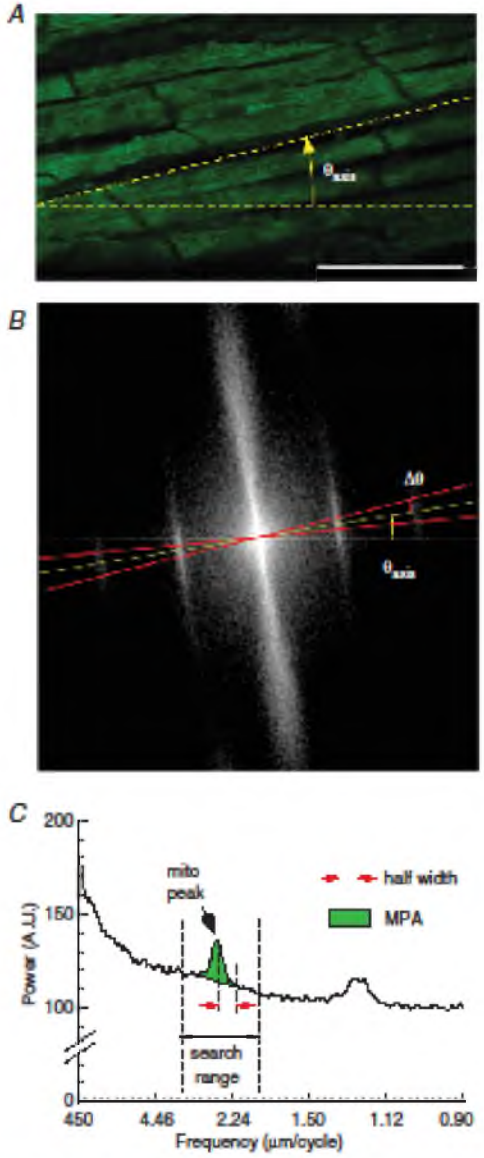

Figure 2. Spectral analysis of F_{TMRM} in confocal images obtained from subepicardial ventricular myocytes in intact heart

A, F_{TMRM} image. Θ_{axis}, the angle of the longitudinal axis of the myocytes. *B*, SFT of the image shown in *A*. $\Delta\Theta$, the half-angular width of the sector (red lines) centred at Θ_{axis} and used for computing the linear spectral profile shown in *C*. *C*, the spectral profile obtained from the SFT spectrum shown in *B*. The *x* axis is the size of spatial features, from the largest (450 μm) to the smallest (0.9 μm). The profile reveals the mitochondrial peak and its first harmonic. The position of the mitochondrial peak is at 2.4 μm cycle^{-1} with corresponds to the sarcomere length. The algorithm searched for the maximum in the user-defined search range and then computed the area under the peak within a user-defined half-width, subtracting the background level. MPA, mitochondrial peak area.

Sensitivity of MPA, mean F_{TMRM}, and SD/mean of F_{TMRM} to mitochondrial uncoupling by FCCP

In the past, either mean F_{TMRM} or standard deviation of F_{TMRM} divided by the mean (SD/mean of F_{TMRM}, a measure of spatial heterogeneity; Duchen *et al.* 2003; Brennan *et al.* 2006) were used for tracking changes in $\Delta\Psi_m$. In order to compare MPA to these other metrics, we first had to ensure stability of these parameters at baseline conditions. Supplemental Fig. 3 shows that even during long perfusion with TMRM (of the order of 1 h), mean F_{TMRM} did not reach steady state and kept increasing. In contrast, after TMRM washout all three parameters were reasonably stable (see Supplemental Fig. 4), even though MPA and SD/mean of F_{TMRM} typically fluctuated more than mean F_{TMRM}.

Figure 3 shows results from an experiment in which the response of MPA to mitochondrial uncoupling by FCCP was compared to that of mean F_{TMRM} and SD/mean of F_{TMRM}. The three parameters were measured as functions of FCCP concentration, laser power, and the size of the region of interest (ROI). The top row in Fig. 3*A* shows the full image under control conditions and indicates how the large ROI and the small ROI were selected from the full image. The small ROI roughly encompassed just two myocytes. Note that for the purposes of computing MPA for ROIs, the black peripheral areas were included in the image in order to preserve the spatial frequency resolution. The bottom row in Fig. 3*A* shows the full image recorded at different FCCP concentrations. All images shown in Fig. 3*A* were obtained at a laser power of 0.48 mW (40% of maximum power of 1.2 mW). One can see that the brightness of the images changes very little up to an FCCP concentration of 5 μM, and then decreases dramatically at 20 μM FCCP. Figure *B–D* shows mean F_{TMRM}, SD/mean of F_{TMRM} and MPA, respectively, for different FCCP concentrations and ROIs. There were slight differences between measurements of the same parameter in different ROIs, reflecting local heterogeneities in the image features. Note, however, the principally different response to increasing levels of mitochondrial uncoupling between mean F_{TMRM}, SD/mean F_{TMRM}, and MPA. In agreement with visual perception of images shown in Fig. 3*A*, mean F_{TMRM} changed very little, at most by 10%, at FCCP concentrations up to 5 μM and then dropped abruptly to an almost background level at 20 μM FCCP (see Fig. 3*B*). SD/mean of F_{TMRM} exhibited a slightly higher sensitivity, with 15–20% decrease between 0 and 5 μM FCCP followed by a dramatic decrease between 5 and 20 μM FCCP (Fig. 3*C*). In contrast, the largest decrease in MPA value (40–50% depending on the ROI) occurred in response to 1 μM FCCP (Fig. 3*D*). Subsequent increases in FCCP concentrations to 5 and 20 μM caused further progressive decreases in MPA, by an additional 20–30%, approaching zero at 20 μM.

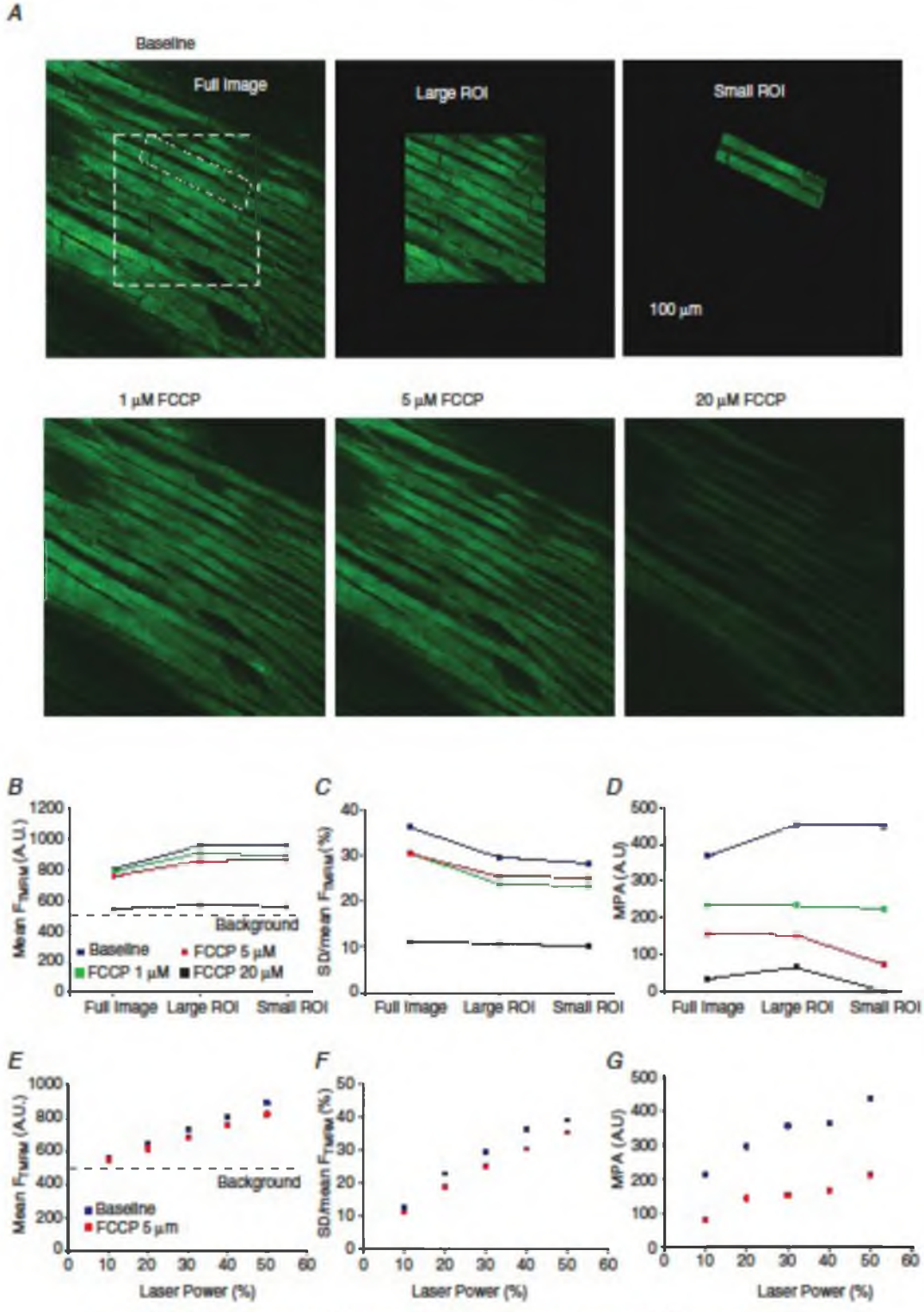

Figure 3. The dependence of MPA, mean F_{TMRM} and SD/mean F_{TMRM} on FCCP concentration, laser power, and the size of the region of interest

We also assessed how the sensitivity of mean F_{TMRM}, SD/mean F_{TMRM} and MPA to mitochondrial depolarization caused by 5 μM FCCP depends on the variation in laser power (Fig. 3*E–G*, respectively). The data are from the 'full image' (see Fig. 3*A*, top row, left image). As expected, mean F_{TMRM} linearly decreases with attenuation of laser power, approaching the threshold of detection at 10% of maximum power (see Fig. 3*E*). Note that the difference in the mean F_{TMRM} in the absence and in the presence of 5 μM FCCP is minor, and is further diminished at reduced levels of laser power. SD/mean F_{TMRM} (Fig. 3*F*) showed a slightly better sensitivity, again dependent on the laser power. However, MPA (shown in Fig. 3*G*) showed a significant improvement in sensitivity over SD/mean F_{TMRM}. Even though MPA also tended to decrease with decreasing laser power (which might be due to increasing contribution of background noise to the Fourier spectrum), the mitochondrial depolarization caused by 5 μM FCCP was still clearly detectable, even under the low-light conditions observed at the lowest laser power, due to a decrease of ~63% in the value of MPA.

Supplemental Figs 5–8 provide additional examples of FCCP effects on mean F_{TMRM} and MPA under various experimental conditions. Note that the invariable decrease of mean F_{TMRM} upon application of FCCP seen in Supplemental Figs 5, 7 and 8 rules out the presence of TMRM quenching (Duchen *et al.* 2003) in our experiments. Regarding the dose dependence of the FCCP effect, the smallest concentration of FCCP having detectable effect was between 300 nM and 1 μM, which is similar to published data (Brennan *et al.* 2006). However, even at the concentration of 5 μM we could still see residual mitochondrial peaks (see Supplemental Figs 6 and 8), suggesting the presence of residual mitochondrial polarization. The peaks were no longer visually discernible from noise when FCCP concentration was raised to 20 μM (see Supplemental Fig. 6) or when the glycolytic inhibitor iodoacetate was added after 5 μM FCCP (see Supplemental Fig. 8). Thus, it appears that a relatively high concentration of FCCP (>5 μM) is necessary to fully dissipate $\Delta\Psi_m$ and that anaerobic glycolysis might contribute to $\Delta\Psi_m$ maintenance in partially uncoupled mitochondria. Note also that, even though in isolated cells both MPA and mean F_{TMRM} responded relatively quickly to $\Delta\Psi_m$ depolarization by FCCP, in whole hearts MPA still responded fast, but mean F_{TMRM} responded very slowly (see Supplemental Fig. 8). The slower speed of TMRM loss from cells within the tissue might be due to the presence of additional diffusional barriers for TMRM in the intact heart. In summary, our data suggest that in whole hearts MPA is a more sensitive marker of mitochondrial polarization than the mean F_{TMRM} and SD/mean F_{TMRM}, and it is conceivable that the absence of mitochondrial peak (MPA ≈ 0) signifies a complete or near-complete $\Delta\Psi_m$ loss.

The dynamics of MPA, mean F_{TMRM} and SD/mean of F_{TMRM} during no-flow ischaemia

Confocal imaging during ischaemia–reperfusion was seriously confounded by massive changes in the heart shape, which invariably occurred upon the onsets of both ischaemia and reperfusion (see Fig. 5 below and Supplemental Fig. 9). Therefore, it was virtually impossible to keep the same field of view throughout the entire ischaemia–reperfusion protocol. We lost the pre-ischaemic field of view after the onset of ischaemia in seven out eight cases, and we lost the ischaemic field of view after the onset of reperfusion in eight out of eight cases. In none of the experiments were we able to maintain the same field of view throughout the entire ischaemia–reperfusion protocol. The average duration of blind periods were 8.1 ± 1.9 min and 4.6 ± 3.2 min upon the onset of ischaemia and resumption of flow, respectively.

Despite these limitations, the MPA analysis enabled us to extract definitive information about the dynamics of $\Delta\Psi_m$ depolarization and recovery during ischaemia–reperfusion. Figure 4 shows an example of confocal imaging of F_{TMRM} before, during, and after a 70 min episode of no-flow ischaemia. The plots in Fig. 4*A* shows the time course of MPA (green), mean F_{TMRM} (blue), and SD/mean F_{TMRM} (light blue). The gaps in the curves indicate changes in the field of view upon both the start of ischaemia and the start of reperfusion, and the 'blind periods' during which no stable images could be obtained. Figure 4*Ba–f* shows the spectral profiles and mitochondrial peaks at the respective time points *a–f* indicated in panel *A*. Before ischaemia, a robust mitochondrial peak can be seen in the SFT spectrum (see Fig. 4*Ba*). The field of view was re-established after

Figure 3. *A*, confocal images of F_{TMRM}. Top row, left to right: three different areas (full image, large ROI and small ROI) in which the parameters were calculated. Bottom row, left to right: full image at 1, 5 and 20 μM FCCP. At each FCCP concentration, the parameters of TMRM fluorescence were calculated for the full image and the two ROIs. *B–D*, mean F_{TMRM}, SD/mean F_{TMRM} and MPA, respectively, computed for the full image and the two ROIs in the absence and the presence of FCCP (1, 5 and 20 μM). *E–G*, mean F_{TMRM}, SD/mean F_{TMRM} and MPA, respectively, computed for the full image in the absence and in the presence of FCCP (5 μM) as the function of laser power.

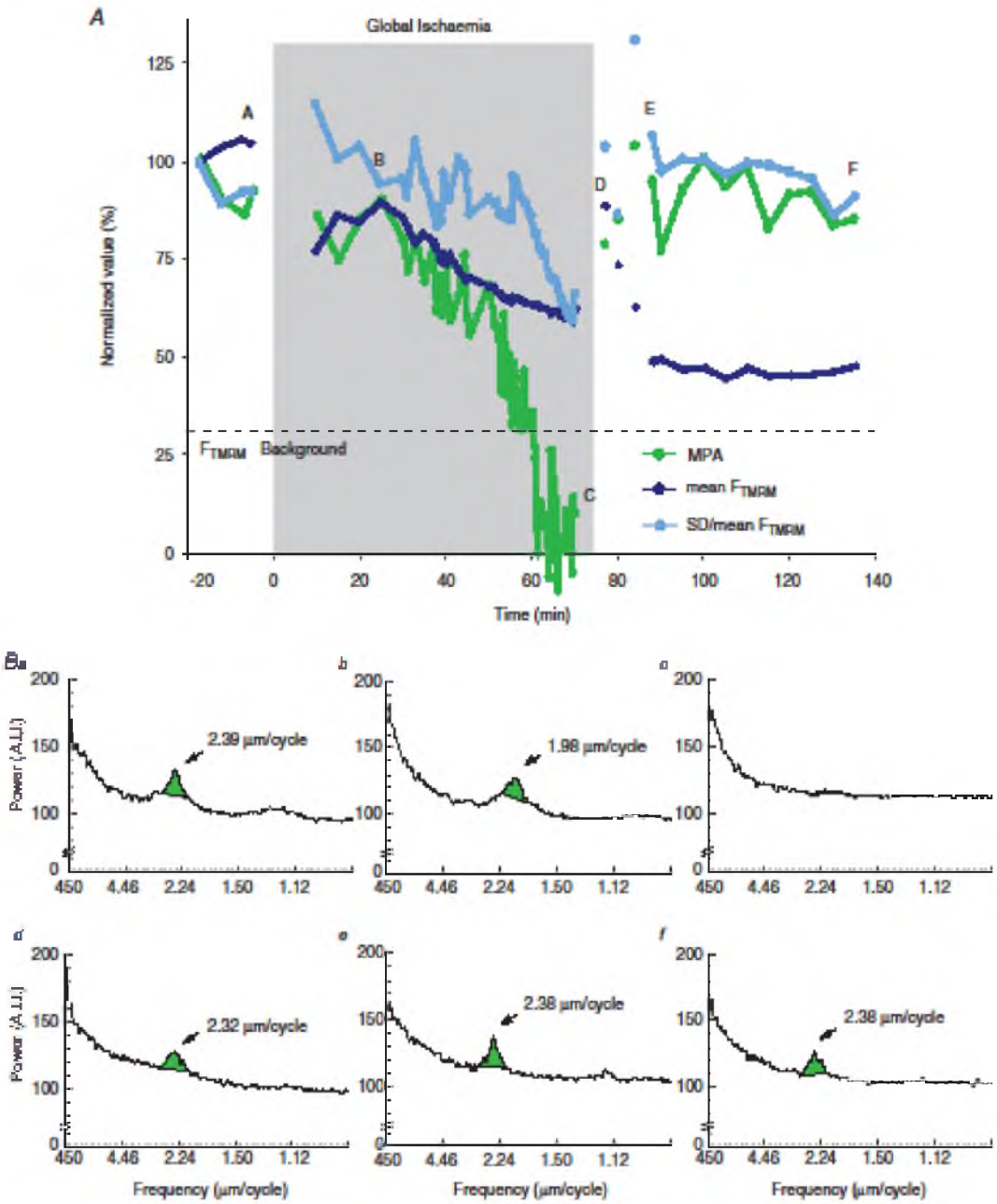

Figure 4. The dynamics of MPA, mean F_{TMRM} and SD/mean F_{TMRM} F_{TMRM} during global ischaemia and reperfusion

A, the plots of MPA (green), mean F_{TMRM} (blue) and SD/mean F_{TMRM} (light blue) before, during and after 70 min episode of ischaemia. Continuous curves indicate recordings from the same field of view. The field of view had to be changed during early ischaemia and early reperfusion because of macroscopic changes in the heart shape. Note that MPA rapidly decreases to an undetectable level between 50 and 60 min of ischaemia and recovers to the level comparable to that before ischaemia within 5 min of reperfusion. Changes in mean F_{TMRM} and SD/mean F_{TMRM} during ischaemia–reperfusion are much less prominent and inconclusive. Panels *Ba–f* show the spectral profiles and mitochondrial peaks at the respective time points indicated in *A*. Note that the mitochondrial peak shifts to a shorter spatial period (1.98 μm cycle^{-1}) during ischaemia and returns to the pre-ischaemic position (2.38 μm cycle^{-1}) upon reperfusion.

10 min of ischaemia. Between 10 and 25 min of ischaemia the value of MPA was close to the pre-ischaemic value, despite the fact that the field of view was different. Note, however, that the position of the peak changed from 2.39 μm cycle^{-1} to 1.98 μm cycle^{-1} (compare panels *Ba* and *Bb*), which is consistent with a decrease in sarcomere length and shrinking of the heart (see Supplemental Fig. 9). After 25 min of ischaemia the MPA began to drop, a process that took about 36 min to reach the level below detectability at approximately 60 min of ischaemia (see Fig. 4*Bc*). Although mean F_{TMRM} and SD/mean F_{TMRM} also decreased during ischaemia, MPA exhibited the largest fractional decrease and, unlike mean F_{TMRM} and SD/mean F_{TMRM}, MPA dynamics enabled a definitive statement of complete or near-complete $\Delta\Psi_m$ loss at around 60 min of ischaemia.

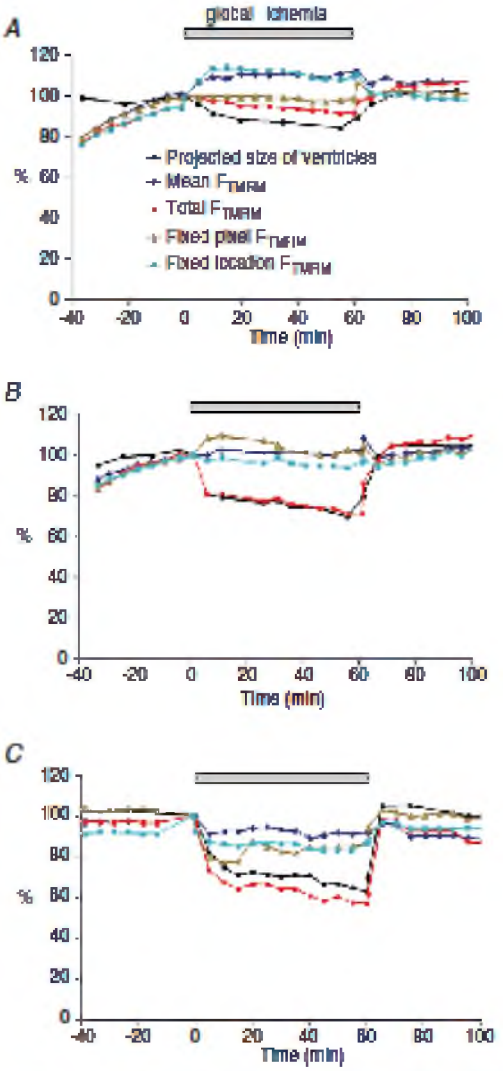

Figure 5. The dynamics of mean F_{TMRM} recorded using an optical mapping setup during global ischaemia and reperfusion

A–C, recordings obtained from 3 different hearts. The measured parameters included the projected size of the ventricles (pixel count of the mapped area), mean F_{TMRM}, total F_{TMRM}, and examples of recordings obtained from a fixed pixel (i.e. the fixed position in the CCD sensor regardless of the changes in the heart shape) and a fixed location (i.e. the same physical point on the heart surface which is projected on different pixels as the heart shape changes). Note that the total F_{TMRM} decreased in all hearts at least partially due to the decrease in the size of the ventricles. However, the dynamics of other types of F_{TMRM} measurements were in general inconsistent.

Upon reperfusion, the field of view had to be re-established four times due to the continuous expansion of the heart. The earliest reperfusion image was taken at 2 min of reperfusion (see point *d* in Fig. 4*A* and the respective spectrum in Fig. 4*Bd*) and already showed a robust recovery to near pre-ischaemic levels of all measured parameters. The second and third post-ischaemic fields of view yielded somewhat discordant fluctuations of mean F_{TMRM} and SD/mean F_{TMRM} reflecting a high dependence of these parameters on the specific features of individual fields of view. The fourth field of view was retained for another 50 min (between points *e* and *f* in Fig. 4*A*) without showing any major changes either in MPA, or mean F_{TMRM}, or SD/mean of F_{TMRM}. Note that during this time frame MPA and SD/mean of F_{TMRM} maintained highly stable levels suggestive of a maintained recovery whereas mean F_{TMRM} showed stable low level, which *per se* could be interpreted as the lack of recovery of $\Delta\Psi_m$ upon reperfusion.

In six out of seven experiments MPA exhibited a dramatic decrease during ischaemia approaching values comparable to those induced by 5–20 μM of FCCP, but only after a delay ranging between 30 and 70 min (see Supplemental Fig. 10). Thus, MPA analysis suggests a much later timing of $\Delta\Psi_m$ collapse during myocardial ischaemia than reported previously (Lyon *et al.* 2010). Sampling of MPA in multiple fields of view during reperfusion suggested spatially heterogeneous and incomplete recovery of $\Delta\Psi_m$, not entirely unexpected after these long episodes of global ischaemia (see Supplemental Fig. 10).

Cell-to-cell heterogeneities in parameters of TMRM fluorescence

Although the MPA method was mainly tested on multicellular fields of view, differences in the TMRM parameters between individual myocytes were frequently observed and could be potentially quantified in terms of mean F_{TMRM}, SD/mean F_{TMRM} and MPA. In qualitative terms, two principally different alterations of TMRM fluorescence could be observed during I–R at the level of individual cells. The first pattern, and by far the most

widespread during ischaemia, was a radical decrease in MPA amid a small (<20%) decrease in mean F_{TMRM} (see Fig. 4 above and Supplemental Figs 11 and 12). Visually such pattern was perceived as a transition from a 'granular' to a 'smooth' cell appearance, which could initially occur in individual cells and propagate as a wave (see Supplemental Video 1). MPA computed for the area exhibiting wave-like mitochondrial depolarization showed a monotonic decrease of MPA (see Supplemental Fig. 11). Thus, in essence, MPA decreased whenever any portion of the analysed region exhibited $\Delta\Psi_m$ loss.

The second pattern was an abrupt appearance of individual myocytes or small groups of myocytes exhibiting a radical decrease in both mean F_{TMRM} and MPA (see Supplemental Figs 13 and 14). Such 'dropouts' were observed in five out of eight hearts at late stages of ischaemia or during reperfusion and are probably similar to those reported previously.(Matsumoto-Ida *et al.* 2006; Slodzinski *et al.* 2008; Davidson *et al.* 2012) The abrupt and catastrophic loss of TMRM from 'dropouts' appears to be a distinct and independent phenomenon from the slow and more global decrease in MPA not accompanied by a major dye loss (see more in Discussion).

The dynamics of F_{TMRM} derived from optical mapping during mitochondrial uncoupling and I–R

Previous reports using wide-field optical mapping indicated large changes in F_{TMRM} within the first few minutes of no-flow ischaemia (Lyon *et al.* 2010), which is in apparent contradiction with the confocal data presented above. Optical mapping provides data averaged over many cells, and at a larger spatial scale (millimetres). To test the possibility that the signs of early mitochondrial depolarization can be detected at this larger scale, we investigated the dynamics of spatially averaged F_{TMRM} using a standard optical mapping technique in the same species (rabbit) and under exactly the same experimental conditions as we used in confocal experiments described above.

Whereas application of FCCP (5 μM) in normally perfused hearts induced an expected (albeit slow) decrease of mean F_{TMRM} in optical maps (see Supplemental Fig. 15), no unequivocal conclusion could be made with regard to changes in F_{TMRM} in hearts subjected to global I–R. The interpretation of these data was seriously confounded by shrinking of the heart upon the onset of ischaemia and recovery of the shape (sometimes incomplete) upon reperfusion (see Supplemental Fig. 9). Figure 5*A*–*C* shows results from three different hearts subjected to I–R. In each heart we tracked changes in the size of the ventricles (as the number of pixels covering the projected image) in parallel to changes in F_{TMRM}. Four different F_{TMRM} measurements are shown for each heart: total F_{TMRM} (fluorescence integrated over the mapped area); mean F_{TMRM} (total F_{TMRM} divided by the pixel count); fixed pixel F_{TMRM} (fluorescence recorded from a single pixel with fixed coordinates) and fixed location F_{TMRM} (our best effort to track fluorescence coming from the same physical point on the surface of the heart, based on anatomical landmarks). One can see that the total F_{TMRM} decreased during ischaemia, closely following the decrease in the projected surface area. At the same time, the mean F_{TMRM} did not show any consistent change. Likewise, measurements from a 'fixed pixel' and even 'fixed location' could show either an increase or a decrease during ischaemia. Amid these inconsistent outcomes, we concluded that, at least in our experimental model, F_{TMRM} derived from wide-field optical mapping could not faithfully represent $\Delta\Psi_m$ changes during ischaemia.

Discussion

In this methodological study we developed and validated a novel spectral method (the MPA method) for tracking *significant* changes in $\Delta\Psi_m$ during I–R in confocally imaged ventricular tissue. Below we will discuss the strengths and limitations of this method in comparison to other approaches, as well as general limits of our ability to image $\Delta\Psi_m$ during real ischaemia–reperfusion.

The major advantage of the MPA method is that it is highly sensitive and selective to the accumulation of the dye in the mitochondrial matrix. The method takes advantage of the mitochondrial packaging specific to cardiac myocytes, such that many (although not all) mitochondria are constrained between the *z*-disks (Vendelin *et al.* 2005). When the mitochondria are well polarized, the spatially periodic increases in F_{TMRM} corresponding to the mitochondrial arrays (see Fig. 1*Ba*) create a distinct mitochondrial peak in the spatial Fourier spectrum (see Fig. 1*Ca*). The observation that this peak fully disappears upon mitochondrial uncoupling by a high concentration of FCCP (see Fig. 1*Cb*) provides strong evidence that *the absence* of the peak heralds a complete or almost complete loss of $\Delta\Psi_m$. While we cannot completely exclude the possibility that mitochondrial fusion/fission may affect the MPA value, available evidence suggests a quantitatively modest change in the mitochondrial size distribution during ischaemia in the whole heart (Ong *et al.* 2010), which can hardly explain the essentially all-or-none changes in MPA observed during I–R in our study.

To the best of our knowledge, none of the previous approaches afforded such a definitive conclusion with regard to the event of $\Delta\Psi_m$ loss. Since the MPA method relies on the specific pattern of mitochondrial packaging in sarcomeres, it is limited to myocardium and presumably skeletal muscle where mitochondrial

organization is somewhat similar (Vendelin *et al.* 2005). However, knowledge of specific shape/size constraints of mitochondria in other cell types can potentially help to develop image-processing approaches for a more mitochondria-specific interpretation of those fluorescent dyes which are present in multiple cellular compartments (Gerencsér & Adam-Vizi, 2001).

A serious obstacle for continuous assessment of MPA in the same field of view during I–R, inherent to microscopic imaging in ischaemic hearts, is the large change in the heart shape accompanying both ischaemia and reperfusion. This phenomenon effectively prevented us from tracking the same group of cells throughout the entire ischaemia–reperfusion protocol in the vast majority of hearts. It should also be noted that tissue drift (albeit at a smaller scale) usually occurred during the rapid phase of ischaemic mitochondrial depolarization (see for example Supplemental Video 1) and could also diminish our ability to make a definitive statement regarding the timing of $\Delta\Psi_m$ loss in a specific group of cells. Note also that the tissue displacement, in general, occurred not only in the plane of view but also in depth, further complicating tracking the same group of cells during relevant events. Our approach to alleviate this problem was acquiring z-stacks (10 to 15 slices, at ~3 μm steps) and then automatically selecting the slice with the largest value of MPA (other criteria of selection, including algorithms of image correlation and visual recognition of image traits, can be applied). Trade-offs of acquiring z-stacks include reduced maximal temporal resolution and increased laser exposure. A recently reported approach for automated real-time tracking/stabilization of confocal images in whole hearts (Schroeder *et al.* 2010), combined with the MPA method described here, may provide an ultimate tool for the analysis of $\Delta\Psi_m$ dynamics during I–R in whole hearts. Also, multi-photon imaging may improve the robustness of the MPA technique due to inherently sharper spatial resolution and decrease in blur, especially in deeper myocardial layers.

Another significant limitation of MPA is the lack of a simple method to calibrate MPA values in terms of actual millivolts of $\Delta\Psi_m$. Again, this limitation is shared with all prior work in perfused myocardial preparations (or in isolated cardiomyocytes, for that matter). In that regard, we presented the data of MPA titration with different concentrations of FCCP (Fig. 3 and Supplemental Fig. 4), which may serve as a semi-quantitative approach for interpretation of MPA values. A dose–response function of $\Delta\Psi_m$ *versus* [FCCP] can be obtained in a mitochondrial assay (Scaduto & Grotyohann, 1999). The validity of such calibration, however, will rely on the (rather strong) assumption that isolated mitochondria have the same sensitivity to FCCP as the mitochondria in intact myocardium. In any case, values of MPA obtained during ischaemia can be compared to those obtained in the same experimental model in the presence of FCCP. In previous studies FCCP concentrations in the micromolar range were considered to be sufficient to completely dissipate $\Delta\Psi_m$ (Johnson *et al.* 1981; Petronilli *et al.* 2001; Duchen *et al.* 2003). In our study 1 μM FCCP decreased MPA by 50%, and 5 μM FCCP brought MPA values to the level of 136 ± 21 but still did not fully eliminated mitochondrial peaks. At the end of ischaemia, we observed MPA values below 136 in all experiments (see Supplemental Fig. 10), and in some cases the mitochondrial peak was visually undetectable (comparable to the effect of 20 μM FCCP). Thus, we can conclude that during ischaemia the degree of $\Delta\Psi_m$ depolarization was comparable to, or exceeded that, of $\Delta\Psi_m$ depolarization caused by 5 μM FCCP.

It is more difficult to form conclusions regarding intermediate levels of MPA. Even during normal perfusion, the variability of MPA was quite high, ranging from 550 to 210 (see Supplemental Fig. 10). Whereas we cannot exclude heterogeneities in $\Delta\Psi_m$ at baseline, we have an impression that this variability was mostly due to variability in the quality and sharpness of the image. Note, however, that in those cases when we were able to maintain the same field of view during ischaemia, the observation of a continuous monotonic decrease in MPA provided valuable information about the timing and the speed of $\Delta\Psi_m$ loss and recovery. For example, the ischaemic data obtained in this study suggest that a significant $\Delta\Psi_m$ depolarization occurs relatively late in ischaemia (after ~30 min) and is a relatively slow process (takes at least 10–15 min), but can be essentially complete by 60–70 min of ischaemia. However, even after such a prolonged time of ischaemia, a relatively fast recovery of $\Delta\Psi_m$ could be observed upon reperfusion at least in some hearts, without evidence of massive and fatal $\Delta\Psi_m$ loss up to 1 h following reperfusion. Also, the recovery upon reperfusion appeared to be heterogeneous (see Supplemental Fig. 10).

The comparative analysis of the dynamics of MPA and mean F_{TMRM} gave us a new perspective on previous observations in the setting of I–R in whole hearts. Several prior publications were focused on the 'dropouts' – cells exhibiting 'rapid, complete, and irreversible' (Matsumoto-Ida *et al.* 2006) loss of mean F_{TMRM} during I–R (Matsumoto-Ida *et al.* 2006; Slodzinski *et al.* 2008; Davidson *et al.* 2012). We also observed accidental 'dropouts' during I–R in our experiments (see Supplemental Figs 13 and 14). The abrupt and catastrophic decline in both MPA and mean F_{TMRM} observed in 'dropouts' appears to be a distinct and independent phenomenon from the slow and global decrease in MPA (which reflected mitochondrial dye loss) amid only a minor change in mean F_{TMRM}. Why the 'dropouts' lose TMRM so quickly from the cytoplasm is not clear, but might reflect a significant loss of sarcolemmal polarization and/or integrity in addition to the loss of the

mitochondrial potential. Further studies are needed to resolve the timing and possible cause–effect relationships between critical mitochondrial and sarcolemmal events during I–R.

We should also comment on the previously published notion of 'waves of mitochondrial membrane potential collapse' occurring within the first 5 min of ischaemia (Lyon *et al.* 2010). The timing of $\Delta\Psi_m$ loss during ischaemia is relevant to explaining electrical depression and arrhythmias during early ischaemia or cardiac arrest, which might be related to mitochondrial depolarization (Akar *et al.* 2005). We have to mention that, based on our study, any conclusions regarding fluorescence changes in this very acute phase of global ischaemia are severely confounded by the attendant changes in the heart shape (see Supplemental Fig. 9). In our confocal experiments we were unable to track myocytes during this stage, but even after 10–15 min of ischaemia all the measured TMRM parameters (mean F_{TMRM}, SD/mean of F_{TMRM}, and MPA) were typically not different from those before ischaemia. At the same time, a major decrease in MPA was typically observed only after 30–40 min of ischaemia (see Supplemental Fig. 10). Moreover, performing optical mapping experiments in the same species (rabbit) and using the same experimental conditions as in our confocal experiments, we realized that the complex dynamical changes in the projection of the heart image to the imaging sensor, in the presence of inherent heterogeneities in dye distribution and illumination, makes the local estimate of F_{TMRM} dynamics dependent on a large number of unknown geometric factors. As a result, changes in per-pixel F_{TMRM} signal cannot be disentangled from changes in the heart geometry. Thus, the timing and the dynamics of $\Delta\Psi_m$ loss/recovery during I–R in whole hearts remain to be settled.

Summary and conclusions

Quantification of mitochondrial spectral peaks derived from confocal TMRM images may be the most sensitive method for tracking significant $\Delta\Psi_m$ changes during no-flow ischaemia and reperfusion in intact hearts. Using this method, we conclude that a significant $\Delta\Psi_m$ depolarization occurs no earlier than 30 min of ischaemia, and at least a partial recovery of $\Delta\Psi_m$ occurs upon reperfusion following 60+ min of ischaemia. This phenomenon is different from a catastrophic and irreversible loss of F_{TMRM} in individual myocytes ('dropouts') amid neighboring cells maintaining high F_{TMRM} level. The relationship between the two 'modes' of presumed $\Delta\Psi_m$ depolarization remains unclear. In the isolated Langendorff-perfused rabbit heart, wide-field imaging of F_{TMRM} can be used for detection of $\Delta\Psi_m$ loss in the presence of coronary perfusion, but does not provide reliable information during no-flow ischaemia and subsequent reperfusion.

References

Ajiro Y, Saegusa N, Giles WR, Stafforini DM & Spitzer KW (2011). Platelet-activating factor stimulates sodium-hydrogen exchange in ventricular myocytes. *Am J Physiol Heart Circ Physiol* **301**, H2395–H2401.

Akar FG, Aon MA, Tomaselli GF & O'Rourke B (2005). The mitochondrial origin of postischemic arrhythmias. *J Clin Invest* **115**, 3527–3535.

Brennan JP, Berry RG, Baghai M, Duchen MR & Shattock MJ (2006). FCCP is cardioprotective at concentrations that cause mitochondrial oxidation without detectable depolarisation. *Cardiovasc Res* **72**, 322–330.

Davidson SM, Yellon DM, Murphy MP & Duchen MR (2012). Slow calcium waves and redox changes precede mitochondrial permeability transition pore opening in the intact heart during hypoxia and reoxygenation. *Cardiovasc Res* **93**, 445–453.

Duchen MR, Surin A & Jacobson J (2003). Imaging mitochondrial function in intact cells. *Methods Enzymol* **361**, 353–389.

Fedorov VV, Lozinsky IT, Sosunov EA, Anyukhovsky EP, Rosen MR, Balke CW & Efimov IR (2007). Application of blebbistatin as an excitation-contraction uncoupler for electrophysiologic study of rat and rabbit hearts. *Heart Rhythm* **4**, 619–626.

Gerencsér ÁA & Adam-Vizi V (2001). Selective, high-resolution fluorescence imaging of mitochondrial Ca^{2+} concentration. *Cell Calcium* **30**, 311–321.

Jin H, Nass RD, Joudrey PJ, Lyon AR, Chemaly ER, Rapti K & Akar FG (2010). Altered spatiotemporal dynamics of the mitochondrial membrane potential in the hypertrophied heart. *Biophys J* **98**, 2063–2071.

Johnson LV, Walsh ML, Bockus BJ & Chen LB (1981). Monitoring of relative mitochondrial membrane potential in living cells by fluorescence microscopy. *J Cell Biol* **88**, 526–535.

Kato M, Akao M, Matsumoto-Ida M, Makiyama T, Iguchi M, Takeda T, Shimizu S & Kita T (2009). The targeting of cyclophilin D by RNAi as a novel cardioprotective therapy: evidence from two-photon imaging. *Cardiovasc Res* **83**, 335–344.

Lyon AR, Joudrey PJ, Jin D, Nass RD, Aon MA, O'Rourke B & Akar FG (2010). Optical imaging of mitochondrial function uncovers actively propagating waves of mitochondrial membrane potential collapse across intact heart. *J Mol Cell Cardiol* **49**, 565–575.

Matsumoto-Ida M, Akao M, Takeda T, Kato M & Kita T (2006). Real-time 2-photon imaging of mitochondrial function in perfused rat hearts subjected to ischemia/reperfusion. *Circulation* **114**, 1497–1503.

Ong S-B, Subrayan S, Lim SY, Yellon DM, Davidson SM & Hausenloy DJ (2010). Inhibiting mitochondrial fission protects the heart against ischemia/reperfusion injury. *Circulation* **121**, 2012–2022.

Petronilli V, Penzo D, Scorrano L, Bernardi P & Di Lisa F (2001). The mitochondrial permeability transition, release of cytochrome c and cell death. *J Biol Chem* **276**, 12030–12034.

Scaduto RC, Jr. & Grotyohann LW (1999). Measurement of mitochondrial membrane potential using fluorescent rhodamine derivatives. *Biophys J* **76**, 469–477.

Schroeder JL, Luger-Hamer M, Pursley R, Pohida T, Chefd'Hotel C, Kellman P & Balaban RS (2010). Short Communication: Subcellular motion compensation for minimally invasive microscopy, *in vivo*: Evidence for oxygen gradients in resting muscle. *Circ Res* **106**, 1129–1133.

Skolnick RL, Litwin SE, Barry WH & Spitzer KW (1998). Effect of ANG II on pHi, $[Ca^{2+}]_i$, and contraction in rabbit ventricular myocytes from infarcted hearts. *Am J Physiol Heart Circ Physiol* **275**, H1788–H1797.

Slodzinski MK, Aon MA & O'Rourke B (2008). Glutathione oxidation as a trigger of mitochondrial depolarization and oscillation in intact hearts. *J Mol Cell Cardiol* **45**, 650–660.

Vendelin M, Béraud N, Guerrero K, Andrienko T, Kuznetsov AV, Olivares J, Kay L & Saks VA (2005). Mitochondrial regular arrangement in muscle cells: a 'crystal-like' pattern. *Am J Physiol Cell Physiol* **288**, C757–C767.

Author contributions

Experiments described in this article were performed in the laboratory of Dr Zaitsev at the Nora Eccles Harrison Cardiovascular Research and Training Institute (CVRTI), University of Utah, Salt Lake City, Utah. The Zeiss confocal system is a shared facility at the CVRTI. The authors' contributions are as follows. Conception and design of the experiments: A.V.Z., P.W.V., K.W.S.; collection, analysis and interpretation of data: P.W.V., K.W.S., A.V.Z., M.W., J.S., K.I.S., J.Z., T.G.T.; drafting the article or revising it critically for important intellectual content: P.W.V., A.V.Z., K.W.S., T.G.T. All authors read and approved the final version of the manuscript.

Acknowledgements

The critical contributions of Dennis King, Bruce Steadman and Philip Ershler (CVRTI, University of Utah) into the technical aspect of this study is greatly appreciated. This study was supported by NIH NHLBI Grants 5-R01-HL-088444, 5 R01 HL103877 and Nora Eccles Treadwell Foundation research grant (A.V.Z.), NIH NRSA fellowship 5-F32-HL-097576 (J.S.), and NIH NHLBI Grant 5R37 HL0042873-24 (K.W.S.). The authors disclose no conflict of interests.

CHAPTER 7

MITOCHONDIRAL DEPOLARIZATION AND ASYSTOLE IN THE GLOBALLY ISCHEMIC RABBIT HEART: COORDINATED RESPONSE TO INTERVENTIONS AFFECTING ENERGY BALANCE

7.1 Abstract

Mitochondrial membrane potential ($\Delta\Psi_m$) depolarization has been implicated in the loss of excitability (asystole) during global ischemia, which is relevant for the success of defibrillation and resuscitation after cardiac arrest. However, the relationship between $\Delta\Psi_m$ depolarization and asystole during no-flow ischemia remains unknown. Here we applied spatial Fourier transform to confocal images formed by fluorescence of $\Delta\Psi_m$ - sensitive fluorophore TMRM and derived spectral peaks reflecting the level of $\Delta\Psi_m$. The time of ischemic $\Delta\Psi_m$ depolarization (t_{mito_depol}) was defined as the time of 50% decrease in magnitude of these peaks. The time of asystole (t_{asys}) was determined as the time when the ventricular excitation threshold exceeded 10 times of the preischemic level and no ventricular activity was present. Untreated hearts in sinus rhythm were compared to those paced at 150 ms, those treated with myosin II ATPase inhibitor blebbistatin, and those treated with blebbistatin and the inhibitor of glycolysis iodoacetate. Blebbistatin fully abolished contraction. In the absence of blebbistatin, preischemic confocal images were

acquired during brief perfusion with 20 mM potassium, and ischemic images were obtained after the ischemic contraction failure (after 7-15 minutes of ischemia). In control, t_{mito_depol} and t_{asys} were 24.4±6.0 and 26.0±5.0 min, respectively. Tachypacing did not significantly affect either parameter. Blebbistatin dramatically delayed both t_{mito_depol} and t_{asys} (51.8±9.2 and 45.9±5.7, respectively; both $p<0.0001$ vs. control), whereas blebbistatin+iodoacetate accelerated both events (t_{mito_depol}, 12.6±2.0; t_{asys}, 6.9±0.6; both $p<0.03$ vs. control). In all groups pooled together, t_{asys} was strongly correlated with t_{mito_depol} ($R2=0.83$; $p < 0.0001$). These data may indicate a casual link between $\Delta\Psi_m$ depolarization and asystole or the mutual dependence of the two events on the critical energy depletion during ischemia. Our results strongly caution against the use of blebbistatin in cardiac imaging studies involving myocardial ischemia.

7.2 Introduction

Collapse of mitochondrial inner membrane potential ($\Delta\Psi_m$) is a major adverse event in the course of global myocardial ischemia and/or reperfusion. It has been implicated in loss of excitability during ischemia and subsequent postreperfusion VF(1), and in the development of pro-arrhythmic action potential alternans during ischemia (30). Despite the obvious importance of $\Delta\Psi_m$ loss for the outcomes of an ischemic insult, the timing and the determinants of this event are still poorly understood. One reason for that is the difficulty of monitoring $\Delta\Psi_m$ in realistic, whole-heart models of ischemia. We addressed these issues in a our previous publication (35) and developed a new method for detection of $\Delta\Psi_m$ collapse in globally ischemic hearts based on spectral analysis of confocally-derived fluorescence emitted by mitochondrial probe tetramethyl rhodamin

perchlorate methyl ester (TMRM)(35). In that study, we provided evidence that a subcellular resolution afforded by a confocal or multiphoton microscopy is necessary to detect $\Delta\Psi_m$ collapse during no-flow ischemia. This, however, necessitates complete immobilization of the heart, because otherwise the scanned microscopic images are distorted, preventing recognition of subcellular features. The recently discovered myosin II inhibitor blebbistatin (12) has been routinely used in both wide-field and confocal heart imaging studies addressing pathophysiology of myocardial I/R (30),(10). However, these studies typically lacked appropriate controls for the possible modulating effects of blebbistatin with regard to studied phenomena.

The purpose of this study was to provide experimental validation of the previously postulated cause-effect relationship between $\Delta\Psi_m$ collapse and electrical failure during ischemia (1). We reasoned that a strong correlation between the timing of $\Delta\Psi_m$ depolarization (t_{mito_depol}) and the timing of asystole (t_{asys}) during global ischemia in whoel hearts would provide a strong support, even though not a complete proof, of the postulated causal relationship. The lack of such correlation would clearly refute it. We also hypothesized that high excitation rate, a condition relevant to VF-induced cardiac arrest, might affect t_{asys}, t_{mito_depol}, or both during ischemia. The difficult, but crucially important, part of the experimental design was to estimate the confounding effects of blebbistatin, which is required to perform confocal experiments in contracting hearts. For that purpose, we transiently immobilized hearts with high potassium Tyrode's solution for obtaining baseline (preischemic) images, and performed confocal imaging during ischemia only after the hearts experienced ischemic contraction failure.

The experiments in blebbistatin-free hearts revealed, quite unexpectedly, that

blebbistatin dramatically (by approximately 100%) and proportionally increased both t_{mito_depol} and t_{asys}, whereas rapid pacing had minimal effects on these parameters. The effects of blebbistatin were fully abolished by the inhibitor of glycolysis iodoacetate, suggesting energy preservation as the underlying mechanism. Importantly, even in the absence of blebbisatin, a significant $\Delta\Psi_m$ depolarization occurred relatively late (at ~ 25 minutes of ischemia), which is much later than it was previously thought (20) and suggests that $\Delta\Psi_m$ has little or no role in early ischemic events, such as contraction failure, action potential shortening (1), and action potential alternans (30). However, under all tested conditions, there was a direct correlation between t_{asys} and t_{mito_depol}, which is compatible with a causal relationship between the two events, although it may also indicate a mutual dependence on the critical level of energy depletion. These observed "life-supporting" effects of blebbistatin urges great caution in the interpretation of ischemic studies conducted in the presence of this drug, but also underscore outstanding cardioprotective properties of blebbistatin, which might be useful in the setting of clinical ischemia/reperfusion and organ preservation.

7.3 Methods

All procedures involving animals were approved by the Animal Care and Use Committee of the University of Utah and complied with the National Institutes of Health Guide for the Care and Use of Laboratory Animals 1996.

7.3.1 Isolated heart model of SCA

Adult white New Zealand rabbits of either sex (2.3±0.5 kg) were euthanized by sodium pentobarbital (130 mg/kg, I/V). Hearts were quickly removed via midline sternotomy and attached to the Langendorff-perfusion apparatus in less than 3 minutes. Hearts were perfused with Tyrode's solution (130 mM NaCl, 24 mM NaHCO3, 1.2 NaH2PO4, 1.0 mM MgCl2, 5.6 mM Glucose, 4.0 mM KCl, 1.8 mM CaCl2, and 0.1g/L albumin, pH=7.4, temperature 37.7±1°C) at the fixed rate of 30 mL/min. After the equilibrium period of 35 minutes, hearts were perfused with Tyrode's solution containing cationic flurophore tetramethylrhodamine methyl ester (TMRM, 450 nM) for 30 minutes followed by washout with normal Tyrode's solution. Subsequent perfusion protocols depended on the experimental group as described below in detail; however, in all groups, the time interval between the heart cannulation and the onset of global ischemia was maintained close to 3 minutes.

All hearts were placed in a custom confocal imaging chamber with a coverslip built in the bottom of the chamber (35). Temperature was monitored in the right ventricular (RV) cavity and near the imaged area in the posterior left ventricular (LV) epicardial surface, and maintained at both sites at 37.7 ± 1° C throughout the protocol. A global bipolar electrogram (an analog of ECG) was recorded continuously from silver electrodes placed on bottom of the imaging chamber on the two sides of the ventricles. Additionally, a small flexible bipolar electrode was placed between the imaging cover slip and the heart from the area imaged in confocal microscope. Two bipolar pacing electrodes made of a pair of Teflon-coated silver wires were inserted into the interventricular septum and the left ventricular (LV) free wall to probe excitation

threshold and to apply rapid pacing. Outflow of the perfusate from the heart was allowed to fill the imaging chamber to the level of ~4 mm from the bottom, which helped to maintain moisture and temperature at the imaged area, and provided a current conductor for the global ECG.

Global ischemia was initiated by the cessation of aortic perfusion and maintained for at least 60 minutes, followed by reperfusion. During ischemia, temperature was maintained at 37.7 ± 1° C by resistor heaters located in the perfusion bath walls and superfusion with heated Tyrode's solution gassed with 95% N2/5% CO2. In 4 experiments, a miniature oxygen probe was inserted between the imaged area and the coverslip during ischemia to ensure hypoxic conditions at the imaged surface. Measured pO2 was <20 mmHg during ischemia.

7.3.2 Experimental groups

A total of 5 experimental groups were used in this study. Hearts in all groups were subjected to 60 minutes of global no-flow ischemia. In Control group (n=7), the hearts were not treated with any drug and were not paced until the spontaneous ventricular activity was lost later in ischemia. In Tachy group (n=5), the hearts were rapidly paced during ischemia (details below). In BBS group (n=7), the hearts were treated with myosin II ATPase inhibitor blebbistatin, which is routinely used for heart immobilization in cardiac imaging studies (12). In BBS-IA group (n=4), the hearts was treated with the combination of blebbistatin and the inhibitor of anaerobic glycolysis sodium iodoacetate. In Glyb group (n=6), the hearts was treated with ATP-sensitive potassium channel (K-ATP) blocker glybenclamide prior to ischemia. This series is supplementary and as such

is described in detail in the Data Supplement.

In Control and Tachy groups, TMRM was washed out with normal Tyrode's solution for 10 minutes. To arrest contraction and record baseline TMRM images prior to ischemia, hearts in these two groups were perfused for approximately 15 minutes with a modified high potassium Tyrode's solution in which [KCl] was raised to 20 mM and [NaCl] was reduced to 114 mM; otherwise, the composition of the solution was the same as described above. The high potassium solution was replaced with normal Tyrode's solution for 10 minutes after the return of normal sinus rhythm before the onset of global ischemia.

In Tachy group, pacing at the cycle length (CL) of 150 ms and stimulus current amplitude of 1.5 times excitation threshold was initiated immediately preceding ischemia. During ischemia, as the excitation threshold increased and one to one capture was lost, the stimulus amplitude was increased to 3 times and then to 10 times preischemic excitation threshold, and the CL was increased to 200 ms, 300 ms, and 700 ms to maintain the highest ventricular activation rate possible. In all other groups, pacing was not initiated until AV block or asystole was observed on the ECG, after which point the same pacing algorithm was used as described above but starting at the CL=300 ms (approximate cycle length of spontaneous sinus rhythm). Hearts were paced from the LV free wall location until threshold exceeded 10X baseline capture, at which point pacing was switched to the second electrode located in the interventricular septum where the same pacing algorithm was applied. The duration of tachycardic rhythm during ischemia was defined as the time during which the excitation rate was maintained at 5 Hz (CL=200 ms) or above, which included paced rhythms and ventricular tachycardia/fibrillation

induced in some hearts by rapid pacing.

In BBS and BBS-IA groups, the TMRM staining solution and all remaining Tyrode's solutions included 5.7 μM blebbistatin(+)+ (Sigma-Aldrich, St. Louis, USA). No high potassium solution was needed due to the effective abolishment of contraction by blebbistatin. The hearts in BBS-IA group were perfused with the inhibitor of glycolysis sodium iodoacetate (250 or 1000 nM, Sigma-Aldrich, St. Louis, USA) dissolved in normal Tyrode's for 15 minutes prior to the onset of ischemia.

7.3.3 Confocal imaging

The posterior LV epicardial surface was imaged in a line scan mode using a Zeiss LSM 510 confocal microscope with a 20X objective lens, giving a field of view of 450 μm x 450 μm, with resolution of 0.439 μm per pixel. The slice thickness was 2.7 μm. In the standard imaging mode, we obtained z-stacks with 9 to 14 slices taken at the distance of 2.7 μm between the centers of each slice, at time intervals of 3-5 minutes. The acquisition of one z-stack took ≈60s seconds. The shorter time intervals between z-stacks were avoided as they could cause a significant loss of TMRM signal (presumably due to TMRM bleaching) if repetitive recordings were continued over 30 minutes (not shown). Z-stacks were helpful in (1) selecting the slice with the sharpest images of synsitial myocytes and (2) tracking the same image plane amid macroscopic changes in myocardial geometry almost always occurring during ischemia (see more in Results 7.4.1). In some cases, when a fast change in the pattern of TMRM fluorescence suggesting $\Delta\Psi_m$ depolarization was evident, a continuous time-series were recorded at a fixed z-depth giving the sharpest image. In this mode, the XY scans were repeated as

soon as the previous XY scan was finished (3.4 seconds per scan). TMRM was excited using a 543 nm laser; emission was collected using a 560 nm long pass filter. The laser power and detector gain were adjusted to ensure that the TMRM signal was not saturated.

7.3.4 Data analysis

In order to identify the time of a significant mitochondrial depolarization during ischemia, we used a spectral method introduced in our previous publication (35). This method relies on the periodic arrangement of the interfibrillar mitochondria, yielding distinct ("mitochondrial") peaks in the Fourier spectrum of the TMRM fluorescence image obtained with a confocal microscope. Loss of $\Delta\Psi_m$ leads to equalization of TMRM concentration between the mitochondrial matrix and the cytosol, causing disappearance of these peaks (35). Consequently, the area under the "mitochondrial peak" (MPA) provides an index of mitochondrial polarization in ventricular myocytes (35). The time point when MPA value reached 50% level of the difference between the minimum and maximum was used as the time of ischemic $\Delta\Psi_m$ depolarization (t_{mito_depol}). This time point was linearly interpolated when necessary. The time of asystole (t_{asys}) was defined as the time point at which no spontaneous ventricular activity was observed in either global or local electrogram, and there was no response to stimulus at 10 times preischemic excitation threshold applied at both pacing locations.

7.3.5 Statistical analysis

To compare t_{mito_depol} and t_{asys} between experimental groups, we used one-way ANOVA with Newman-Keuls post-hoc test for individual pairwise comparisons. Linear

regression analysis was applied to test for correlation between t_{mito_depol} and t_{asys} in four groups (Control, Tachy, BBS, and BBS-IA) pooled together. One-sample two-tailed t-test was used to determine if the difference between t_{mito_depol} and t_{asys} in each group is significantly different from zero. All tests were performed using XLSTAT ver. 2014.1.08 (Addinsoft USA, New York, NY). Statistical significance was declared at $p < 0.05$, and all the values presented in text, tables, and figures are means ± standard deviation.

7.4 Results

The following figures are representative examples of confocally recorded TMRM fluorescence and corresponding MPA dynamics, along with time-aligned global bipolar ECG from Control, BBS, BBS-IA, Tachy, and Glyb groups. All these figures have the same layout. Panels A to C show, from left to right, the original confocal TMRM images, their Fourier power spectrum, and spectral profiles, respectively, obtained at the selected time points indicated in Panel D. The spectral profiles are computed along the approximate longitudinal axis of myocytes indicated with yellow lines in the Foutier spectra. This line crosses two "mitochondrial peaks". Because the spectra have radial symmetry, the two halves of the spectral profile and the respective "mitochondrial peaks" are summed up to yield the curves shown on the right-hand side of Panels A-C. The mitochondrial peak area (MPA) values are computed as the integral of the region indicated with green color in the spectral profiles (see more detailed description in related text). Panel D shows the time course of MPA at 3-5-minute time steps time-aligned with a global bipolar electrogram (an analog of ECG). Red and green vertical dashed lines indicate t_{asys} and t_{mito_depol}, respectively.

Note that in hearts not treated with blebbistatin (Control, Tachy, and Glyb groups), the preischemic images were obtained during a brief period of perfusion with high potassium solution (performed at 20-30 minutes before the ischemic episode) as a means to abolish motion. In these hearts, complete cessation of contraction due to the ischemic contractile failure usually set the earliest time point at which confocal imaging became possible. In addition to rhythmic contractions, macroscopic changes in the heart shape (shrinking/swelling) could render confocal imaging impossible, because the imaged area shifted significantly even during a single scan. In 6/7 hearts from Control group, the "blind" period caused by the two types of motion artifact ranged from 7 to 13 minutes. In one Control heart, the "blind" period was extended to 19 minutes due to technical problems with the microscope. In BBS group, the main source of motion artifact was the macroscopic change in heart shape, although in some cases, blebbistatin appeared to lose efficacy within the first 5-10 minutes of ischemia, leading to microscopic rhythmic contractions. In 6/7 hearts from BBS group, the "blind" period (predominantly caused by heart shape changes) ranged from 5 to 10 minutes. In one BBS heart, the "blind" period was close to 20 minutes due to technical difficulties. Despite this limitation, the earliest MPA values obtained during ischemia were not significantly different from the preischemic MPA values in both Control and BBS groups (89±23% and 86±20% of the preischemic value, respectively; p=NS). In contrast, the end-ischemic MPA values were very significantly lower than preischemic MPA values in both Control and BBS groups (11.3±3.5% and 24.8±8.7% of the preischemic value, respectively; $p<0.0001$). In summary, the confocal imaging in whole-hearts was not possible during the early phase of ischemia either in the absence or the presence of blebbistatin, but it is

unlikely that the critical $\Delta\Psi_m$ depolarization occurred during that time period.

7.4.1 Ischemic mitochondrial depolarization and asystole in Control

Figure 7.1 shows data from a representative Control experiment in which a spontaneously beating heart was subjected to 63 minutes of global ischemia. Figure 7.1A shows data obtained under normoxemic conditions 16 minutes prior to ischemia in the presence of 20 mM [K+]o. During perfusion with the high potassium solution (shown with emerald blue in Figure 7.1D) cardiac excitation and thus contraction were fully arrested. It can be seen that the TMRM fluorescence had a "granular" appearance typical of well-polarized mitochondria and yielded prominent "mitochondrial bands" in the Fourier spectrum. Accordingly, the spectral profile along the longitudinal axis of myocytes featured a large-amplitude mitochondrial peak at spatial frequency approximately corresponding to the interval between the z-disks (2.15 μm-1), as well as its first harmonic.

Figure 7.1B shows data obtained at 9 minutes of ischemia. Note that the actual imaged myocytes are not the same as in the preischemic image (see Figure 7.1A), because the heart changed shape rapidly within the first 8 minutes of ischemia and the original field of view was lost. However, the TMRM image at 9 minutes of ischemia was similar in appearance to that prior to ischemia. Likewise, the Fourier spectrum and the corresponding spectral profile (Figure 7.1B, center and right) showed large-amplitude mitochondrial peaks, yielding MPA at about 98% of the preischemic value. These data suggest that within the first 10 minutes of ischemia, the $\Delta\Psi_m$ was largely preserved. Note, however, that the position of the mitochondrial peak shifted during ischemia to a shorter

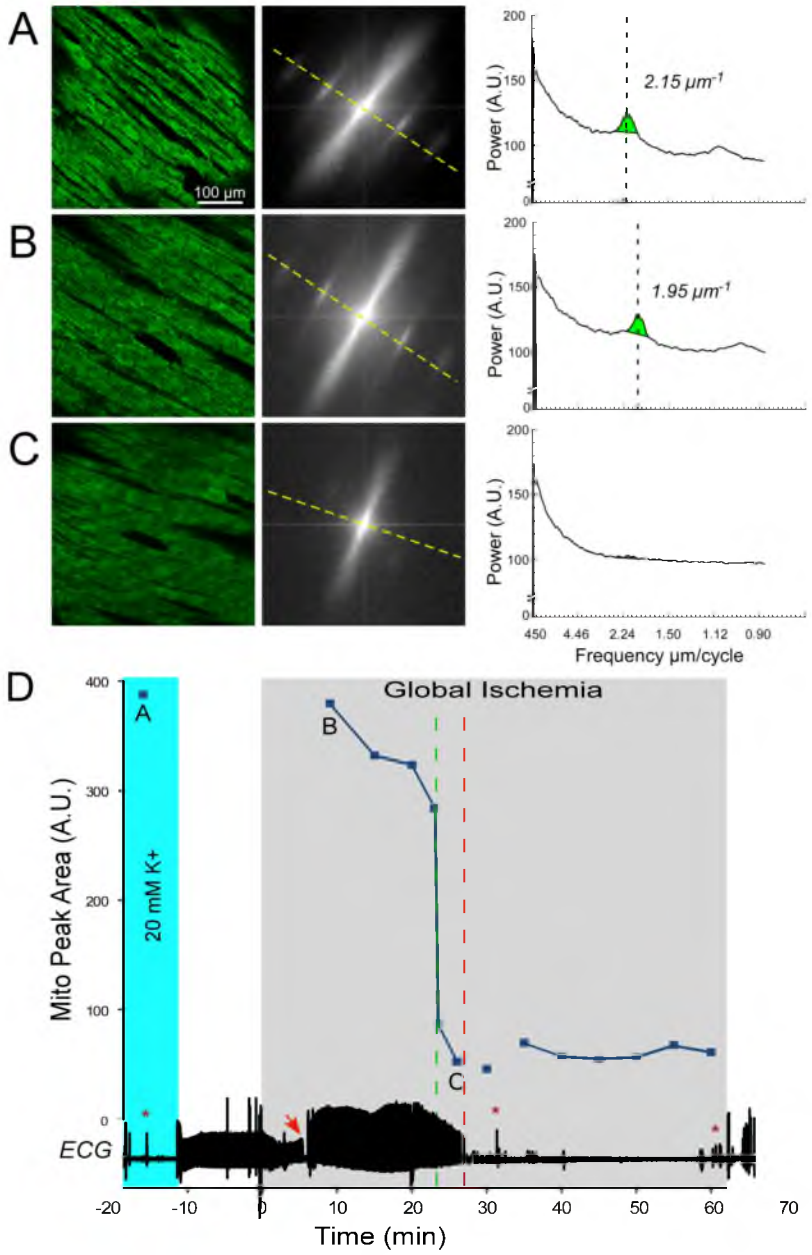

Figure 7.1. Representative data from CONTROL experiment. Panels A-C are TMRM images, SFT power spectra, and spectral profiles taken from the respective points in panel D. Panel D is MPA dynamics time aligned with ECG. Vertical dashed green line marks 50% depolarization; vertical dashed red line marks asystole time. Red arrow marks the start of pacing after loss of intrinsic ventricular activation. Asterisks mark noise induced by motion. A is during 20 mM K+ 16 minutes prior to ischemia and shows well-polarized $\Delta\Psi_m$. At B, 9 minutes of ischemia, $\Delta\Psi_m$ is still well polarized; however, significant $\Delta\Psi_m$ depolarization occurs at 23 minutes. Point C at 26 minutes of ischemia shows complete loss of $\Delta\Psi_m$. In this case, $\Delta\Psi_m$ precedes asystole at 27 minutes.

spatial period (from 2.15 μm-1 to 1.95 μm-1) reflecting shortening of the sarcomere.

MPA moderately decreased between 10 and 20 minutes, and then catastrophically decreased between 23 and 24 minutes of ischemia. The confocal TMRM image obtained after this transition (Figure 7.1C, left, corresponding to point C in Figure 7.1D) shows disappearance of the "granular" pattern, suggesting redistribution of TMRM between the mitochondrial matrix and the cytosol. Accordingly, the Fourier spectrum and the spectral profile (Figure 7.1C, center and right) reveal the virtual absence of the mitochondrial peaks. These changes strongly suggest that in this experiment, a significant $\Delta\Psi_m$ loss has occurred between 23 and 24 minutes of global ischemia ($t_{mito\_depol} = 23$). Due to additional changes in the heart shape (typically associated with rapid phases of the apparent $\Delta\Psi_m$ depolarization and the ensuing drift of the imaged area and the focal plane), the imaged area continuously imaged between time points B and C was lost. However, the two adjacent regions imaged during the rest of the ischemic period showed similar "smooth" appearance of the TMRM image and similarly low levels of MPA (not shown) suggesting that a significant $\Delta\Psi_m$ depolarization had also occurred in those regions. As mentioned before, in Control experiments, the MPA level recorded at the earliest possible time during ischemia (12.6 ± 3.8 minutes of ischemia) was not significantly different from the preischemic level. However, a decrease in MPA value to the level of at least 25% of the preischemic value was invariably observed later in ischemia. In particular, t_{mito_depol}, defined as the time of 50% MPA loss, occurred at 24.4±6.0 minutes of ischemia (range, 17.5-36.0 minutes). Ischemic MPA loss was sometimes precipitous (as in Figure 7.1D) and sometimes more gradual.

The global bipolar electrogram (an analog of ECG) recorded simultaneously with

confocal imaging is presented in the bottom of Figure 7.1D. It shows transient cessation of electrical activity caused by perfusion with high potassium solution, during which the baseline confocal image was acquired (point A). The complete AV block occurred at approximately 7 minutes of ischemia (red arrow) and was followed after a short delay with ventricular pacing. The red dashed line indicates the time at which pacing from two ventricular locations at the stimulus amplitude 10 times preischemic excitation threshold failed (t_{asys}), which in this case followed t_{mito_depol} by 4 minutes. In this and other Control hearts, asystole occurred at 26.0±5.0 minutes of ischemia (range, 17 to 33 minutes). The average time delay between t_{asys} and t_{mito_depol} (t_{asys} - t_{mito_depol}) was equal to 1.6 ±5.0 minutes and was not significantly different from zero.

7.4.2 Ischemic mitochondrial depolarization and asystole in hearts rapidly paced during ischemia (Tachy group)

Tachycardic rhythm is present in a large fraction of cases of sudden cardiac arrest. Due to increased metabolic load and increased intracellular Na and Ca, it is possible that a high excitation frequency during global ischemia affects t_{mito_depol}, t_{asys}, or the relationship between the two. Thus, in Tachy group (n=5), we applied rapid pacing (CL=150 ms) starting at 2.6± 3 minutes before ischemia and during ischemia for as long as the heart could follow this pacing rate in one-to-one fashion. As the ability to capture the heart was progressively deteriorating during ischemia, the CL and the stimulus current were progressively increased as described in Methods section 7.3.2. Rapid pacing precipitated transient episodes of ventricular tachycardia of fibrillation in 4/5 hearts with the excitation rate similar to the rate of pacing. Tachycardic rhythm (either paced rhythm

or VT/VF at CL not exceeding 200 ms) was maintained for the first 13.8±5.1 minutes of ischemia, after which time point the increasing postrepolarization refractoriness reduced the maximal rate the heart could follow. Neither t_{mito_depol} nor t_{asys} were significantly affected by the presence of tachycardic rhythm during the above-mentioned time period of early ischemia (t_{mito_depol}, 24.0±4.6 minutes; t_{asys}, 20.4±6.0 minutes; p=NS vs. Control). A representative example of confocal imaging and ECG data from Tachy group is shown in Figure 7.2.

7.4.3 Blebbistatin greatly postpones ischemic mitochondrial depolarization and asystole

Blebbistatin, a recently discovered selective inhibitor of myosin II ATPase, has become a "standard-of-care" electromechanical uncoupler for use in experimental studies involving optical mapping or confocal imaging (12), including those addressing effects of ischemia/reperfusion on electrophysiological parameters and $\Delta\Psi_m$ dynamics (10, 29, 30). However, the influence of blebbistatin on the alterations occurring during ischemia has not been thoroughly studied.

We used blebbistatin at the concentration of 5.7 μM, which in our experiments rendered contraction undetectable at the level of confocal imaging. At half of this concentration, the motion artifact became undetectable in images obtained with optical mapping system, yet was still present in confocal images (not shown). It should also be noted that in some experiments, microscopic contraction reappeared during the first 10 minutes of ischemia despite the presence of blebbistatin at the concentration of 5.7 μM, suggesting a decrease in blebbistatin efficacy under these conditions (not shown).

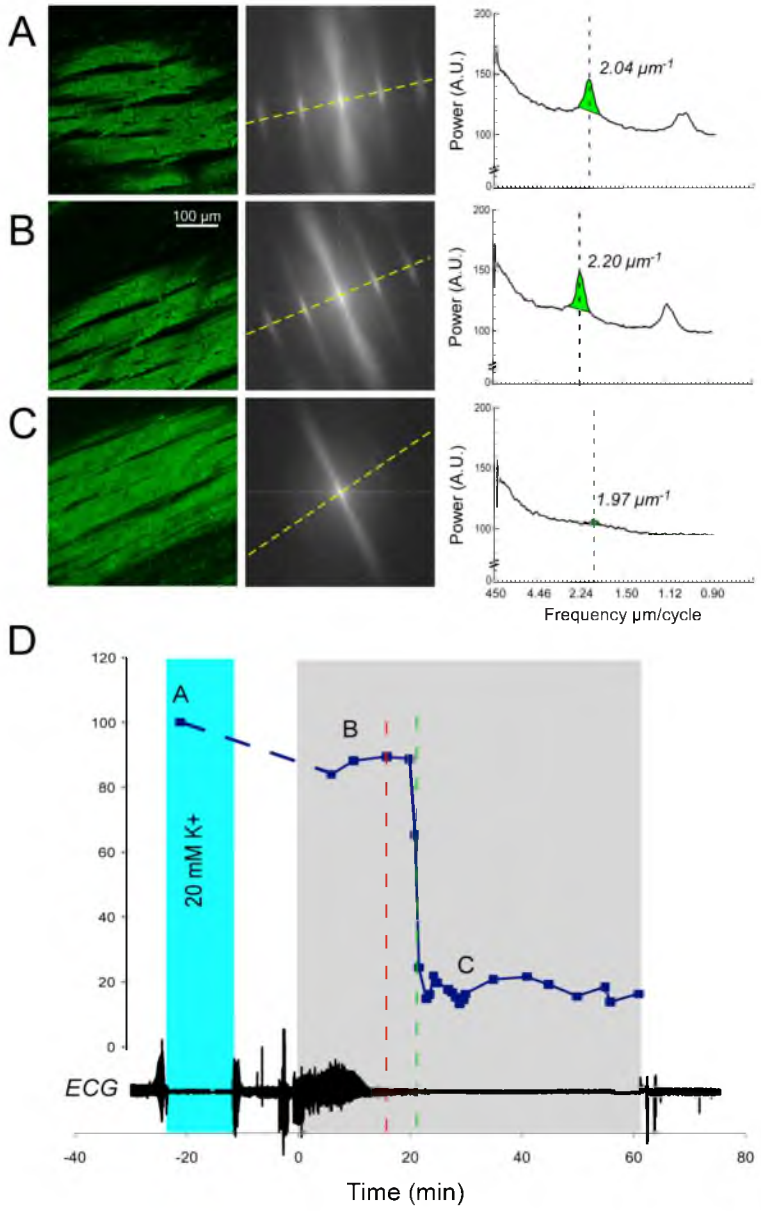

Figure 7.2. Representative data from Tachy experiment. Panels A-C are TMRM images, SFT power spectra, and spectral profiles taken from the respective points in panel D. Panel D is MPA dynamics time aligned with ECG. Vertical dashed green line marks 50% depolarization; vertical dashed red line marks asystole time. A is during 20 mM K+ 20 minutes prior to ischemia and shows well-polarized $\Delta\Psi_m$. At B, 10 minutes of ischemia, $\Delta\Psi_m$ is still well polarized; however, significant $\Delta\Psi_m$ depolarization occurs at 21 minutes of ischemia. Point C shows complete $\Delta\Psi_m$ loss at 30 minutes of ischemia. In the presence of high rate pacing, aystole occurred at 16 minutes of ischemia.

Blebbistatin had a dramatic influence on both the dynamics of $\Delta\Psi_m$ loss and the timing of asystole during ischemia. Results from a representative experiment are shown in Figure 7.3. The layout of Figure 7.3 is similar to that of Figure 7.1. Figure 7.3A shows data obtained prior to ischemia (point A in Figure 7.3D). The confocal TMRM image (Figure 7.3A, left) shows myocytes with a "granular" appearance reflecting well-polarized mitochondria. Accordingly, the spectral analysis (middle and right panel of Figure 7.3A) reveals "mitochondrial peaks". Figure 7.3B shows data obtained at 30 minutes of ischemia (point B in Figure 7.3D). It can be seen that the pattern of TMRM signal and the spectral features are similar to those obtained prior to ischemia, suggesting that mitochondrial polarization is largely preserved. Finally, Figure 7.3C shows data obtained at 70 minutes of global ischemia (point C in Figure 7.3D). At this time point, it can be seen that the granular pattern in TMRM signal is lost, as well as the "mitochondrial peaks" in the spectrum. Accordingly, the measured MPA value becomes close to zero, suggesting a very significant $\Delta\Psi_m$ depolarization.

Figure 7.3D shows the time course of MPA. One can appreciate a relatively slow (as compared to Figure 7.1) process of mitochondrial depolarization, taking about 30 minutes. MPA dynamics show minor fluctuations, which is most likely due to sensitivity of the spectral analysis to slight changes in the position of the focal plane, often unavoidable in experiments using whole-hearts. Despite these fluctuations, the overall decrease of MPA by about 90 % of the preischemic value is perhaps a robust indicator of true ischemic $\Delta\Psi_m$ loss. In this and other BBS experiments, the estimated t_{mito_depol} was 51.8±9.2 minutes of ischemia (range, 43.0-69.7 minutes), an increase of 112% over Control value ($p < 0.0001$). In the BBS group, the speed of the MPA loss appeared to be

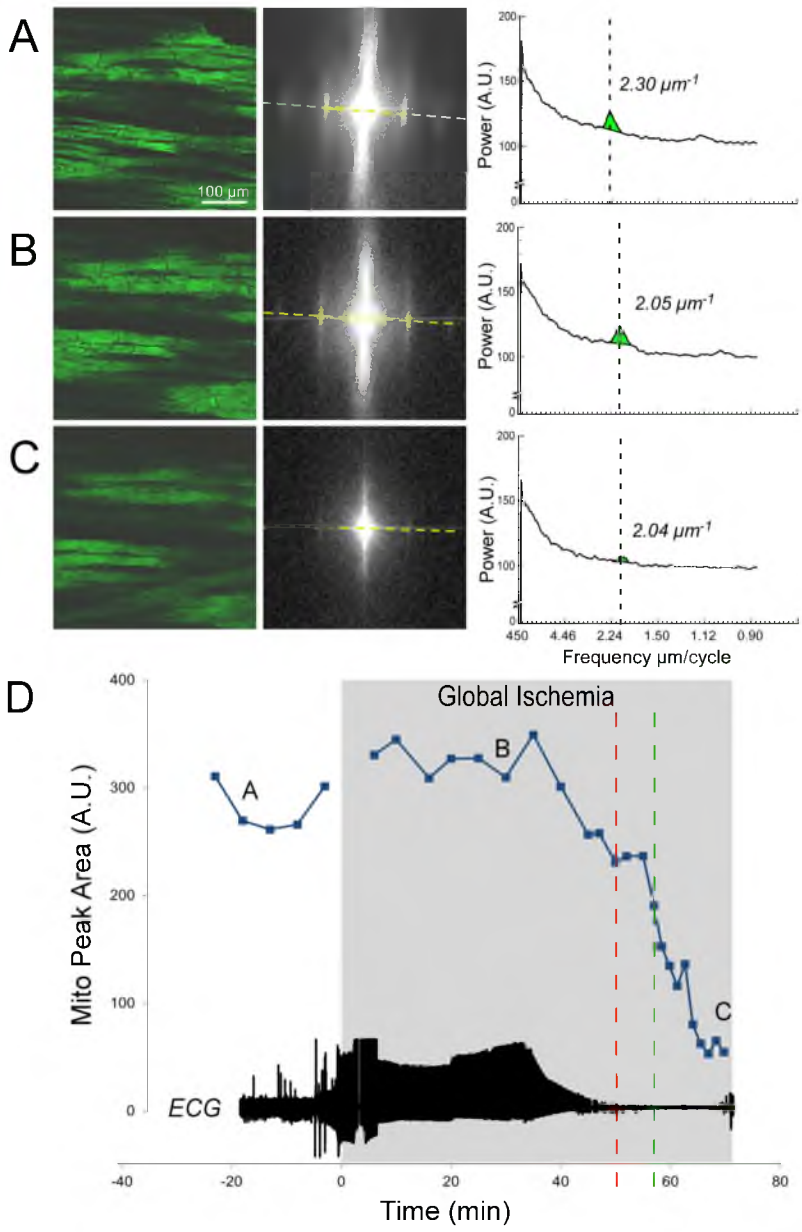

Figure 7.3. Representative data from BBS experiment. Panels A-C are TMRM images, SFT power spectra, and spectral profiles taken from the respective points in panel D. Panel D is MPA dynamics time aligned with ECG. Vertical dashed green line marks 50% depolarization; vertical dashed red line marks asystole time. A is 18 minutes prior to ischemia and shows well-polarized $\Delta\Psi_m$. At B, 30 minutes of ischemia, $\Delta\Psi_m$ is still well polarized. Significant $\Delta\Psi_m$ depolarization occurs late in ischemia at 57 minutes. Point C is after $\Delta\Psi_m$ loss at 70 minutes of ischemia. Asystole occurred at 50 minutes of ischemia, before 50% depolarization.

slower than in Control group, but it varied greatly among individual BBS experiments, and it was also difficult to convert the visual impression into a meaningful number amenable to a statistical treatment.

The global ECG is presented in the bottom of Figure 7.3D. The red dashed line indicates the time at which pacing from two ventricular locations at the stimulus amplitude 10 times preischemic excitation threshold failed (t_{asys}), which in this case preceded t_{mito_depol} by 7 minutes. Note, however, that at the time of asystole, a decrease in the MPA value was already apparent. In this and other BBS hearts, asystole occurred at 45.9±5.7 minutes of ischemia (range, 39-53 minutes). The average time delay between t_{asys} and t_{mito_depol} (t_{asys} - t_{mito_depol}) was equal to -5.9 ±7.8 minutes and was not significantly different from zero, although in 6/7 BBS experiments, asystole occurred ahead of 50%MPA loss.

7.4.4 Glycolytic inhibition greatly accelerates ischemic mitochondrial depolarization and asystole

In order to assess the role of anaerobic glycolysis in the prolonged maintenance of $\Delta\Psi_m$ and myocardial excitability during ischemia afforded by blebbistatin, four hearts were treated with an inhibitor of glycolysis sodium iodoacetate (250 – 1000 μM) in addition to blebbistatin (BBS-IA group, n=4). Figure 7.4 shows a representative example of such an experiment. Before the onset of ischemia, there were no major effects of iodoacetetae on either $\Delta\Psi_m$ or electrical activity. However, the electrical failure occurred extremely early in the course of ischemia (at 6.5 minutes of ischemia) and was shortly followed by a sharp MPA decrease, reaching the 50% level at 12.5 minutes of ischemia.

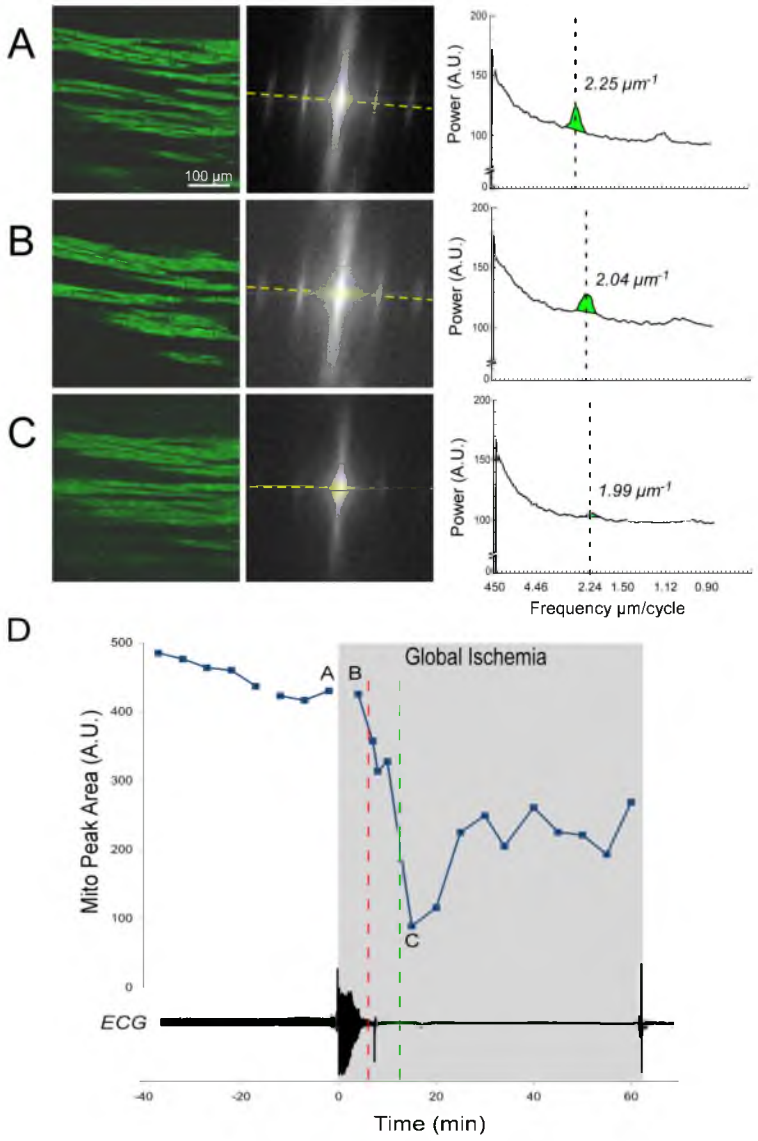

Figure 7.4. Representative data from BBS-IA experiment. Panels A-C are TMRM images, SFT power spectra, and spectral profiles taken from the respective points in panel D. Panel D is MPA dynamics time aligned with ECG. Vertical dashed green line marks 50% depolarization; vertical dashed red line marks asystole time. IA was perfused 15 minutes before ischemia, as indicated by the break in MPA plot. IA did not significantly effect $\Delta\Psi_m$, as seen at point A, 2 minutes before ischemia. At B, 4 minutes into ischemia, $\Delta\Psi_m$ is still well polarized. $\Delta\Psi_m$ depolarization occurred rapidly with 50% depolarization at 12.5 minutes. Point C is after $\Delta\Psi_m$ loss at 15 minutes of ischemia. Asystole occurred very early at 6.5 minutes of ischemia.

Of interest, the phase of sharp MPA decrease was followed by a partial recovery (observed in 3 out of 4 BBS-IA experiments), but electrical activity never recovered. It should be also noted that upon reperfusion, these hearts never recovered any electrical activity and apparently had a complete $\Delta\Psi_m$ loss within the first 10 minutes of reperfusion (not shown). In 4 BB-IA experiments, t_{asys} was 6.9±0.6 minutes and t_{mito_depol} was 12.6±2.1 minutes. Both t_{asys} and t_{mito_depol} in BBS-IA group were significantly different from the values of the respective parameters in both BBS and Control groups. Thus, it appears that the preservation of $\Delta\Psi_m$ and sarcolemmal excitability afforded by blebbistatin during ischemia is fully dependent on functional anaerobic glycolysis.

The coordinated response of t_{asys} and t_{mito_depol} to interventions affecting energy balance becomes more evident when the data from Control, Tachy, BBS, and BBS-IA groups are pooled together (Figure 7.5). One can see that overall, there is a strong direct correlation between the timing of the two critical events (R^2=0.834, $p<0.0001$) such that, on average, t_{asys} is slightly ahead of t_{mito_depol}. Note that the points from Control and Tachy groups significantly overlap, whereas the points from BBS and BBS-IA groups form distinct clusters fully separated from Control/Tachy cluster.

7.4.5 Effect of K-ATP blocker glybenclamide on ischemic mitochondrial depolarization and asystole

A cause-effect relationship between $\Delta\Psi_m$ collapse and electrical failure during ischemia mediated by a critical level of K-ATP opening has been previously postulated (1). Our observations that the time of asystole and the ischemic $\Delta\Psi_m$ loss are similar under various experimental conditions are compatible with this notion. To further

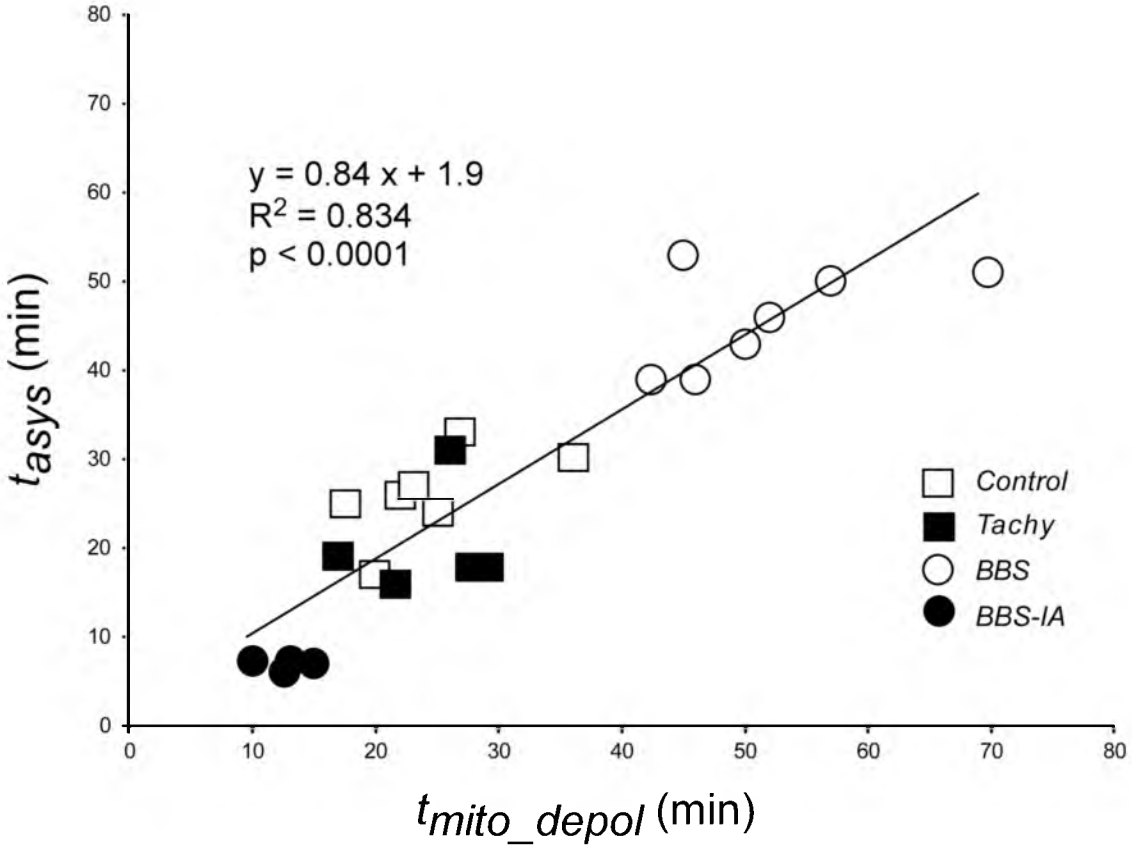

Figure 7.5. Relationship between timing of $\Delta\Psi_m$ and asystole for all interventions. $\Delta\Psi_m$ and asystole are correlated, with a slight bias toward $\Delta\Psi_m$ loss occurring after asystole. Glyb intentionally altered the relationship by moving asystole after $\Delta\Psi_m$ depolarization; therefore, Glyb experiments were not included in the linear regression plot.

ascertain the role of K-ATP in ischemic asystole, we performed experiments using K-ATP blocker glybenclamide (10 μM, Glyb group). Data from a representative heart treated with glybenclamide are shown in Figure 7.6. Glybenclamide postponed t_{asys} (to 33.6±7.7 minutes vs. 26.0±5.0 minutes in Control, $p<0.05$), confirming a role of K-ATP in ischemic electrical failure (1),(31). t_{mito_depol} in Glyb group (measured as the time of 50% MPA loss) was not different from Control (24.9±7.2 minutes vs. 24.4±6.0 minutes in Control, p=NS). However, unlike Control group, in the Glyb group the earliest possible ischemic MPA values (obtained at 12.1±1.7 minutes of ischemia) were significantly lower than the preischemic values (67.5±14.6% of preischemic value, p=0.003). In one Glyb experiment, the earliest ischemic MPA value recorded at 10 minutes of ischemia fell below 50% of the preischemic value, which necessitated the exclusion of this experiment from t_{mito_depol} analysis. Thus, it is possible that glybenclamide promoted partial $\Delta\Psi_m$ depolarization early in ischemia (see possible reasons in Discussion 7.5.1).

7.4.6 Summary of t_{asys} and t_{mito_depol} in different experimental groups

Figure 7.7 A and B summarizes the statistical analysis of t_{asys} and t_{mito_depol}, respectively, in all experimental groups. All pairwise comparisons were performed, but only physiologically meaningful significant differences are indicated. As compared to Control, t_{asys} was significantly prolonged in Glyb group, very significantly prolonged in BBS group, and very significantly shortened in BBS-IA group. Also, t_{asys} was very significantly shorter in BBS-IA group than in BBS group. As compared to Control, t_{mito_depol} was very significantly prolonged in BBS group, and significantly shortened in

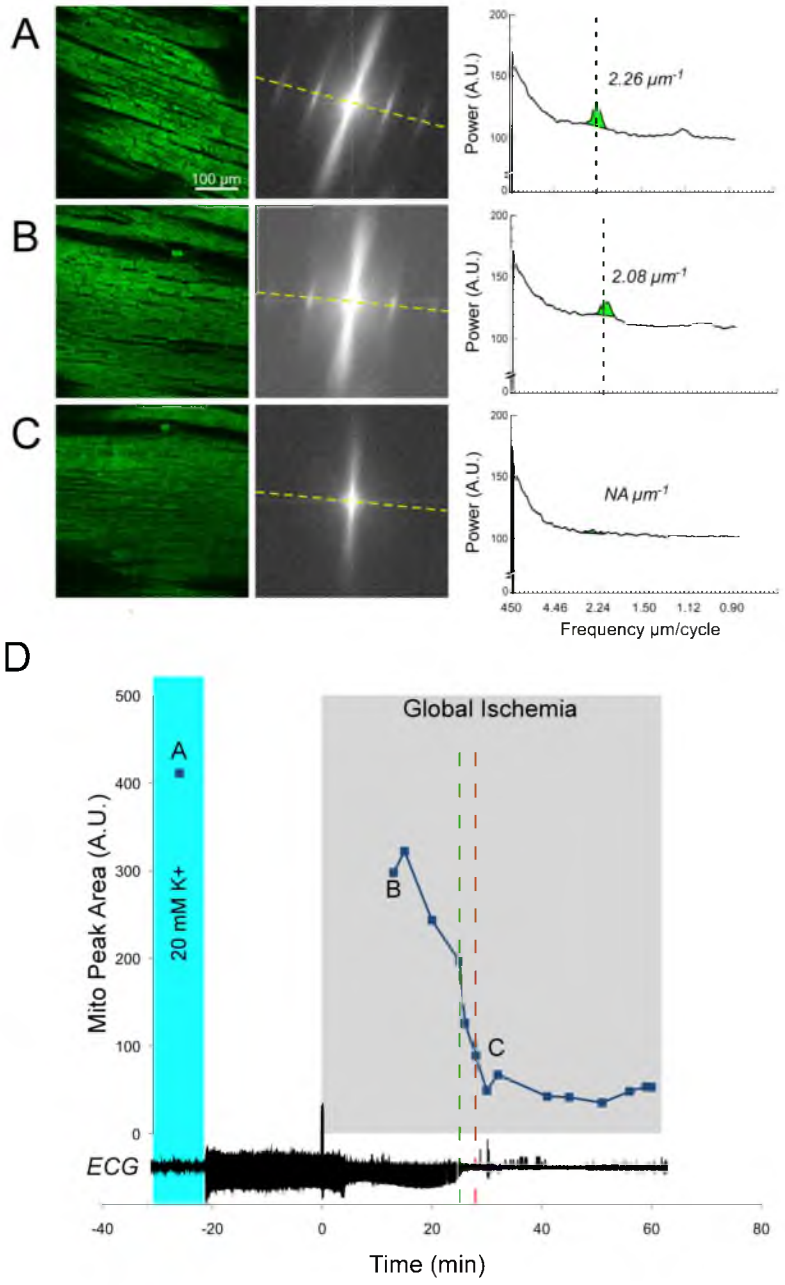

Figure 7.6. Representative data from Glyb experiment. Panels A-C are TMRM images, SFT power spectrums and spectral profiles taken from the respective points in panel D. Panel D is MPA dynamics time aligned with ECG. Vertical dashed green line marks 50% depolarization; vertical dashed red line marks asystole time. A is during 20 mM K+ 26 minutes prior to ischemia and shows well-polarized $\Delta\Psi_m$. At B, 13 minutes of ischemia, $\Delta\Psi_m$ is still well polarized; however, significant $\Delta\Psi_m$ depolarization occurs at 25 minutes of ischemia. Point C shows complete $\Delta\Psi_m$ loss at 32 minutes of ischemia. Asystole occurred after $\Delta\Psi_m$ loss at 28 minutes of ischemia.

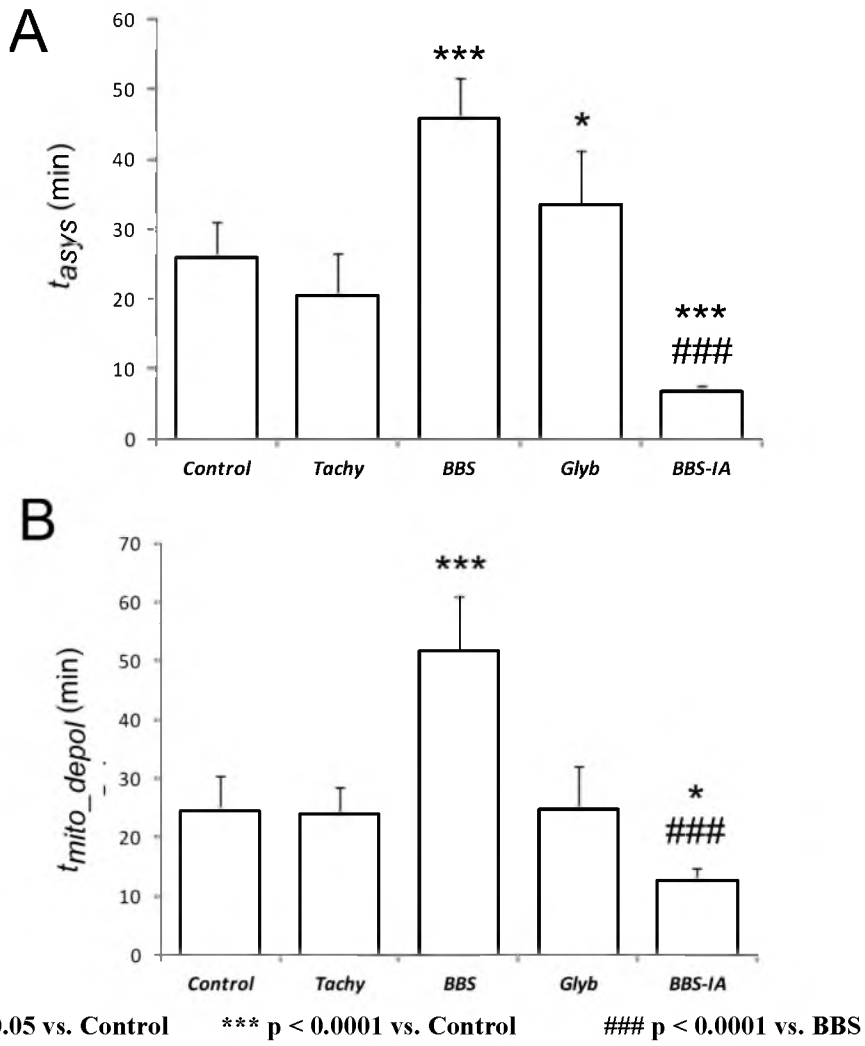

Figure 7.7. Asystole and 50% $\Delta\Psi_m$ depolarization for Control and energetic interventions. (A) Timing of asystole for different groups. Control and Tachy were not significantly different. BBS and Glyb groups had significantly later asystole times than Control. BBS-IA was significantly earlier than both Control and BBS. (B) BBS caused the latest $\Delta\Psi_m$ loss, and was significantly different than Control and BBS-IA. BBS-IA was also significantly earlier than Control. $\Delta\Psi_m$ was not significantly different between Control, Tachy, and Glyb.

BBS-IA group. Also, t_{mito_depol} was very significantly shorter in BBS-IA group than in BBS group.

Figure 7.8 shows the difference between t_{asys} and t_{mito_depol} in all experiments. In each group, this difference was compared to zero (i.e., the two events are simultaneous). One can see that in Control and Tachy groups, there was no consistent order in the timing of the two critical events. In BBS group, in all but one heart, t_{asys} was ahead of t_{mito_depol}, but the presence of two outliers precluded statistically significant difference from zero. In all BBS-IA experiments, t_{asys} was ahead of t_{mito_depol}, and in all Glyb experiments, t_{asys} was behind t_{mito_depol}. Only in these two groups the difference between t_{asys} and t_{mito_depol} was significant ($p<0.05$).

7.5 Discussion

7.5.1 Relationship between $\Delta\Psi_m$ collapse and electrical failure during global ischemia: Mutual dependence on the energy balance

$\Delta\Psi_m$ collapse during no-flow ischemia is a critical event of I/R, which has been implicated in the loss of myocardial excitability and subsequent postreperfusion lethal arrhythmias by a mechanism of so-called "metabolic sink block" (1). Conceptually, the mechanism involves $\Delta\Psi_m$ loss due to the opening of the inner membrane anionic channel (IMAC), which is a self-enhancing and propagating event because IMAC opening is promoted by reactive oxygen species (ROS) and in turn releases ROS. It is further assumed that ATP hydrolysis by mitochondrial F_0-F_1 ATPase under these conditions causes a critical depletion of cellular ATP and activation of K-ATP channel. In turn, K-

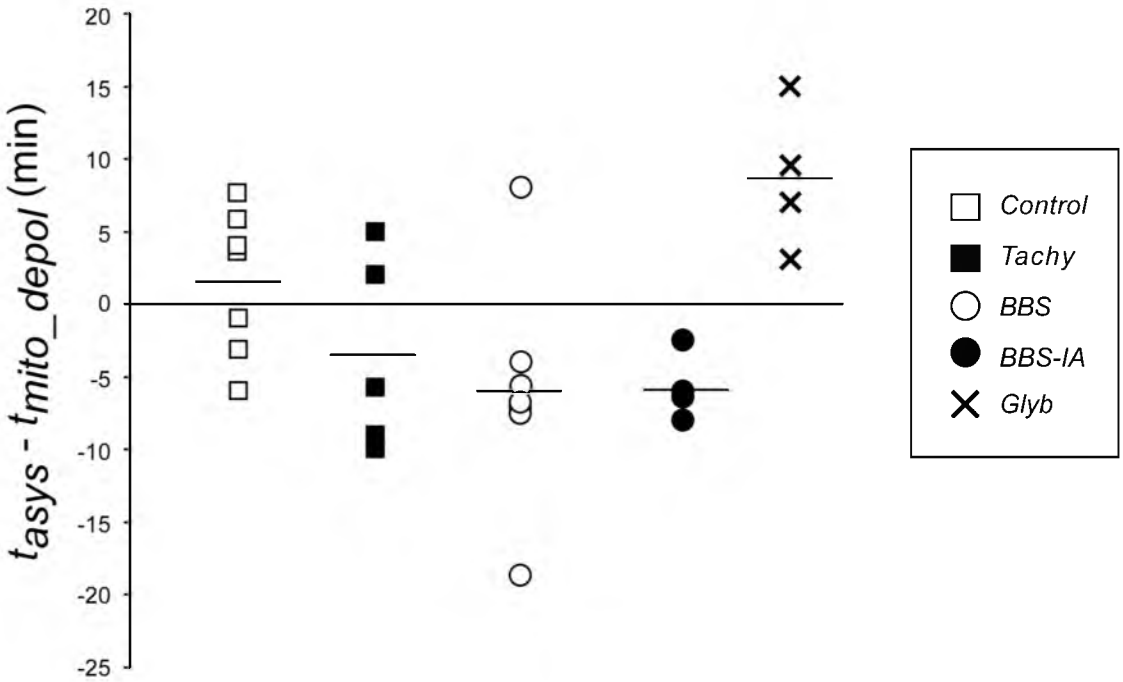

Figure 7.8. Time delay between asystole and $\Delta\Psi_m$ depolarization. In control hearts, the time delay was dispersed between positive and negative values, but on average, asystole occurred after $\Delta\Psi_m$ loss by 2 minutes. For Tachy, BBS, and BBS-IA groups, asystole on average preceeded $\Delta\Psi_m$ depolarization. As predicted, Glyb application caused asystole to occur after $\Delta\Psi_m$ loss, with an average difference of 11 minutes.

ATP activation causes a critical source-sink mismatch, by dramatically increasing the sink for the excitatory current, and conduction failure (1). This mechanism was postulated without the actual analysis of the ischemic dynamics of $\Delta\Psi_m$. Our study shows a strong temporal correlation between the time of the estimated 50% of $\Delta\Psi_m$ loss and the moment of the electrical failure under a variety of experimental conditions, which would be compatible with the "metabolic sink block" mechanism. However, whether or not this correlation reflects a cause-effect relationship between $\Delta\Psi_m$ collapse and electrical failure cannot be determined with certainty. During ischemia, the almost exclusive source of ATP is anaerobic glycolysis, and the major consumers are muscle myosin II ATPase, ATP-consuming ionic pumps, and the mitochondrial F_1F_0-ATPase. During near-anoxia, $\Delta\Psi_m$ can be maintained at an almost unchanged level as long as the glycolytic ATP flux supplies enough ATP to the mitochondria to keep the free energy of ATP hydrolysis below the electrochemical proton potential (14). Moreover, $\Delta\Psi_m$ can be maintained at a relatively constant level even when the cytosolic [ATP] decreases and K-ATP channel is activated (14). Thus, the opening of K-ATP channel is ultimately determined by the dynamics of the balance between the glycolytic ATP production and the three major consuming processes mentioned above, and it does not have to follow $\Delta\Psi_m$ collapse. In any event, it is clear that both $\Delta\Psi_m$ depolarization and electrical failure had strong and similar dependence on glycolytic ATP. Our data suggest that in the presence of blebbistatin, anaerobic glycolysis was functional and was producing sufficient amount of ATP to cover the energy costs of ionic pumps and $\Delta\Psi_m$ maintenance for about 50 minutes of no-flow ischemia. Indeed, when anaerobic glycolysis was inhibited by iodoacetate in the presence of blebbistatin, the two critical events occurred about 40

minutes earlier. There was an apparent partial recovery of $\Delta\Psi_m$ later in ischemia despite the continuous presence of iodoacetate (see Figure 7.4), which, however, was not followed by a recovery in electrical activity. It is difficult to explain this phenomenon. One possibility is a decrease in the blocking efficacy of iodoacetate due to some changes in chemical environment caused by ischemia. Alternatively, a GTP/ATP producing reaction in the citric acid cycle converting succinyl-CoA to succinate and catalyzed by succinyl-CoA ligase, which remains active throughout long periods of ischemia, could have been unregulated under conditions of glycolytic inhibition, possibly due to an ischemia-induced increase in inorganic phosphate (23), and provide a source of ATP for the maintenance of $\Delta\Psi_m$.

The most straightforward explanation for the delay of $\Delta\Psi_m$ collapse and asystole afforded by blebbistatin as compared to Control group is the ATP preservation due to the blockade of muscle myosin II ATPase. If this assumption is correct, then energy spent on contraction until it fails at about 7-10 minutes of ischemia would be enough to support $\Delta\Psi_m$ and the residual activity of ionic pumps between 25 and 45-50 minutes of ischemia (the difference in the timing of critical events between Control and BBS groups). This would mean that noncontractile ATP expenditures between 25 and 45-50 minutes of ischemia (required for $\Delta\Psi_m$ maintenance, the work of ionic pumps, and other, presumably minor, expenses) are roughly equivalent to 40% of the ATP required for contraction during the first 10 minutes of ischemia (per unit of time). Whereas a detailed analysis of the effect of blebbistatin on the energy metabolism during ischemia is pending, some previously published results make the above assumption unlikely. Sebbag et al. (28) analyzed ATP depletion and lactate accumulation in globally ischemic canine

ventricular myocardial in the absence and the presence of electromechanical uncoupler 2,3-Butanedione monoxime (BDM) at the concentration that fully abolished contraction. Simple calculations based on the data presented by these authors indicate that even during the first 10 minutes of ischemia (i.e., the phase during which cardiac contraction is present), BDM reduced energy consumption by only 30%. Accordingly, noncontractile expenses during the early phase of ischemia constituted 70% of total ischemic ATP consumption, or ~170% of the contractile ATP cost. Thus, unless the noncontractile energy expenses were markedly reduced in later phases of ischemia, the energy saving due to the abolishment of contraction during early ischemia may not be enough to explain the ability of BBS to markedly postpone the time of $\Delta\Psi_m$ collapse and asystole. Note also that rapid pacing did not significantly change the timing of $\Delta\Psi_m$ collapse and asystole, supporting the idea that contraction, and even the maintenance of ionic homeostasis, were not critical factors of ATP depletion during ischemia. Together, these observations suggest that ATP hydrolysis by F_0-F_1 ATPase is the major ATP sink during ischemia, and also that blebbistatin might have energy-sparing effects beyond myosin II ATPase blockade. The effect of blebbistatin on energy metabolism during ischemia is the subject of an ongoing study in our lab.

It was postulated that the link between $\Delta\Psi_m$ collapse and electrical failure during ischemia is mediated via activation of K-ATP (1). In our study, blockade of K-ATP by glybenclamide postponed asystole by about 7 minutes and also increased the separation between 50% MPA loss and asystole from ~2 to ~11 minutes. These findings are in agreement with asystole-delaying effect of glybenclamide observed by us previously in the canine model of ischemic VF (31) and support the notion of "metabolic sink block"

(1).

Regarding the reactive oxygen species (ROS)-induced-ROS-release-mediated IMAC opening as a mechanism of $\Delta\Psi_m$ collapse (2), from the standpoint of energy balance, it is just a mechanism contributing to inner mitochondrial membrane (IMM) leak and thus increasing ATP hydrolysis by F_0-F_1 ATPase. The fact that blebbistatin has such a huge effect with respect to the maintenance of $\Delta\Psi_m$ during ischemia, and assuming that the timing of $\Delta\Psi_m$ collapse is largely determined by a critical decrease in [ATP] (14) suggests that either the ROS-induced ROS-release mechanism is not a significant factor of ischemic IMM leak, or that blebbistatin somehow is able to interfere with this mechanism. This possibility should be tested in future studies.

7.5.2 Use of blebbistatin should be avoided in studies concerning mechanisms and outcomes of myocardial I/R

One of the conundrums for researchers attempting real-time imaging in beating hearts is the necessity to immobilize the heart, which, unavoidably, alters the outcomes. The current study shows that blebbistatin is an extreme case in point, because it changed all the major endpoints of the study (the time of $\Delta\Psi_m$ collapse and the time of asystole) by about 100%. BBS was shown previously to affect electrophysiology (6) and the mechanism of VF (19) in normoxemic hearts, but this may be the first study to identify the dramatic effects of BBS on the I/R phenomena. Clearly, these findings largely exclude blebbistatin as a viable tool for heart immobilization in studies concerning the mechanisms and outcomes of I/R. Researchers should look for alternative approaches which have less influence on I/R phenomena. Perhaps at this point, it is easier said than

done. Other popular heart immobilizers (BDM and cytochalasin D) were shown to have various effects on cardiac electrophysiology, arrhythmias, and energy balance in normal or ischemic hearts (5, 28). Complete exclusion of immobilizers from physiological cardiac imaging is difficult. The degree of difficulty depends on the type of imaging. For wide-field video imaging (a.k.a. "optical mapping"), immobilization by way of mechanical restraint served well enough in many of those studies which focused on analysis of propagation of electrical waves in the heart (9, 36). There were a few attempts to use "demorphing" approaches for the purposes of virtual immobilization of the heart (25), and ratiometric imaging to subtract the motion artifact (15). However, these approaches have not substituted the wide use of chemical immobilizers by the optical mapping community, perhaps indicating their limited practical utility. For imaging physiological parameters whose dynamics are slow as compared to the cardiac cycle (e.g., $\Delta\Psi_m$, [NADH], [FADH2], [ROS]), the motion artifact may be less of an issue because the signals can be averaged over many contraction cycles. However, I/R imposes additional problems due to deformation of the heart geometry following shrinking/swelling of the myocardium during I/R. As we argued in our previous publication (35), such changes in heart shape may seriously confound interpretation of slow signals recorded using optical mapping techniques, because the changes in fluorescence intensity due to spatial deformations and attendant differences in illumination, scattering, and/or local fluorophore concentration can be misinterpreted as reflecting a real change in the physiological parameter of interest. Of note, shrinking/swelling of myocardium during I/R is not abolished by blebbistatin (35) or BDM (Garg, Taylor, Zaitsev, unpublished data).

Confocal or multiphoton imaging of physiological fluorescent indicators in live perfused hearts is a newer modality than optical mapping. With currently available apparatuses, the cellular and subcellular images of syncytial cardiac myocytes cannot be obtained without complete or nearly complete elimination of cardiac contraction. Thus, to the best of our knowledge, all studies of this kind performed to-date involved using one of the electromechanical uncouplers, including at least two studies addressing the dynamics of $\Delta\Psi_m$ during I/R, which used blebbistatin (10, 21, 29). The current study may be the first to present information about ischemic changes in $\Delta\Psi_m$ without uncouplers. In order to do so, for control recordings of $\Delta\Psi_m$, we immobilized the heart using hyperkalemic solution. We postulated that depolarization of the plasma membrane with the high extracellular concentration of potassium did not have a major effect on $\Delta\Psi_m$. Nevertheless, such physiological modulations of $\Delta\Psi_m$ are unlikely to be comparable to $\Delta\Psi_m$ collapse occurring during total ischemia. During ischemia, we took advantage of contraction failure leading to complete heart immobilization between 5 and 15 minutes of ischemia. From that moment on, we were able to obtain high-fidelity confocal images and track the changes in $\Delta\Psi_m$ based on the MPA measurement. An obvious limitation of this approach is the inability to track $\Delta\Psi_m$ during the early phase of ischemia, before the ischemic contraction failure takes place. Fortunately for us, the critical transition, i.e., when MPA value fell below 50 % of its dynamic range, occurred after the contraction failure in all experiments not using blebbistatin, with the exception of one experiment in Glyb group. Thus, it appears to be the case that the failure of contraction precedes $\Delta\Psi_m$ collapse during ischemia.

Summarizing the above, blebbistatin presents an outstanding example of the

situation where modulating the system for technical purposes dramatically distorts the behavior of the system. It was assumed for some time that blebbistatin is free of limitations imposed by use of BDM (29), but this assumption has to be discarded as far as studies of I/R are concerned. For the purposes of confocal imaging, the alternative is to use short-term immobilization with hyperkalemic solution in perfused hearts, and wait for contraction failure during ischemia. Currently, this seems to be the best out of bad solutions. This situation should motivate the search for computer-aided methods to "unscramble" confocal images distorted by cardiac contraction, and some recent developments towards that end give hope (27).

CHAPTER 8

CONCLUSIONS AND FUTURE WORK

Sudden cardiac arrest remains one of the leading causes of death in the United States despite continued research and improved treatment protocols. Resuscitation failure due to asystole or recurrent fibrillation contributes to the alarmingly low survival rate for patients in out-of-hospital SCA. One postulated mechanism linking metabolic stress of SCA and electrical abnormalities is the loss of mitochondrial inner membrane potential ($\Delta\Psi_m$) and the consequent activation of the ATP-sensitive potassium channel (K_{ATP}) when cellular ATP is critically depleted. The research presented in this dissertation addressed, for the first time, the relationship between mitochondrial depolarization caused by metabolic stress and electrical abnormalities in a whole-heart model of SCA during the clinically relevant time frame.

8.1 Ventricular fibrillation and inexcitability during global ischemia

The first project of this dissertation looked at the complex dynamics of ventricular fibrillation and the development of inexcitability during long-duration ventricular fibrillation (LDVF) and global ischemia. The main findings of the study were the presence of interchamber and intrachamber heterogeneities in ventricular fibrillation rate (VFR) and the emergence of fully inexcitable areas interwoven with excitable areas in

both ventricles during late-stage global ischemia. Gradients in VFR developing during ischemia have been previously documented in both canine and rabbit models; however, our research demonstrated for the first time the simultaneous presence of both epicardial to endocardium and right ventricular (RV) to left ventricular (LV) gradients. Additionally, we found that patterns of activation gradients during LDVF are different between the two chambers with a significant VFR gradient arising between the mid-myocardium and epicardium of the RV, but not the between the mid-myocardium. In contrast, significant differences in VFR were present between all layers of the LV. The RV to LV epicardial gradient was one of the most striking, with the RV epicardium maintaining excitability significantly longer than the LV epicardium. The RV also had repetitive reentry circuits in the later stages of LVDF while no reentry circuits were present in the LV. Interestingly, fast activation was consistently found in the epicardial and mid-myocardial layers of the septum during late LDVF. Previous research had focused on the endocardial Purkinje fibers as the source of activity during VF; however, the fast activation sites were located 4-5 mm from the nearest endocardium surface, indicating that the septum may harbor sources maintaining fibrillatory activity independent of the Purkinje fibers. Additionally, we examined the differences in action potential duration (APD) and diastolic interval (DI) between the LV and RV epicardium. During LDVF, we found a right to left gradient in the DIs, but relatively unchanged APDs.

A novel finding of this study was the development of a highly heterogeneous, mosaic pattern of inexcitability in both the LV and RV epicardium during LDVF. Present after 4 minutes of global ischemia, both chambers had areas of complete inexcitability

adjacent to areas maintaining activation. In some cases, the gradient was very sharp, reaching 4-5 Hz/mm. A proposed mechanism for localized areas of inexcitability is the heterogeneous activation of the ATP-sensitive potassium channel secondary to mitochondrial membrane depolarization. As a subproject, we tested the effects of the heterogeneous K_{ATP} channel opening hypodissertation by applying the I_{KATP} blocker glybenclamide. We found that glybenclamide markedly reduced the areas of total inexcitability in the first 10 minutes of ischemia, but did not completely remove the epicardial heterogeneities present within the ventricles. Importantly, we did find that K_{ATP} channel blockade reduced the incidence of asystole; in hearts not treated with glybenclamide, 5 out of 9 hearts were asystolic before 10 minutes of LDVF; in contrast, in 6 out of 6 hearts treated with glybenclamide, asystole did not occur within the first 10 minutes of global ischemia.

8.2 Mitochondrial depolarization during modeled SCA

To further investigate the role of mitochondrial membrane depolarization in asystole, we established a new methodology to both monitor $\Delta\Psi_m$ and excitability in a whole-heart model of SCA. As discussed in the Chapter 3, we were required to change both our imaging system and our animal model. Additionally, before we could study the physiological link between metabolic stress and inexcitability, we had to develop a new method to analyze $\Delta\Psi_m$-sensitive TMRM fluorescence in a no-flow model of global ischemia. TMRM is a cationic membrane-permeable dye that distributes in the extracellular space, cytosol, and mitochondria based on a three-chamber Nernstian distribution. Therefore, when $\Delta\Psi_m$ depolarization occurs, the dye redistributes itself into

the cytosol and extracellular space. This approach works in isolated cell preparations because when $\Delta\Psi_m$ depolarizes and TMRM redistributes, the dye that moves into the extracellular space and is continuously washed away, therefore reducing the total number of dye molecules and the collected fluorescence. However, in models of no-flow global ischemia, the total amount of dye remains the same and the mean TMRM fluorescence does not decrease upon $\Delta\Psi_m$ depolarization. The diversity in previous reports of $\Delta\Psi_m$ during global ischemia could be the result of ambiguity in mean TMRM fluorescence. To address the limitations of the traditional approach, we developed a new method to monitor $\Delta\Psi_m$ during ischemia using spectral analysis of the confocally recorded TMRM signal. In cardiac myocytes, the mitochondria are arranged in a highly ordered crystal-like pattern between the z-disks (38). Therefore, TMRM accumulation in negatively charged mitochondria creates distinct peaks in the spatial Fourier transform power spectrum of TMRM images. TMRM redistribution between the mitochondria and cytoplasm following $\Delta\Psi_m$ depolarization leads to dissipation of the mitochondrial peaks. In order to quantify $\Delta\Psi_m$, we developed an algorithm to measure the area under the peaks. We validated this method against the traditional mean fluorescence approach in both isolated and whole-heart models using the $\Delta\Psi_m$ uncoupler carbonylcyanide-p-trifluoromethoxypheny hydrazone (FCCP). In hearts subjected to global no-flow ischemia, we consistently detected $\Delta\Psi_m$ depolarization after 30 minutes of ischemia using the SFT method, but we did not consistently detect depolarization using the mean fluorescence method. Instead, some hearts showed a drop in fluorescence late in ischemia and others showed an increase. Previous studies of $\Delta\Psi_m$ during ischemia and reperfusion reported the presence of individual cells with a complete loss of TMRM signal, which are

referred to as 'dropout' cells. We occasionally observed such 'dropouts' during ischemia and reperfusion experiments, but we believe they are different than the global depolarization detected by SFT and might reflect both a significant loss of mitochondrial potential and sarcolemmal integrity.

Using the SFT method, we investigated the temporal relationship of mitochondrial membrane depolarization and inexcitability. For the first time, we monitored $\Delta\Psi_m$ and excitability in hearts subject to global ischemia. Additionally, we examined the effects of modulating the ischemic energy balance by using rapid pacing, the inhibitor of myosin II ATPase blebbistatin, and the inhibitor of anaerobic glycolysis iodoacetate. We found a strong correlation between the onset of asystole and the time of $\Delta\Psi_m$ under all test conditions. However, it is unclear if the correlation reflects a cause-effect relationship between $\Delta\Psi_m$ depolarization and inexcitability. In control hearts, $\Delta\Psi_m$ depolarization and asystole occurred, relatively close together, on average at 24 and 26 minutes of ischemia, respectively. Interestingly, blebbistatin afforded a remarkable cardio-protective effect, delaying both parameters to 46 and 50 minutes of ischemia. Additionally, blebbistatin improved $\Delta\Psi_m$ recovery and reduced the incidence of arrhythmias in early reperfusion. The almost doubling of the timing of $\Delta\Psi_m$ and asystole warrants caution when using the mechanical uncoupler during ischemic studies but encourages further research into the mechanisms of protection. Inhibition of anaerobic glycolysis using iodoacetate rapidly accelerated $\Delta\Psi_m$ depolarization and inexcitability to 13 and 7 minutes of ischemia, despite the presence of blebbistatin. The acceleration of both parameters by iodoacetate points to the importance of anaerobic glycolysis in providing cellular ATP for both maintaining $\Delta\Psi_m$ and blocking K_{ATP} opening. K_{ATP}

channel blockade with glybenclamide postponed asystole, which is consistant with the hypodissertation that ATP derived from glycolysis dictates K_{ATP} current during ischemia.

8.3 Future work

The characterization of ischemic ventricular fibrillation and mitochondrial membrane potential presented in this dissertation provides important information that can help to improve the understanding of the dismal survival rate of SCA; however, continued research is needed to improve outcomes for SCA victims. While data were presented from experimental methods characterized inexcitability in epicardial activation and determined the relationship between epicardial $\Delta\Psi_m$ loss and global asystole, the direct relationship between localized electrical propagation failure and $\Delta\Psi_m$ loss remains a research goal. Ideally, one could image propagation with a voltage-sensitive dye and $\Delta\Psi_m$ with TMRM in the exact same field with little or no time delay between the individual signal acquisitions. In the second project, we explored the possibility of imaging $\Delta\Psi_m$ loss using wide field optical mapping; however, the analysis of TMRM signal is limited by the previously discussed issues with total fluorescence measurements in no-flow ischemia. Another possible method to image both voltage-sensitive and $\Delta\Psi_m$–sensitive fluorescence would be to confocally image mitochondrial signal at a magnification suitable for the SFT method, then switch to a lower magnification and record voltage-sensitive signal with a CCD camera normally used in wide field optical mapping. Previous research by our lab showed that a CCD camera mounted to an inverted microscope was sensitive enough to detect action potentials in isolated cells (39). This approach could precisely tell whether or not local inexcitability is the directly

correlated with $\Delta\Psi_m$ loss.

The unexpected cardio-protective effects of blebbistatin discussed in this dissertation present another interesting area of research, particularly during reperfusion. The data presented in Chapter 7 demonstrate that hearts treated with blebbistatin had markedly reduced incidences of arrhythmias during reperfusion, along with slightly better recovery of MPA. Initial studies by the Zaitsev lab investigating blebbistatin's effect on sarcolemmal permeability during reperfusion found that blebbistatin markedly reduced the percent of cells with permeabilized membranes after 2 hours of ischemia. Additionally, blebbistatin completely eliminated the presence of infarcted tissue after 3 hours of reperfusion (37). Clinically, a better understanding of the mechanisms of cardiopretection by blebbistatin in ischemia and reperfusion could help both delay asystole during ischemia and prevent cell death and arrhythmias during reperfusion.

Defibrillation is the gold standard treatment for VF-induced SCA. The presence of local areas of inexcitability, as found in the isolated canine heart, could not only reduce the efficacy of defibrillation shocks, but the mosaic pattern could also provide a substrate for refibrillation following shock. Understanding the role of heterogeneous inexcitability on defibrillation and recurrent VF could help develop better CPR and defibrillation protocols. It would also be of interest to explore whether partial reperfusion through chest compression, or reduction of inexcitable areas through K_{ATP} channel block, changes the degree of inexcitability enough to improve defibrillation.

The effects of defibrillation on mitochondria during ischemia could also be investigated using the SFT method developed in this dissertation. Recent studies have shown transient pores formed by electroporation of membranes during defibrillation (3,

22). Independently, mitochondrial damage, accompanied by increases in lactate production and reduced oxygen consumption, has also been implicated in myocardial injury (13, 32). Tsai et al. found that VF and electrical shock, both alone and in syndissertation, caused extensive mitochondrial swelling, membrane rupture, and decreased respiration (33). Cytosolic calcium overload, during defibrillation (16) may lead to subsequent mitochondrial calcium overload, leading to the mitochondrial permeability transition pore (mPTP) opening (4). Absent from the existing research is direct evidence demonstrating changes in $\Delta\Psi_m$ during defibrillation; however, mitochondrial damage due to defibrillation could contribute to decreased long-term patient survival.

8.4 Overall summary and potential significance of this work

In conclusion, the research presented in the preceding chapters has addressed important gaps in knowledge in the field of sudden cardiac arrest. The first project characterized for the first time the development of spatially complex, inter- and intrachamber gradients and heterogeneous patterns of excitability during the clinically relevant time frame of sudden cardiac arrest. Localized inexcitability was reduced by blocking I_{KATP} with glybenclamide, a well as the incidence of asystole. Investigating the hypodissertation that mitochondrial depolarization leads to K_{ATP} channel opening and asystole, we found that $\Delta\Psi_m$ and inexcitability were temporally related, but not directly correlated, suggesting that anaerobic glycolysis was the key provider of cytosolic ATP during ischemia. The accelerated loss of both parameters with the inhibition of glycolysis confirmed this, and encourages further research into factors affecting glycolysis during

ischemia. An unexpected finding of this dissertation was the cardio-protective effects of blebbistatin, cautioning its use in ischemia research but providing a basis to further research the mechanism of its unprecedented protective effects.

REFERENCES

1. **Akar FG, Aon MA, Tomaselli GF, and O'Rourke B.** The mitochondrial origin of postischemic arrhythmias. *The Journal of clinical investigation* 115: 3527-3535, 2005.

2. **Akar FG and O'Rourke B.** Mitochondria are sources of metabolic sink and arrhythmias. *Pharmacology & therapeutics* 131: 287-294, 2011.

3. **Al-Khadra A, Nikolski V, and Efimov IR.** The role of electroporation in defibrillation. *Circulation research* 87: 797-804, 2000.

4. **Ayoub IM, Radhakrishnan J, and Gazmuri RJ.** Targeting mitochondria for resuscitation from cardiac arrest. *Critical care medicine* 36: S440-446, 2008.

5. **Baker LC, Wolk R, Choi BR, Watkins S, Plan P, Shah A, and Salama G.** Effects of mechanical uncouplers, diacetyl monoxime, and cytochalasin-D on the electrophysiology of perfused mouse hearts. *American journal of physiology Heart and circulatory physiology* 287: H1771-1779, 2004.

6. **Brack KE, Narang R, Winter J, and Ng GA.** The mechanical uncoupler blebbistatin is associated with significant electrophysiological effects in the isolated rabbit heart. *Experimental physiology* 98: 1009-1027, 2013.

7. **Brown DA and O'Rourke B.** Cardiac mitochondria and arrhythmias. *Cardiovascular research* 88: 241-249, 2010.

8. **Camara AK, Bienengraeber M, and Stowe DF.** Mitochondrial approaches to protect against cardiac ischemia and reperfusion injury. *Frontiers in physiology* 2: 13, 2011.

9. **Choi BR and Salama G.** Simultaneous maps of optical action potentials and calcium transients in guinea-pig hearts: mechanisms underlying concordant alternans. *The Journal of physiology* 529 Pt 1: 171-188, 2000.

10. **Davidson SM, Yellon DM, Murphy MP, and Duchen MR.** Slow calcium waves and redox changes precede mitochondrial permeability transition pore opening in the intact heart during hypoxia and reoxygenation. *Cardiovascular research* 93: 445-453, 2012.

11. **Dedkova EN and Blatter LA.** Measuring mitochondrial function in intact cardiac myocytes. *Journal of molecular and cellular cardiology* 52: 48-61, 2012.

12. **Fedorov VV, Lozinsky IT, Sosunov EA, Anyukhovsky EP, Rosen MR, Balke CW, and Efimov IR.** Application of blebbistatin as an excitation-contraction uncoupler for electrophysiologic study of rat and rabbit hearts. *Heart rhythm : the official journal of the Heart Rhythm Society* 4: 619-626, 2007.

13. **Gaba DM, Maxwell MS, Merlone S, and Smith C.** Internal countershock produces myocardial damage and lactate production without myocardial ischemia in anesthetized dogs. *Anesthesiology* 66: 477-482, 1987.

14. **Ganitkevich V, Mattea V, and Benndorf K.** Glycolytic oscillations in single ischemic cardiomyocytes at near anoxia. *The Journal of general physiology* 135: 307-319, 2010.

15. **Himel HDt and Knisley SB.** Imaging of cardiac movement using ratiometric and nonratiometric optical mapping: effects of ischemia and 2, 3-butaneodione monoxime. *IEEE transactions on medical imaging* 25: 122-127, 2006.

16. **Krauthamer V and Jones JL.** Calcium dynamics in cultured heart cells exposed to defibrillator-type electric shocks. *Life sciences* 60: 1977-1985, 1997.

17. **Kudenchuk PJ, Fahrenbruch CE, and Rea TD.** Cardiac arrest: survivors or still victims? *Circulation* 118: 328-330, 2008.

18. **Lo BM, Quinn SM, Hostler D, and Callaway CW.** Rescue shock outcomes during out-of-hospital cardiac arrest. *Resuscitation* 75: 469-475, 2007.

19. **Lou Q, Li W, and Efimov IR.** The role of dynamic instability and wavelength in arrhythmia maintenance as revealed by panoramic imaging with blebbistatin vs. 2,3-butanedione monoxime. *American journal of physiology Heart and circulatory physiology* 302: H262-269, 2012.

20. **Lyon AR, Joudrey PJ, Jin D, Nass RD, Aon MA, O'Rourke B, and Akar FG.** Optical imaging of mitochondrial function uncovers actively propagating waves of mitochondrial membrane potential collapse across intact heart. *Journal of molecular and cellular cardiology* 49: 565-575, 2010.

21. **Matsumoto-Ida M, Akao M, Takeda T, Kato M, and Kita T.** Real-time 2-photon imaging of mitochondrial function in perfused rat hearts subjected to ischemia/reperfusion. *Circulation* 114: 1497-1503, 2006.

22. **Nikolski VP and Efimov IR.** Electroporation of the heart. *Europace : European pacing, arrhythmias, and cardiac electrophysiology : journal of the working groups on cardiac pacing, arrhythmias, and cardiac cellular electrophysiology of the European*

Society of Cardiology 7 Suppl 2: 146-154, 2005.

23. **Phillips D, Aponte AM, French SA, Chess DJ, and Balaban RS.** Succinyl-CoA synthetase is a phosphate target for the activation of mitochondrial metabolism. *Biochemistry* 48: 7140-7149, 2009.

24. **Rea TD, Eisenberg MS, Sinibaldi G, and White RD.** Incidence of EMS-treated out-of-hospital cardiac arrest in the United States. *Resuscitation* 63: 17-24, 2004.

25. **Rohde GK, Dawant BM, and Lin SF.** Correction of motion artifact in cardiac optical mapping using image registration. *IEEE transactions on bio-medical engineering* 52: 338-341, 2005.

26. **Sasaki N, Sato T, Marban E, and O'Rourke B.** ATP consumption by uncoupled mitochondria activates sarcolemmal K(ATP) channels in cardiac myocytes. *American journal of physiology Heart and circulatory physiology* 280: H1882-1888, 2001.

27. **Schroeder JL, Luger-Hamer M, Pursley R, Pohida T, Chefd'hotel C, Kellman P, and Balaban RS.** Short communication: Subcellular motion compensation for minimally invasive microscopy, in vivo: evidence for oxygen gradients in resting muscle. *Circulation research* 106: 1129-1133, 2010.

28. **Sebbag L, Verbinski SG, Reimer KA, and Jennings RB.** Protection of ischemic myocardium in dogs using intracoronary 2,3-butanedione monoxime (BDM). *Journal of molecular and cellular cardiology* 35: 165-176, 2003.

29. **Slodzinski MK, Aon MA, and O'Rourke B.** Glutathione oxidation as a trigger of mitochondrial depolarization and oscillation in intact hearts. *Journal of molecular and cellular cardiology* 45: 650-660, 2008.

30. **Smith RM, Velamakanni SS, and Tolkacheva EG.** Interventricular heterogeneity as a substrate for arrhythmogenesis of decoupled mitochondria during ischemia in the whole heart. *American journal of physiology Heart and circulatory physiology* 303: H224-233, 2012.

31. **Taylor TG, Venable PW, Shibayama J, Warren M, and Zaitsev AV.** Role of KATP channel in electrical depression and asystole during long-duration ventricular fibrillation in ex vivo canine heart. *American journal of physiology Heart and circulatory physiology* 302: H2396-2409, 2012.

32. **Trouton TG, Allen JD, Yong LK, Rooney JJ, and Adgey AA.** Metabolic changes and mitochondrial dysfunction early following transthoracic countershock in dogs. *Pacing and clinical electrophysiology : PACE* 12: 1827-1834, 1989.

33. **Tsai MS, Huang CH, Tsai CY, Chen HW, Lee HC, Cheng HJ, Hsu CY,**

Wang TD, Chang WT, and Chen WJ. Ascorbic acid mitigates the myocardial injury after cardiac arrest and electrical shock. *Intensive care medicine* 37: 2033-2040, 2011.

34. **Valenzuela TD, Roe DJ, Cretin S, Spaite DW, and Larsen MP.** Estimating effectiveness of cardiac arrest interventions: a logistic regression survival model. *Circulation* 96: 3308-3313, 1997.

35. **Venable PW, Taylor TG, Sciuto KJ, Zhao J, Shibayama J, Warren M, Spitzer KW, and Zaitsev AV.** Detection of mitochondrial depolarization/recovery during ischaemia--reperfusion using spectral properties of confocally recorded TMRM fluorescence. *The Journal of physiology* 591: 2781-2794, 2013.

36. **Venable PW, Taylor TG, Shibayama J, Warren M, and Zaitsev AV.** Complex structure of electrophysiological gradients emerging during long-duration ventricular fibrillation in the canine heart. *American journal of physiology Heart and circulatory physiology* 299: H1405-1418, 2010.

37. **Venable PW, Sciuto, K,J.; Taylor, T.G.; Garg, V.; Shibayama, J.; Spitzer, K.W.; Zaitsev, A.V.** Blebbistatin Delays Mitochondrial Depolarization and Asystole during Myocardial Ischemia, and Prevents Cell Death Upon Reperfusion. *Biophysical journal* 106: 186a, 2014.

38. **Vendelin M, Beraud N, Guerrero K, Andrienko T, Kuznetsov AV, Olivares J, Kay L, and Saks VA.** Mitochondrial regular arrangement in muscle cells: a "crystal-like" pattern. *American journal of physiology Cell physiology* 288: C757-767, 2005.

39. **Warren M, Spitzer KW, Steadman BW, Rees TD, Venable P, Taylor T, Shibayama J, Yan P, Wuskell JP, Loew LM, and Zaitsev AV.** High-precision recording of the action potential in isolated cardiomyocytes using the near-infrared fluorescent dye di-4-ANBDQBS. *American journal of physiology Heart and circulatory physiology* 299: H1271-1281, 2010.

40. **White RD and Russell JK.** Refibrillation, resuscitation and survival in out-of-hospital sudden cardiac arrest victims treated with biphasic automated external defibrillators. *Resuscitation* 55: 17-23, 2002.

41. **Wu TJ, Lin SF, Hsieh YC, Ting CT, and Chen PS.** Ventricular fibrillation during no-flow global ischemia in isolated rabbit hearts. *Journal of cardiovascular electrophysiology* 17: 1112-1120, 2006.